

UNIVERSITÀ
DEGLI STUDI
DI PADOVA

UNIVERSITY OF PADOVA

DEPARTMENT OF INDUSTRIAL ENGINEERING

MASTER THESIS IN AEROSPACE ENGINEERING

STUDY AND CHARACTERIZATION OF THE FILTER STRIP ASSEMBLY OF THE ENVISS CAMERA FOR THE COMET INTERCEPTOR MISSION

SUPERVISOR
PROF. MIRCO ZACCARIOTTO

MASTER CANDIDATE
CARMEN NALETTO,
MATR. 2020553

CO-SUPERVISORS
DR. VANIA DA DEPPO
DR. PAOLA ZUPPELLA
RESEARCH SCIENTISTS AT CNR-IFN

JULY 11, 2023

To my family and all the people I love,
thank you for always believing in me.

Abstract (IT)

EnVisS (Entire Visible Sky) è una telecamera all-sky progettata ad-hoc per la prima missione Fast dell'Agenzia Spaziale Europea (ESA), Comet Interceptor. Lo scopo di questa missione è ampliare la conoscenza sulle comete tramite l'esplorazione e l'incontro ravvicinato di una cometa incontaminata o di un corpo interstellare.

L'obiettivo scientifico di EnVisS è quello di mappare e studiare l'intera chioma della cometa nel intervallo di lunghezza d'onda del visibile. Uno dei componenti principali di EnVisS è il filter strip assembly (FSA), che consentirà di misurare la radianza e le proprietà di polarizzazione della luce diffusa della chioma della cometa. L'attuale progetto (sviluppato da CNR-IFN e Leonardo SpA) del FSA consiste in tre strisce filtranti incollate uno accanto all'altra: un filtro centrale a banda larga e ad alta trasmissione (BB) e due filtri laterali per la polarizzazione lineare.

Oggetto di questo lavoro di tesi è lo studio e la caratterizzazione preliminare del filter strip assembly. Nei laboratori CNR-IFN di Padova (Italia) sono stati testati diversi tipi di filtri polarizzatori per stabilire quale tra questi ha le proprietà più adatte agli scopi di EnVisS. I filtri polarizzatori analizzati sono: RCV8N2EC, ottimizzati per il visibile, UBB01A (ultra broadband) a larga banda, entrambi prodotti dalla ditta Moxtek, e Wide Band prodotto da Polarcor.

Inoltre, il FSA è stato simulato con un software di analisi agli elementi finiti Patran-Nastran. Lo scopo di questa simulazione è determinare se i componenti ottici del filter assembly siano soggetti a cambiamenti strutturali, quando sono sottoposti a carichi esterni e non planarità dell'interfaccia meccanica tra la struttura di supporto e il FSA.

Abstract (EN)

EnVisS (Entire Visible Sky) is an all-sky camera designed to fly on Comet Interceptor, the first European Space Agency (ESA) Fast mission. The aim of this mission is to increase our knowledge on comets by encountering and exploring a truly pristine comet or an interstellar object originating at another star.

EnVisS's scientific task is to image, in push-frame mode, the whole comet coma in the visible range. One of the main components of EnVisS is the filter strip assembly (FSA), a key element to be realized, which aims to measure the radiance and the polarization properties of the comet's coma diffused light. The current design (developed by CNR-IFN and Leonardo SpA) consists of three filter strips glued side by side: one central high transmission broadband (BB) filter and two lateral linear polarization filters.

Object of this thesis work is the study and the preliminary characterization of this filter assembly. In the CNR-IFN laboratories in Padua (Italy) different types of polarizing filters have been tested to establish which one has the most fitting properties for EnVisS's purposes. The analyzed filters are Moxtek visible light polarizer RCV8N2EC and ultra broadband UBB01A, and Polarcor Wide Band polarizer. In addition, the FSA has been simulated with a Finite Element Analysis software Patran-Nastran. The purpose of this analysis is to learn if the optical components of the filter package are prone to structural changes, whenever they are subjected to external loads and to the non-planarity of the mechanical interface between the support structure and the FSA.

Contents

Abstract (it) **v**

Abstract (en) **vi**

1 Introduction **1**
- 1.1 Comet Interceptor . . . 2
  - 1.1.1 Mission analysis . . . 2
  - 1.1.2 Scientific Objectives . . . 4
  - 1.1.3 Payload . . . 6
- 1.2 EnVisS . . . 9

2 Polarizing Filters **13**
- 2.1 Polarization . . . 13
  - 2.1.1 Polarization Ellipse . . . 13
  - 2.1.2 Stokes Parameters . . . 15
  - 2.1.3 Polarizers . . . 17
- 2.2 EnVisS polarization filters candidate . . . 19
  - 2.2.1 Moxtek RCV8N2EC and UBB01A . . . 19
  - 2.2.2 Polarcor Wide Band . . . 22

3 Optical Analysis **25**
- 3.1 Bentham Reflectometer . . . 26
  - 3.1.1 Instrument configuration . . . 26
  - 3.1.2 Laboratory setup and Measurement procedure . . . 27
- 3.2 Atomic Force Microscope . . . 35
  - 3.2.1 Instrument configuration . . . 35
  - 3.2.2 Measurement procedure . . . 38

4 Finite Element Analysis **39**
- 4.1 Filter Strip Assembly . . . 39
- 4.2 Simulation . . . 42
  - 4.2.1 Geometry . . . 43
  - 4.2.2 Meshing . . . 44
  - 4.2.3 Properties . . . 47
  - 4.2.4 Boundary Conditions . . . 48

4.2.5 Loads and Analysis 48

5 Results **51**
5.1 Optical Properties 51
5.1.1 Moxtek RCV8N2EC 52
5.1.2 Moxtek UBB01A 57
5.1.3 Polarcor Wide Band 64
5.1.4 Comparison 68
5.2 Topography 73
5.2.1 Moxtek RCV8N2EC 74
5.2.2 Moxtek UBB01A 76
5.2.3 Polarcor Wide Band 79
5.3 Finite Element Analysis 80
5.3.1 Quasi-static acceleration effect 81
5.3.2 Non-planarity of the mechanical interface 85

6 Future activities **91**

7 Conclusions **93**

8 Appendix **95**
8.1 Electromagnetic spectrum 95
8.2 Polarization Ellipse 97
8.3 Stokes Parameters 99
8.4 Finite Element Method 102
8.5 Additional Results 103
8.5.1 Optical properties 103
8.5.2 Finite Element Analysis 109
8.6 Roughness parameters 116

References **118**

Acknowledgments **123**

Listing of figures

1.1 Comet Interceptor Spacecraft A design (Phase B). 7
1.2 Comet Interceptor Probe B2 design (Phase B). 7
1.3 EnVisS placement configuration and its field of view. 10
1.4 3D-Plus package composed by the CMOS monochrome sensor and glass window (manufactured by AMS-OSRAM) and its electronics. 11
1.5 EnVisS ray-tracing configuration and its CAD model. 11

2.1 Propagation of the transverse optical field. 14
2.2 Functioning of a wire-grid polarizer: when unpolarized light incident on the polarizer, polarization with electric field parallel to wire grid is reflected and polarization with electric field perpendicular to the wire grid is transmitted. 18
2.3 Moxtek polarizing filters general wire-grid configuration. 20
2.4 Moxtek polarizing filters. 20
2.5 Polarcor Wide Band Polarizer. 22

3.1 Main units of the Bentham Reflectometer. 26
3.2 View of the optical breadboard, goniometer, sample/detector stages and motorized rotation mount. 28
3.3 Example of the measured incident signal in the wavelength range 350-1100 nm. 29
3.4 Configuration set up for the transmissivity measurements. 30
3.5 Configuration set up for the reflectivity measurements for $\theta = 10°$. 32
3.6 Park System XE-70 Atomic Force Microscope. 36
3.7 Laser beam bounce detection mechanism. 36
3.8 AFM tip-sample potential energy representation and related scanning modes. 37

4.1 Schematic of EnVisS FSA. 41
4.2 CAD model of the aluminum mounting frame, courtesy of Leonardo SpA. 42
4.3 Geometry of the FSA and glue layers. 43
4.4 Complete geometry of the simulated model. 44
4.5 Mesh of the FSA and glue layers. 45
4.6 Mesh of the supporting frame. 45
4.7 Rigid Body Elements connecting the sensor mass to the supporting structure of the FSA. 46

4.8 Zoom of one of the RBE2. 47
4.9 Simulation of the pinned support of the structure. 48

5.1 Transmissivity T_p of Moxtek RCV8N2EC polarizer in the wavelength range 350-1100 nm. Dashed lines give the confidence range of the measurements. 53
5.2 Transmissivity T_s of Moxtek RCV8N2EC polarizer in the wavelength range 350-1100 nm. Dashed lines give the confidence range of the measurements. 53
5.3 Reflectivity R_p of Moxtek RCV8N2EC polarizer with a 10° AOI in the wavelength range 350-1100 nm. Dashed lines give the confidence range of the measurements. 54
5.4 Reflectivity R_s of Moxtek RCV8N2EC polarizer with a 10° AOI in the wavelength range 350-1100 nm. Dashed lines give the confidence range of the measurements. 54
5.5 Contrast ratio of Moxtek RCV8N2EC polarizer. 55
5.6 Malus' curve of Moxtek RCV8N2EC polarizer transmissivity for specific wavelengths. 56
5.7 Malus' curve of Moxtek RCV8N2EC polarizer reflectivity for specific wavelengths. 56
5.8 Comparison between measured and datasheet values of the reflectivity R_p of Moxtek RCV8N2EC polarizer as function of the incident angle for specific wavelengths. 57
5.9 Comparison between measured and datasheet values of the reflectivity R_s of Moxtek RCV8N2EC polarizer as function of the incident angle for specific wavelengths. 58
5.10 Transmissivity T_p of Moxtek UBB01A polarizer in the wavelength range 350-1100 nm. Dashed lines give the confidence range of the measurements. 59
5.11 Transmissivity T_s of Moxtek UBB01A polarizer in the wavelength range 350-1100 nm. Dashed lines give the confidence range of the measurements. 59
5.12 Reflectivity R_p of Moxtek UBB01A polarizer with a 10° AOI in the wavelength range 350-1100 nm. Dashed lines give the confidence range of the measurements. 60
5.13 Reflectivity R_s of Moxtek UBB01A polarizer with a 10° AOI in the wavelength range 350-1100 nm. Dashed lines give the confidence range of the measurements. 60
5.14 Contrast ratio of Moxtek UBB01A polarizer. 61
5.15 Malus' curve of Moxtek UBB01A polarizer transmissivity for specific wavelengths. 62
5.16 Malus' curve of Moxtek UBB01A polarizer reflectivity for specific wavelengths. 62

5.17 Comparison between measured and datasheet values of the reflectivity R_p of Moxtek UBB01A polarizer as function of the incident angle for specific wavelengths. 63
5.18 Comparison between measured and datasheet values of the reflectivity R_s of Moxtek UBB01A polarizer as function of the incident angle for specific wavelengths. 63
5.19 Transmissivity T_p of Polarcor Wide Band polarizer in the wavelength range 350-1100 nm. Dashed lines give the confidence range of the measurements. 65
5.20 Transmissivity T_s of Polarcor Wide Band polarizer in the wavelength range 350-1100 nm. Dashed lines give the confidence range of the measurements. 65
5.21 Zoom of the transmissivity T_s of Polarcor Wide Band polarizer in the wavelength range 500-1100 nm. Dashed lines give the confidence range of the measurements. 66
5.22 Reflectivity of Polarcor Wide Band polarizer with an AOI of 10° at 0°, 45° and 90° polarization angle, in the wavelength range 350-1100 nm. 66
5.23 Contrast ratio of Polarcor Wide Band polarizer. 67
5.24 Reflectivity of Polarcor Wide Band polarizer considering an AOI of 10°, 15° and 20°, in the wavelength range 350-1100 nm. 67
5.25 Malus' curve of Polarcor Wide Band polarizer transmissivity for specific wavelengths. 68
5.26 Transmissivity T_p of Moxtek RCV8N2EC, Moxtek UBB01A, Polarcor Wide Band polarizers, in the wavelength range 350-1100 nm. Dashed lines give the confidence range of the measurements. 69
5.27 Transmissivity T_s of Moxtek RCV8N2EC, Moxtek UBB01A, Polarcor Wide Band polarizers, in the wavelength range 350-1100 nm. Dashed lines give the confidence range of the measurements. 69
5.28 Reflectivity R_p of Moxtek RCV8N2EC, Moxtek UBB01A, Polarcor Wide Band polarizers with a 10° AOI, in the wavelength range 350-1100 nm. Dashed lines give the confidence range of the measurements. 70
5.29 Reflectivity R_s of Moxtek RCV8N2EC, Moxtek UBB01A, Polarcor Wide Band polarizers with a 10° AOI, in the wavelength range 350-1100 nm. Dashed lines give the confidence range of the measurements. 71
5.30 Absorption A_p of Moxtek RCV8N2EC, Moxtek UBB01A, Polarcor Wide Band polarizers. 72
5.31 Absorption A_s of Moxtek RCV8N2EC, Moxtek UBB01A, Polarcor Wide Band polarizers. 72
5.32 Contrast ratio of Moxtek RCV8N2EC, Moxtek UBB01A, Polarcor Wide Band polarizers. 73
5.33 Topography of Moxtek RCV8N2EC wire-grid structure and its roughness parameters. 75

5.34 2D plot of the Moxtek RCV8N2EC wires height as a function of the sampling length. 76
5.35 Topography of Moxtek UBB01A wire-grid structure and its roughness parameters. 77
5.36 2D plot of the Moxtek RCV8N2EC wires height as a function of the sampling length. 78
5.37 Topography of Polarcor Wide Band polarizer and its roughness parameters. 79
5.38 2D plot of the Polarcor Wide Band polarizer roughness as a function of the sampling length. 80
5.39 Deformation of the analyzed system when subjected to 56g inertial load along the positive x-axis. 81
5.40 Deformation of the analyzed system when subjected to 56g inertial load along the positive y-axis. 82
5.41 Deformation of the analyzed system when subjected to 56g inertial load along the positive z-axis. 82
5.42 Deformation of the analyzed system when subjected to 56g inertial load along the negative z-axis. 82
5.43 Von Mises stress distribution on the analyzed system when subjected to 56g inertial load along the positive x-axis. 83
5.44 Von Mises stress distribution on the glue layers when subjected to 56g inertial load along the positive x-axis. 84
5.45 X-component of the stress tensor acting on the glue layers when subjected to 56g inertial load along the positive x-axis. 85
5.46 Y-component of the stress tensor acting on the glue layers when subjected to 56g inertial load along the positive x-axis. 85
5.47 Zoom on one of the vertical/horizontal glue layers to highlight the X and Y-component stress tensor on the most critical glue area, when subjected to 56g inertial load along the positive x-axis. 86
5.48 Deformation of the analyzed system when subjected to a 100 μm displacement of one of the pinned nodes. 87
5.49 Von Mises stress distribution on the analyzed system when subjected to a 100 μm displacement of one of the pinned nodes. 87
5.50 Von Mises stress distribution on the glue layers when subjected to a 100 μm displacement of one of the pinned nodes. 87
5.51 X-component of the stress tensor acting on the glue layers when subjected to a 100 μm displacement of one of the pinned nodes. 88
5.52 Y-component of the stress tensor acting on the glue layers when subjected to a 100 μm displacement of one of the pinned nodes. 88

8.1 Electromagnetic spectrum. 97

8.2 Transmissivity of Moxtek RCV8N2EC polarizer in the wavelength range 350-1100 nm, as a function of the polarization angle. 103
8.3 Reflectivity of Moxtek RCV8N2EC polarizer in the wavelength range 350-1100 nm, as a function of the polarization angle. 104
8.4 Reflectivity R_p of Moxtek RCV8N2EC polarizer with a 15° AOI, in the wavelength range 350-1100 nm. Dashed lines give the confidence range of the measurements. 104
8.5 Reflectivity R_s of Moxtek RCV8N2EC polarizer with a 15° AOI, in the wavelength range 350-1100 nm. Dashed lines give the confidence range of the measurements. 105
8.6 Reflectivity R_p of Moxtek RCV8N2EC polarizer with a 20° AOI, in the wavelength range 350-1100 nm. Dashed lines give the confidence range of the measurements. 105
8.7 Reflectivity R_s of Moxtek RCV8N2EC polarizer with a 20° AOI, in the wavelength range 350-1100 nm. Dashed lines give the confidence range of the measurements. 106
8.8 Transmissivity of Moxtek UBB01A polarizer in the wavelength range 350-1100 nm, as a function of the polarization angle. 106
8.9 Reflectivity of Moxtek UBB01A polarizer in the wavelength range 350-1100 nm, as a function of the polarization angle. 107
8.10 Reflectivity R_p of Moxtek UBB01A polarizer with a 15° AOI, in the wavelength range 350-1100 nm. Dashed lines give the confidence range of the measurements. 107
8.11 Reflectivity R_s of Moxtek UBB01A polarizer with a 15° AOI, in the wavelength range 350-1100 nm. Dashed lines give the confidence range of the measurements. 108
8.12 Reflectivity R_p of Moxtek UBB01A polarizer with a 20° AOI, in the wavelength range 350-1100 nm. Dashed lines give the confidence range of the measurements. 108
8.13 Reflectivity R_s of Moxtek UBB01A polarizer with a 20° AOI, in the wavelength range 350-1100 nm. Dashed lines give the confidence range of the measurements. 109
8.14 Von Mises stress distribution on the analyzed system when subjected to 56g inertial load along the positive y-axis. 109
8.15 Von Mises stress distribution on the glue layers when subjected to 56g inertial load along the positive y-axis. 110
8.16 X-component of the stress tensor acting on the glue layers when subjected to 56g inertial load along the positive y-axis. 110
8.17 Y-component of the stress tensor acting on the glue layers when subjected to 56g inertial load along the positive y-axis. 110

8.18 Von Mises stress distribution on the analyzed system when subjected to 56g inertial load along the positive z-axis. 111
8.19 Von Mises stress distribution on the glue layers when subjected to 56g inertial load along the positive z-axis. 111
8.20 X-component of the stress tensor acting on the glue layers when subjected to 56g inertial load along the positive z-axis. 111
8.21 X-component of the stress tensor acting on the glue layers when subjected to 56g inertial load along the positive z-axis. 112
8.22 Von Mises stress distribution on the analyzed system when subjected to 56g inertial load along the negative z-axis. 112
8.23 Von Mises stress distribution on the glue layers when subjected to 56g inertial load along the negative z-axis. 112
8.24 X-component of the stress tensor acting on the glue layers when subjected to 56g inertial load along the negative z-axis. 113
8.25 Y-component of the stress tensor acting on the glue layers when subjected to 56g inertial load along the negative z-axis. 113
8.26 Deformation of the analyzed system when subjected to a 100 μm displacement of one of the pinned nodes. 113
8.27 Von Mises stress distribution on the analyzed system when subjected to a 100 μm displacement of one of the pinned nodes. 114
8.28 Von Mises stress distribution on the glue layers when subjected to a 50 μm displacement of one of the pinned nodes. 114
8.29 X-component of the stress tensor acting on the glue layers when subjected to a 50 μm displacement of one of the pinned nodes. 114
8.30 Y-component of the stress tensor acting on the glue layers when subjected to a 50 μm displacement of one of the pinned nodes. 115

Listing of tables

1.1 Summary of EnVisS characteristics. 12

2.1 General Specifications of Moxtek's RCV8N2EC and UBB01A polarizing filters, given by the manufacturer. 21
2.2 General Specifications of Polarcor Wide Band polarizing filter, given by the manufacturer. 23

4.1 Material properties used in the model. 47

6.1 EnVisS main milestones. EFM, STM and PFM stand for Electrical/Engineering Functional Model, Structural and Thermal Model, and Proto-Flight Model respectively. 91

Listing of acronyms

ADC . . . . . Analog-to-Digital Converter

AFM . . . . . Atomic Force Microscope

AOGNC . . . . . Attitude, Orbit, Guidance and Navigation Control

AOI . . . . . Angle of Incidence

AR . . . . . Anti-Reflective

ARIEL . . . . . Atmospheric Remote-sensing Infrared Exoplanet Large-survey

CNR-IFN . . . . . Italian National Research Council – Institute for Photonics and Nanotechnologies

CoCa . . . . . Comet Camera

CR . . . . . Contrast Ratio

DFP . . . . . Dust Field and Plasma instrument

DNC . . . . . Dynamically New Comet

EFM . . . . . Electrical/Engineering Functional Model

EnVisS . . . . . Entire Visible Sky

ESA . . . . . European Space Agency

FEA . . . . . Finite Element Analysis

FEM . . . . . Finite Element Method

FM . . . . . Flight Model

FoV . . . . . Field of View

FSA . . . . . Filter Strip Assembly

HI . . . . . Hydrogen Imager

ISO . . . . . Interstellar Object

JAXA ..... Japan Aerospace Exploration Agency

JFC ..... Jupiter-Family Comets

LPC ..... Long Period Comet

MANiaC ..... Mass Analyzer for Neutrals in a Coma

MPC ..... Multi-Point Constraints

MTF ..... Modulation Transfer Function

MIRMIS ..... Modular InfraRed Molecules and Ices Sensor

NAC ..... Narrow Angle Camera

NAVCAM ..... NAVigation CAMera

OHB-IT ..... Orbitale Hochtechnologie Bremen (Italia)

OPIC ..... Optical Periscope for Comets

P/L ..... Payload

PS ..... Plasma Suite

PSPD ..... Position Sensitive Photodetector

RBE2 ..... Rigid Body Elements Type 2

RoHS ..... Restriction of Hazardous Substances Directive

RMA ..... Rotating Mirror Assembly

SEL2 ..... Sun-Earth Lagrange Point 2

SNR ..... Signal to Noise Ratio

SPM ..... Scanning Probe Microscopy

STM ..... Structural and Thermal Model

TA ..... Transmission Axis

TAS-UK ..... Thales Alenia Space (UK)

TCM ..... Trajectory Correction Manoeuvre

WAC ..... Wide Angle Camera

1 Introduction

Comets are the most primitive objects in the Solar System. They are mainly composed of dust, water ice and carbon-based compounds which proves that these bodies were formed at large distances from the Sun and have been preserved at low temperatures since their creation. The chemical constituents of cometary material are a key element to better understand the conditions that occurred when our Solar System and Sun were formed [1].

It is reasonable to say that there are billions, or even trillions, of comets orbiting the Sun in the Kuiper Belt[1] and in the Oort Cloud[2]. Up to date, the comets that have been studied in situ are thought to be originated in the former region and have all low-activity and short-period (Jupiter-Family Comets, JFCs), with the exception of 1P/Halley [2]. It is believed that all these objects have made several thousands of returns to the perihelion and so they have undergone surface compositional and morphological modification, and blanketing of the nucleus by thick layers of dust. On the other hand, the Oort Cloud might contain a significant amount of icy bodies that have orbits so long that they had passed through the inner solar system thousands of years ago. Other comets of this region have never even ventured close to the Sun in the billions of years since they formed. Being the most preserved objects in the Solar System, these bodies, called Dynamically New Comets (DNCs), provide the

[1]The Kuiper Belt is a donut-shaped region of remnants from the Solar System's early history, beyond the orbit of Neptune.

[2]The Oort Cloud is the most distant region of our Solar System and is believed to be a giant spherical shell surrounding the Sun, the planets and the Kuiper Belt Objects, containing a significant amount of icy bodies.

unique opportunity to investigate the unaltered pristine materials from which our system generated.

It is also known that a population of these dynamically new objects leave the Solar System, since their paths are perturbed into hyperbolic orbits and thus escape the solar influence. Consequently, it has been assumed that there is a similar population of bodies that enter the Solar System from interstellar space. If intercepted, these Interstellar Objects (ISOs) would provide the opportunity of sampling primordial material formed around a star different from our Sun and thus in different condition with respect to those generated in our Solar System.

As of recent years, hundreds of short-period comets are known and have been observed at a minimum of two passes through perihelion. In contrast, thousands of Long Period Comets (LPC) have been observed, many of which are dynamically new, but they have never been encountered by a space mission. The first expedition that will accomplish this goal is *Comet Interceptor*.

1.1 Comet Interceptor

Comet Interceptor is the first European Space Agency (ESA) Fast mission. This multi-point mission is dedicated to the encounter and the exploration of an as-yet unknown target at an unknown future time. Its scientific task is to gather valuable information regarding comet morphology, composition, and plasma environment. This will provide new insights on the formation and evolutionary path of comets, and, more generally, on the condition of the early stages of the Solar System formation.

1.1.1 Mission analysis

The launch of Comet Interceptor is planned for the end of 2029. It will be a shared launch with ESA mission ARIEL[3] on an Ariane 62, where Comet Interceptor will be the upper passenger of the Dual Launch Configuration, and ARIEL the lower one [2].

After the takeoff Comet Interceptor will perform a direct transfer to a large amplitude quasi-Halo orbit around the Sun-Earth Lagrange Point 2 (SEL2). Both the geometry of the transfer and the amplitude of the orbit will depend on the launch date and time, but it is already foreseen that the injection orbit will be a 9° inclined high-apogee, nearly parabolic orbit, with perigee at 180 km altitude and apogee at 1.5×10^6 km. Generally, quasi-Halo

[3] ARIEL, Atmospheric Remote-sensing Infrared Exoplanet Large-survey.

orbits around SEL2 have a period of 180 days, amplitude of around 1 million km and are intrinsically unstable.

Once entered in the parking orbit, Comet Interceptor will be orbiting around SEL2 for an unknown amount of time, possibly between few months and 4 years. During this time, periodic station keeping manoeuvres are planned to avoid an exponential deviation of the spacecraft from the reference orbit. Thanks to the spacecraft's ability to reduce dynamic noise and velocity perturbations, the manoeuvres are scheduled every 28 days with a Δv of 2.3 m/s per year.

While Comet Interceptor waits in the quasi-Halo orbit, the ground based observatories are expected to discover potential targets for the mission. It is predicted that many icy bodies will be found through routine observation outside the orbit of Uranus, giving at least five years lead-up time before the comet reaches perihelion. As each new object is discovered, it will be evaluated if it is a feasible potential encounter candidate for Comet Interceptor. The foreseen target that the mission aims to study is either a Dynamically New Comet, thus a comet entering the inner Solar System for the first time that retains the majority of its original volatiles, or an Interstellar Object originating at another star. In the event that no suitable DNC or ISO is discovered, the best available Long Period Comet will be the mission's target. In the worst case scenario for which also no potential candidate LPC is found, Comet Interceptor will be encountering one of the Jupiter Family's comets.

Once the target is selected, Comet Interceptor will orbit around SEL2 until the right conditions to start the transfer are presented. For each potential candidate object, the possible transfer trajectories and encounter profiles will be analyzed in detail for at least 6 months before initiating the manoeuvres. To avoid unnecessary Δv, the target comet will be intercepted at one of its nodal crossings of the Ecliptic plane. Consequently, the encounter location can be defined by 2 parameters: the heliocentric distance, R_C, and the phase angle of Earth[4], θ.

The transfer orbit has been studied with the 2-body dynamics under solar gravity considering that when the spacecraft leaves the vicinity of SEL2 also the gravity effect of Earth has an important impact. Two different strategies have been proposed to perform this manoeuvre: a direct transfer and a moon gravity assist.

With the former strategy, Comet Interceptor will exit the gravitational pull of the Earth-Moon system by leaving the quasi-Halo orbit and entering a heliocentric one. During this transfer towards the comet, a second deep-space manoeuvre might be necessary to adjust the

[4]The phase angle θ is measured as the Comet-Sun-Earth angle.

orbit and the phasing. The second strategy foresees a Moon fly-by after which the spacecraft can escape the gravitational pull of the Earth-Moon system. The Moon fly-by introduces operational complexity, but allows Δv savings and is an efficient way to reach heliocentric orbits with perihelion below 1 AU.

Depending on the chosen strategy, this transfer phase could last between a few months and 3-4 years. Moreover, Comet Interceptor will probably slightly adjust the transfer trajectory to fly-by a non-active minor body in order to engineering testing the spacecraft optical navigation cameras and autonomous tracking required for the actual comet fly-by. This would increase the mission robustness and probability of success of the science fly-by.

The encounter phase, which is assumed to last 60 days, is the final stage before the comet fly-by. Since it is predicted that deterministic manoeuvres would not be needed, during this phase operations can focus on the navigation required to the comet approach. This navigation will rely on ground-based measurements of the comet's position, on radio tracking of the spacecraft and on the optical data from the NAVCAM, which can directly relate the positions of spacecraft and comet, thus allowing to perform critical trajectory correction manoeuvres (TCMs) and improving the accuracy of the prediction of the fly-by location and time.

In the last three days before the closest approach, final operations (still subjected to optimization and refinement) will take place. During this phase, Comet Interceptor will proceed towards the target comet up to a distance of 1000 km and will deploy two sub-probes that will follow different trajectories through the coma at distances of 850 km and 400 km. The result will be unique, simultaneous, spatially resolved information of the 3-dimensional properties of the target comet.

Finally, there will be a six-month, post-encounter phase for data transmission to Earth, followed by de-commissioning and post-operations.

1.1.2 Scientific Objectives

As previously mentioned, Comet Interceptor overall scientific task is to provide the first investigation of a DNC and to sample simultaneously different regions of the coma. To achieve this goal, the scientific requirements that need to be met are the measurements of the cometary nucleus properties, and the coma connection to the nucleus and its interaction with the solar wind. These two scientific themes will be addressed as Nucleus and Coma Science, respectively. Furthermore, detailed observation of the surface and the coma will be combined to monitor changes in the cometary activity.

The first theme focuses on finding out what are the DNC's nucleus characteristics, i.e. its rotation rate, surface composition, shape, morphology and structure. This task is accomplished by in-situ measurements and sampling. The collected information will provide unique insights into early surface evolution and constraints for surface features' formation timescales. Additionally, since few impacts are expected in the Oort Cloud, potential impact craters, depressions, layers, regolith and boulders on the comet surface might provide an unmodified record of early bombardment in the Solar System, other than a unique insight into the early Solar System's accretion processes and the characteristics of primordial small planetesimals.

A comparison between Comet Interceptor target and short-period comets encountered by previous missions would show the differences between a pristine object and one subjected to significant changes due to its passages through the perihelion. The characterization of the differences and the similarities between the two objects would be invaluable. Moreover, composition measurement of the surface might provide information about the chemical processing as comets evolve.

On the other hand, the Coma Science investigates the composition of the gas and dust in the coma, the connection between the latter and the nucleus, and how it interacts with the solar wind.

The observation of the gas, dust and plasma are linked to each other and to the studies of the nucleus through the process of cometary activity. Measurements of the composition and distribution of volatile species in the coma will give useful insights regarding the difference between the activity process of a DNC and that of a more evolved body. In particular, Comet Interceptor will collect data about the relative abundances of molecules of high volatility, such as CH_4, CO and CO_2, with respect to water; find out if there is evidence of hyperactivity (i.e., significant activity being driven by sublimation from icy 'chunks' in the coma) and if there are differences in isotopic composition. For each of these topics, ESA Fast mission will test if the phenomenon is related to comet's evolution or not.

One of Comet Interceptor peculiarities is its multi-spacecraft configuration which gives it the ability to perform observations of the coma from three different positions at the same time, thus describing coma's properties in a 3-dimensional way. Finally, Energetic Neutral Atom (ENA) observations will be used to complete the multi-point in-situ plasma measurements in order to give an insight of which plasma variations are due to external influences by providing a continuous observation of the variability of the solar wind.

1.1.3 Payload

To perform multi-point observations during the fly-by of the target object, Comet Interceptor will be composed of three modules: a main spacecraft (S/C A) and two sub-probes (B1 and B2). Both S/C A and Probe B2 are developed by ESA and two possible designs have been considered during the phase B study: one developed by TAS-UK[5] led consortium and one by OHB-IT[6] led consortium; while Probe B1 is developed by JAXA[7].

The payload of spacecraft A will consist of a High resolution Comet Camera (CoCa) and a Rotating Mirror Assembly (RMA), a Mass spectrometer (MANiaC), a Dust Field and Plasma instrument suite (DFP-A), and an IR multi-spectral imager (MIRMIS). The proposals of both constructors for the S/C A feature:

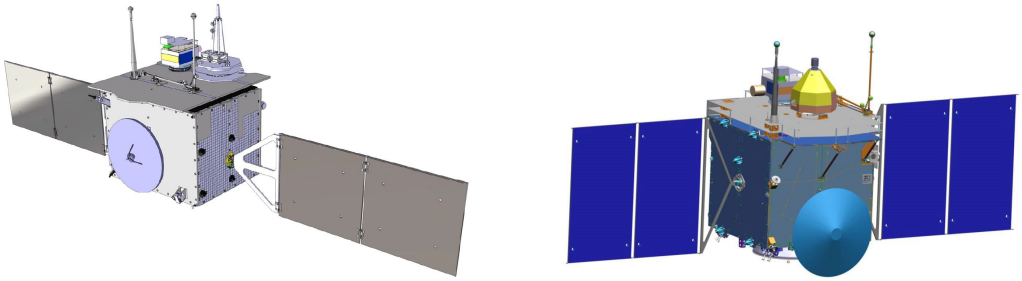
- Cuboid shape, hosting all platform equipment and accommodating both probes (on the same side) and the payload;
- Two deployable solar arrays;
- The Attitude, Orbit, Guidance and Navigation Control (AOGNC) subsystem, including different sensors and actuators;
- The chemical propulsion system with a large Δv capability;
- Fixed High-Gain X-band Antenna;
- Thermal control system;
- Dust shield.

The two different designs of S/C A developed by TAS-UK and OHB-IT are shown in Figure 1.1.

Probe B1 is a small craft, 3-axis stabilised, with flat, cuboid shape and without propulsion capability. Its payload consists of a Hydrogen Imager (HI), a Narrow Angle Camera (NAC), a Wide Angle Camera (WAC) and a Plasma Suite (PS). The probe has a total mass of approximately 35 kg and typical size of 0.5 m. B1 will feature:

- Dedicated Attitude, Guidance and navigation sub-system using payload units;
- Electrical power system based on deployable solar arrays and a secondary battery;
- Communication system working in S-band to transmit and receive data/commands with the main spacecraft;
- Dust shield protecting the probe during the comet encounter.

[5]TAS-UK, Thales Alenia Space (UK).
[6]OHB-IT, Orbitale Hochtechnologie Bremen (Italia).
[7]JAXA, Japan Aerospace Exploration Agency.



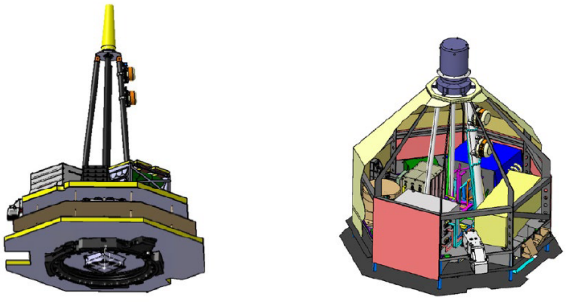
(a) TAS-UK **(b)** OHB-IT

Figure 1.1: Comet Interceptor Spacecraft A design (Phase B).

Like B1, Probe B2 is a small craft without propulsion and attitude control capability, with a total mass of 35 kg. This probe has an axisymmetric shape with typical diameter of 0.5 m and is spin-stabilised. It is equipped with an Entire Visible Sky Polarimetric camera (EnVisS), a Low resolution camera (OPIC) and a Dust Field and Plasma instrument suite (DFP-B). The probe configurations of both constructors are similar and include:

- Power system based on a primary battery;
- Communication system working in S-band to transmit and receive data/commands with the main spacecraft;
- Dust shield protecting the probe during the encounter;
- Operational lifetime of approximately 30 hours.

The two different designs of B2 developed by TAS-UK and OHB-IT are shown in Figure 1.2.



(a) TAS-UK **(b)** OHB-IT

Figure 1.2: Comet Interceptor Probe B2 design (Phase B).

With the beginning of the mission Phases C, D and E1, in January 2023, the designs of

S/C A and Probe B2 developed by OHB-IT led consortium have been selected.

As previously illustrated, the scientific objectives of the mission can be divided in two main themes: Nucleus and Coma Science.

For the Nucleus theme, Comet Interceptor will return visible and near infrared images from three different view points, given by S/C A and both probes.

The highest resolution images (with resolution of 10 m/pixel) will come from CoCa on Spacecraft A, which will track the nucleus through the fly-by. The other images will be taken by both NAC and WAC visible cameras on Probe B1 (which will take photos of the nucleus and its surroundings from a fixed orientation during the closest approach), and by OPIC on Probe B2 (which will provide images of the nucleus and of the inner coma from a different angle shortly before closest approach). These images will provide useful information regarding the size, shape, and surface morphology of the target comet nucleus. Its rotation rate will be constrained by both resolved imaging and images of the unresolved nucleus by CoCa in the days before and after the flyby.

Insights about the nucleus composition will come from multi-colour imaging from both CoCa and MIRMIS, and from point spectroscopy in the 2.5-5 μm range in MIRMIS. The latter will also provide unique information about the surface layers thermal inertia via thermal-infrared imaging. Moreover, insights into the physical properties of the surface layers will come from visible wavelength polarimetry measurements by EnVisS.

Regarding the Comet Environment Theme, Comet Interceptor will measure in-situ the coma composition, including measurements of isotopic ratios, by means of MANiaC.

MIRMIS will provide gas composition measurements through remote sensing, while HI will monitor the cometary water production rate.

CoCa, WAC, OPIC and EnVisS will investigate the spatial distribution of dust from three different viewpoints. Furthermore, the EnViSS all-sky imager on Probe B2 will constrain dust properties through polarimetric measurements, while the DISC and DFP instruments will measure the mass distribution of dust particles colliding with both Spacecraft A and Probe B2.

The magnetic field of the comet will be measured simultaneously by magnetometers on all three spacecraft, in order to analyze the interaction between solar wind and cometary plasma. Moreover, plasma properties will be measured by three spectrometers (DFP) and an ion mass spectrometer (PS).

1.2 EnVisS

EnVisS (Entire Visible Sky) is an all-sky camera designed to fly on Comet Interceptor's spin stabilized Probe B2.

The instrument, of which the CNR-IFN[8] of Padua, Italy, is the Principal Investigator (PI), features an optical head, composed of ten lenses, connected to a commercial space-qualified detector developed by 3D-Plus company, and to ad-hoc data and power units and software. Moreover, EnVisS adopts a filter strip assembly (FSA), composed of one broadband filter and two polarimetric ones, to be mounted as close as possible to the detector, making the camera compact and with low mass and complexity.

Due to scientific requirements and technical instrument constraints, the imager will study the target comet dust environment and polarimetric properties in the visible spectrum (wavelength range of 550-800 nm). The analysis will be conducted from a point inside the coma itself and will last for the full fly-by of the comet.

EnVisS will be placed with its optical axis perpendicular to the Probe B2 spin-axis, which will be pointed at the comet nucleus for most of the time. A representation of this configuration is shown in Figure 1.3a.

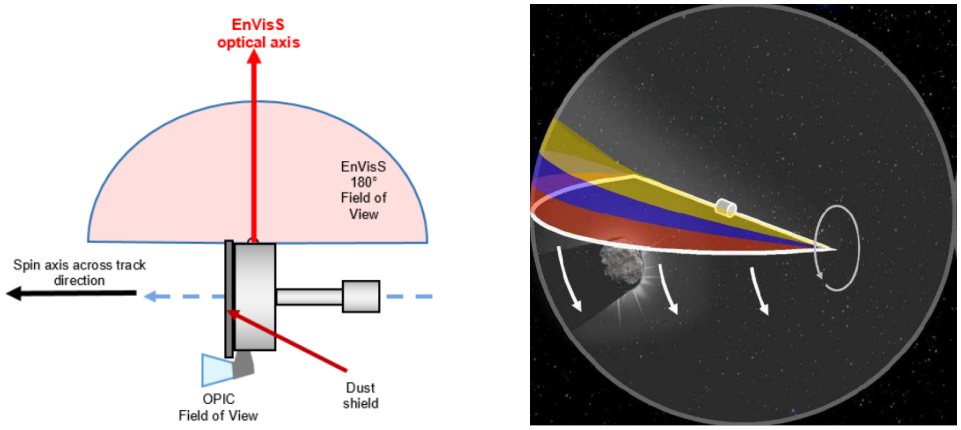
The fish-eye camera is characterized by an instantaneous wide field of view (FoV) covering a 180×45 solid angle, with the ± 90 FoV in the across track direction and the 45 FoV in the along track direction. Thanks to the spinning of the Probe B2, EnVisS images in scanning motion the entire sky, with a dynamic FoV of 180×360 (see Figure 1.3b). While the probe rotates (with a baseline spin rate of 15 rpm, thus a spin period of 4 seconds [3]), EnVisS will continuously acquire images. This technique is called push-frame imaging and it allows the acquisition of slices of the sky, which will be stitched together, on-ground, to form an image of the whole scene surrounding the probe. Therefore, EnvisS will be able to embody the coma, jets and gases of the comet in a single image.

The all-sky camera will measure the intensity, the degree of linear polarization and polarization angle orientation of the light scattered by the dust particles in the comet coma with a full 180 phase angle coverage [2]. To achieve the desired signal to noise ratio (SNR), the map of the coma will be taken with different angular resolution[9], depending on the cometary activity.

EnVisS optical head is composed of 10 lenses and has a 3.45 mm focal length; the camera

[8] CNR-IFN, Italian National Research Council – Institute for Photonics and Nanotechnologies.

[9] The minimum resolution element is 0.2.



(a) EnVisS placement on B2 and its static FoV.

(b) EnVisS dynamic FoV and B2 spinning motion.

Figure 1.3: EnVisS placement configuration and its field of view.

modulation transfer function (MTF) is 70% at 45 lp/mm. The mechanical structure is made of titanium and invar; the EnVisS mechanical design foresees also two light baffles to prevent straylight from light sources outside the nominal FoV. A prototype of EnVisS fish-eye lens optical head will be realized by Leonardo SpA in Campi Bisenzio, Florence (Italy).

As previously mentioned, the filter strip assembly is mounted very near to the detector and is needed to study the radiance and the polarization properties of the comet's coma diffused light [4]. The FSA is composed of three filter strips glued side by side, all working in the same wavelength range but having different optical properties. The central strip is a high transmission broadband (BB) with no polarization properties, while the side ones are linear polarization filters with the same transmission bandpass as the BB and with polarization axis at 45 from one another. The unused areas of the FSA will be covered by a black coating to minimize scattering.

The detector is a CMOS monochrome sensor CMV4000 by AMS-OSRAM and consists of 2048 $\times$ 2048 pixels with a pitch of 5.5 μm. The manufacturer will mount a 0.55 mm thick D263 glass window above the sensor that functions as mechanical optically transparent shield.

The assembly composed by the sensor and the relative electronics will be then manufactured by 3D-Plus and is shown in Figure 1.4.

The required signal to noise ratio is of at least 10 for the broadband images and of at least 100 for the polarimetric ones. Since in 1 ms exposure time the expected acquired signal is

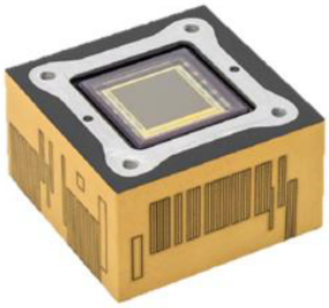
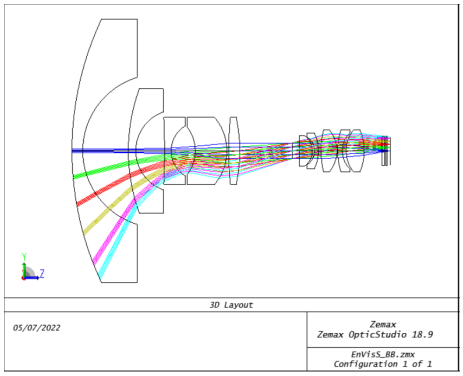


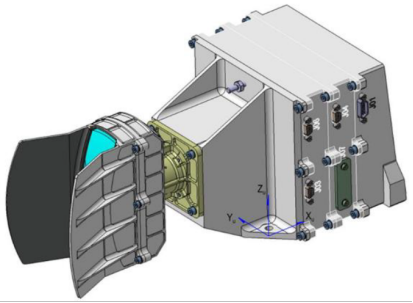
Figure 1.4: 3D-Plus package composed by the CMOS monochrome sensor and glass window (manufactured by AMS-OSRAM) and its electronics.

too low to satisfy the required SNR, a flexible approach has been adopted. In fact, the comet signal along the direction of the apparent motion is not expected to change too much, so it is not really necessary to have a very high resolution along this direction. Thus, accepting some smearing in the direction of the rotation of the scene, longer exposure times can be used. At the same time, angular resolution can be preserved in the across-track direction, assuring a sampling of comet phase function every 0.1. With this strategy, if the radiance of the coma is different from the expected one, adjustments of the exposure time can be made. A further increase of the SNR can also be achieved through pixel binning, on-board, or co-adding of the images in successive spacecraft rotation, on-ground.

In Figure 1.5 a schematic ray-tracing along the optical head to the sensor and a 3D CAD model of EnVisS, courtesy of Leonardo SpA, are illustrated, while EnVisS main characteristics are reported in Table 1.1.



(a) Schematics of the ray-tracing along the optical head to the sensor.



(b) 3D CAD model of EnVisS.

Figure 1.5: EnVisS ray-tracing configuration and its CAD model.

Filters	1 broadband and 2 polarimetric filters
Wavelength Range	550-800 nm
Instrument FoV	180×45 (Fixed) 180×360 (Dynamic)
Pixel scale (IFOV)	0.1/px
Entrance Aperture	1.23 mm
F/ #	2.8
Focal Length	3.45 mm
MTF	$> 70\%$ at 45 lp/mm
Distortion	$< 8\%$
Telecentricity	< 4

Table 1.1: Summary of EnVisS characteristics.

2
Polarizing Filters

In the previous chapter a general view of the Comet Interceptor mission and its all-sky camera EnVisS has been given. Henceforward, the focus of this work will be entirely on the fish-eye camera filter strip assembly (FSA) which is one of the key elements to study the radiance and the polarization properties of the comet's coma in the visible light wavelength range[1]. Before going into detail about the FSA, an overview on the polarization properties of the light is necessary.

2.1 Polarization

2.1.1 Polarization Ellipse

The vectorial nature of light is called polarization [5]. In the most general case, when the electromagnetic waves propagate through space, the electrical and magnetic field constantly change their amplitude and orientation.

For simplicity, to study this behaviour of light, only the electric field $\vec{E}$ will be considered, given that the magnetic one is always perpendicular to it.

Considering an electromagnetic wave propagating along the z-axis, a generic electrical field

[1] A brief explanation of the definition of light and the electromagnetic spectrum is illustrated in Appendix 8.1

can be represented by two different components (see Figure 2.1):

$$E_x(z,t) = E_{0x}\cos(kz - \omega t + \delta_x)$$
$$E_y(z,t) = E_{0y}\cos(kz - \omega t + \delta_y)$$

where E_{0x}, E_{0y} are the maximum amplitude of the x and y components, δ_x and δ_y are their phases at $(z,t) = (0,0)$.

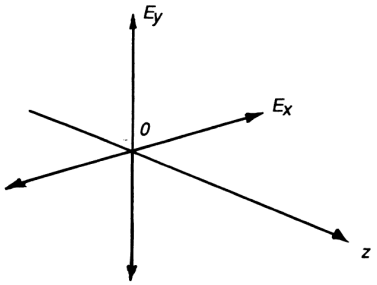


Figure 2.1: Propagation of the transverse optical field.

As the field propagates, the vector generally describes a locus of points in space, generating a curve of elliptic shape, given by[2]:

$$\frac{E_x^2}{E_{0x}^2} + \frac{E_y^2}{E_{0y}^2} - 2\,\frac{E_x\,E_y}{E_{0x}\,E_{0y}}\cos(\delta_y - \delta_x) = \sin^2(\delta_y - \delta_x)$$

This behaviour is commonly known as optical polarization and the previous equation is called the polarization ellipse.

For certain values of E_{0x}, E_{0y} and $\delta = \delta_y - \delta_x$, the polarization ellipse degenerates into special forms.

If $E_{0x} = 0$ and $E_{0y} \neq 0$, the field oscillates only in the y-direction and the light is said to be linear vertically polarized (considering the system of reference in Figure 2.1). Similarly, if $E_{0y} = 0$ and $E_{0x} \neq 0$, the field oscillates only in the x-direction and it gives linear horizontally polarized light.

When $\delta = 0, \pi$ the polarization ellipse reduces to

$$\frac{E_x^2}{E_{0x}^2} + \frac{E_y^2}{E_{0y}^2} \pm 2\,\frac{E_x\,E_y}{E_{0x}\,E_{0y}} = 0 \quad\Longrightarrow\quad \left(\frac{E_x}{E_{0x}} \pm \frac{E_y}{E_{0y}}\right)^2 = 0 \quad\Longrightarrow\quad E_y = \pm\left(\frac{E_{0y}}{E_{0x}}\right)E_x$$

[2]The mathematical steps to obtain this equation are illustrated in Appendix 8.2

which is the equation of a straight line with slope $\pm E_{0y}/E_{0x}$, hence, linearly polarized light with a certain slope. If $\delta = 0$ the slope will be positive, otherwise negative. In the particular case for which $E_{0x} = E_{0y}$, the light will be linearly polarized at $\pm 45°$.

If the phase difference δ is $\pm\pi/2$, the polarized ellipse equation reduces to that of a standard ellipse which is not rotated with respect to the coordinate system. In addition, if $E_{0x} = E_{0y} = E_0$ the equation reduces to

$$\frac{E_x^2}{E_0^2} + \frac{E_y^2}{E_0^2} = 1$$

which is the equation of a circle. The light is then said to be right or left circularly polarized when $\delta = \pi/2$ and $\delta = 3\pi/2$ respectively.

This description of light in terms of the polarization ellipse is very useful because it enables us to describe by means of a single equation various states of polarized light. Nonetheless, this representation is inadequate for several reasons.

The polarization ellipse is a very useful representation of the light behaviour since it allows the description of the various states of polarized light in one equation. However, this characterization is unsuitable for measurements of the light properties considering that it presents two main issues.

First of all, it is observed that when the beam of light that propagates through space crosses a perpendicular plane, the light vector traces out an ellipse (or some special form of it) in a time interval of the order of 10^{-15} seconds. This short period of time clearly prevents the observation of the polarization ellipse.

Furthermore, the polarization ellipse cannot be used to describe unpolarized or partially polarized light, but only light that is completely polarized. Since, in nature, light is very often unpolarized or partially polarized, this limitation is very restrictive.

For these reasons, another description of polarized light, in which only observed or measured quantities are present, is needed.

2.1.2 Stokes Parameters

In the mid 1800s, Sir G. G. Stokes discovered that the polarization behaviour of light could be described by four measurable quantities [5]. The first parameter represents the total irradiance of the optical field, while the remaining three quantities describe the polarization state of light. These four observables now take the name of Stokes parameters.

Moreover, Stokes defined unpolarized light as the light whose intensity is unaffected when a polarizer is rotated (see Paragraph 2.1.3) or when a retarder is placed along its path.

Stokes also proved that his parameters give a complete description of unpolarized light and of any of its polarization state, and they are exactly the measured quantities.

As previously mentioned, the polarization ellipse is valid only for any given instant of time, hence, a more precise definition of the equation would be:

$$\frac{E_x^2(t)}{E_{0x}^2(t)} + \frac{E_y^2(t)}{E_{0y}^2(t)} - 2\,\frac{E_x(t)\,E_y(t)}{E_{0x}(t)\,E_{0y}(t)}\cos\delta(t) = \sin^2\delta(t)$$

where $\delta(t) = \delta_y(t) - \delta_x(t)$

Considering E_{0x}, E_{0y} and δ constant over time, and E_x and E_y implicitly dependent on it, to represent the equation in terms of the observable of the optical field, an average over the observation time is needed. Then, through several mathematical steps, shown in Appendix 8.3, the previous analytical expression can be reduced to:

$$(E_{0x}^2 + E_{0y}^2)^2 - (E_{0x}^2 - E_{0y}^2)^2 - (2\,E_{0x}\,E_{0y}\cos\delta)^2 = (2\,E_{0x}\,E_{0y}\sin\delta)^2$$

From which the Stokes parameters are:

$$\begin{cases} S_0 = E_{0x}^2 + E_{0y}^2 & = I \\ S_1 = E_{0x}^2 - E_{0y}^2 & = Q \\ S_2 = 2\,E_{0x}\,E_{0y}\cos\delta & = U \\ S_3 = 2\,E_{0x}\,E_{0y}\sin\delta & = V \end{cases}$$

where

- S_0 is the total irradiance of light;
- S_1 is the amount of irradiance of light which is linear horizontal or vertical polarized;
- S_2 is the amount of irradiance of light which is linear $\pm 45°$ polarized;
- S_3 is the amount of irradiance of light which is left or right circular polarized.

For any state of polarized light the Stokes parameters always satisfy

$$S_0^2 \geq S_1^2 + S_2^2 + S_3^2$$

The light is considered completely polarized whenever the total intensity is equal to the sum of the other three quantities, whereas is unpolarized or partially polarized if S_0 is greater than

the sum of the remaining Stokes parameters.

The polarization state of light can then be identified by a four-parameter vector which is called Stokes vector for a plane wave and is given by $S = (S_0\, S_1\, S_2\, S_3)^T$. All these polarization state vectors are defined in Appendix 8.3.

2.1.3 Polarizers

Polarized light can be generated, changed and manipulated to fit one's needs. These operations can be carried out by means of particular optical devices called polarizers.

A polarizer is an instrument whose input is any source of light and whose output is some form of polarized light [6].

These optical devices come in many different configurations, but they are all based on one of four fundamental physical mechanisms: dichroism (or selective absorption), reflection, scattering and birefringence (or double refraction). All of these mechanisms allow the polarizers to select a particular polarization state and discard all the others, which can be achieved by a form of asymmetry associated with the polarizer itself.

For the purpose of this work, only a few of the selective absorption techniques will be illustrated.

The term dichroism refers to the selective absorption of one of the two field components of an incident beam. The polarizers whose functional mechanism is selective absorption are physically anisotropic, producing a preferential absorption direction of one component while being transparent to the other.

The simplest optical device that uses selective absorption is the wire-grid polarizer, which consists of a grid of parallel conducting wires. The conduction along the individual wires is the basic concept of these polarizers [7].

Considering an unpolarized light beam incident on the grating, the electric field of the electromagnetic radiation (which can be resolved into two orthogonal components[3]), interacts with the wires.

The component of the field parallel to the wires causes electrons to oscillate along the length of each one of them, thus generating a current. As the electrons oscillate they transfer their energy from the field to the grid and radiate in both the forward and the backward directions. The incident wave tends to be canceled by the re-radiated wave in the forward

[3] In this example the two components are chosen to be one parallel to the wires and the other perpendicular to them.

direction, while the radiation propagating in the backward direction appears as a reflected wave.

On the other hand, the electrical field perpendicular to the wires does not interact much with the electrons, thus the wave remains unaltered as it propagates through the grid, transmitting the polarized light (see Figure 2.2). The transmission axis of the grid is perpendicular to the wires.

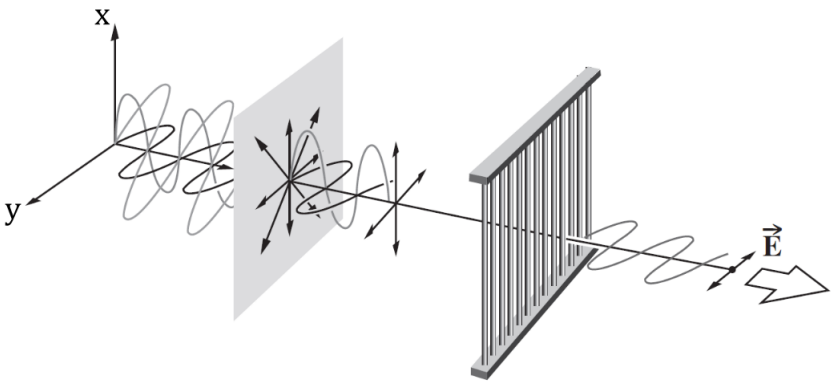


Figure 2.2: Functioning of a wire-grid polarizer: when unpolarized light incident on the polarizer, polarization with electric field parallel to wire grid is reflected and polarization with electric field perpendicular to the wire grid is transmitted.

Other optical devices that use the selective absorption mechanism are polarizers whose materials are inherently dichroic because of an anisotropy in their respective crystalline structures [6].

These types of materials have a specific direction within the crystal determined by their atomic configurations which identifies their principal or optic axis. The electrical field component of an incident beam that is orthogonal to this axis is strongly absorbed by the material, thus, the principal axis corresponds to the polarizer's transmission axis.

Due to crystal properties, the elastic binding forces on the electrons will be different as a function of the direction, hence, the response of these particles to the electric field of an incident electromagnetic wave will vary with the direction of $\vec{E}$.

The absorption increases with the crystal thickness: the thicker the crystal, the more complete the absorption. On the other side, though, also the transmitted light suffers a certain amount of absorption, and this absorption is strongly wavelength dependent.

2.2 EnVisS polarization filters candidate

In the Comet Interceptor mission, the polarization properties of the comet's coma diffused light will be analyzed thanks to the two polarizer filter strips composing the filter package (FSA) of the EnVisS camera.

It has been described how there are different types of optical elements that can be used to achieve a polarization state. Consequently, to establish which type of polarizer best meet EnVisS requirements, a preliminary characterization[4] of different sample filters has been carried out in the CNR-IFN laboratories.

The analyzed filters are Moxtek visible light polarizer RCV8N2EC and ultra broadband UBB01A, and Polarcor Wide Band polarizer.

2.2.1 Moxtek RCV8N2EC and UBB01A

Moxtek polarizing filters RCV8N2EC and UBB01A are both designed with Moxtek Nanowire Technology to control light and image polarization even in high energy and high temperature applications [8], [9]. They feature a wire-grid polarizer surface on one side (Paragraphs 5.2.1, 5.2.2) which, as previously explained, consists of a metallic grating with a period smaller than the wavelength for which the polarizer is used [10].

Moxtek polarizers feature highly durable materials, thus offering pure polarization that gives high contrast and bright images for the life of the instrument. Furthermore, these filters have excellent polarization uniformity over large apertures and the degree of polarization depends little on wavelength and angle of incidence.

The polarizer samples used for the characterization measurements are D-mount (circular frame). The mounts have been tested for durability and are made of 6061 anodized aluminum. The frame has been developed to protect the polarizers, making it easier to handle them without damaging the wire-grid.

The mounts also show two reference marks (white lines) on one face which act as indicator for the transmission axis of the filter, which is perpendicular to the wire-grid.

In Figure 2.4 are shown the two sides of Moxtek polarizers, while in Table 2.1 their specifications are reported.

[4] The preliminary characterization of the polarizers will be described in Chapter 3.

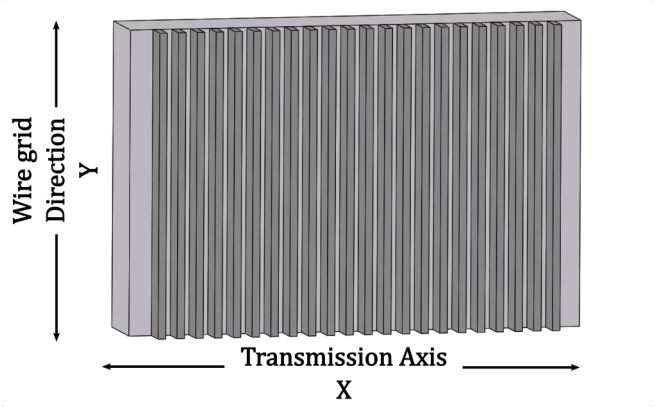


Figure 2.3: Moxtek polarizing filters general wire-grid configuration.



(a) RCV8N2EC **(b)** UBB01A

Figure 2.4: Moxtek polarizing filters.

The first thing that can be pointed out from the table is the different wavelength range in which the polarizers work: UBB01A has a bandwidth larger than 2900 nm while RCV8N2EC has a nominal working bandwidth smaller than 300 nm. Since EnVisS's purpose is to image the whole comet coma in the visible range and the filters are used to study the radiance and the polarization properties of the comet's coma diffused light in the spectral range of 550-800 nm, it can already be observed that between the two Moxtek polarizing filter UBB01A might be preferred.

Another argument in favour of the UBB01A polarizer is its type of substrate. Fused silica, in fact, has unique optical, mechanical, and thermal properties, such as: high chemical purity and resistance, high softening temperature and thermal resistance, low thermal expansion with high resistance to thermal shocks, high transparency from the UV and IR spectral range and high radiation resistance. Moreover, this material has been strongly assessed for space environment and has flight heritage. Since it is already foreseen that the substrate of the

central broadband filter of the FSA is fused silica, polarizing filters with the same substrate would be preferred.

	RCV8N2EC	UBB01A
Wavelength Range [nm]	420-700	300-$\geq$ 3200
Substrate Type	Display Grade Glass	Fused Silica
Thickness [mm]	0.7 ± 0.07	1.0 ± 0.1
Index of Refraction	1.5198 (435.8 nm) 1.5078 (643.8 nm)	1.4672 (430 nm) 1.4504 (1000 nm)
Thermal Expansion $[10^{-7}/°C]$	31.7 (0-300°C)	5.5
Angle of Incidence (AOI) [°]	0 ± 20	0 ± 20
Anti-Reflective (AR) Coating	Standard on backside only	Not standard
Maximum Temperature	200°C, $>$ 5000 hours	200°C, $>$ 5000 hours
Transmission Axis (TA)	Referenced to long side of part	Referenced to long side of part
TA Tolerance [°]	± 1	± 1
Dimensional Tolerance	± 0.2	± 0.4
Edge Exclusion [mm]	2	2
RoHS	Compliant	Compliant

Table 2.1: General Specifications of Moxtek's RCV8N2EC and UBB01A polarizing filters, given by the manufacturer.

Nonetheless, each filter has been evaluated, and its properties have been analyzed and compared both with the other filters' ones and with the transmissivity and reflectivity provided by the manufacturer (see Chapter 5).

2.2.2 Polarcor Wide Band

Polarcor Wide Band Polarizer is based on selective absorption thanks to its material anisotropy. The polarization mechanism of this filter consists in a resonant absorption of light by elongated silver crystals within the glass material. Because of its solid glass, this optical device offers excellent optical properties and is extremely resistant to chemical, physical and thermal damage, therefore presenting optimal performance, durability and stability in harsh environments [11]. In Table 2.2 Polarcor Wide Band Polarizer specifications are reported.

It can be observed that Polarcor Wide Band polarizer has a nominal working wavelength range of 500 nm, which is wider than Moxtek's RCV8N2EC, but smaller than UBB01A. Also, the minimum operational wavelength is 600 nm, while EnVisS will study the diffused light in the range of 550-800 nm. Moreover, the substrate material used for this polarizing filter is the borosilicate glass [12], which is a suitable material for space applications.

Polarcor filter has no mount, but once the measurements on this filter were finished the polarizer has been mounted into a standard laboratory mounting frame for easy handling and protection, as it can be seen in Figure 2.5



Figure 2.5: Polarcor Wide Band Polarizer.

	POLARCOR WIDE BAND
Polarization Bandwidth [nm]	600-1100
Substrate Type	Borosilicate Glass Containing Elongated Silver Crystals
Thickness [mm]	0.50 ± 0.05
Index of Refraction at Wavelength Bandwidth	1.5218-1.5107
Coefficient of Thermal Expansion CTE $[10^{-6}/°C]$	6.5
Angle of Incidence (AOI) [°]	0 ± 5
RoHS	Compliant
Contrast	>10000:1
Extinction Ratio [dB]	>40
Transmittance (%) without AR-Coated	>60.0
Insertion Loss [dB] without AR-Coated	<2.20
Transmittance (%) with 2 sides AR-Coated	>66.0
Insertion Loss [dB] with 2 sides AR-Coated	<1.8
Reflectance (%) per each side	<1.0

Table 2.2: General Specifications of Polarcor Wide Band polarizing filter, given by the manufacturer.

3

Optical Analysis

The Padua branch of the CNR-IFN has a wide experience in metrology for space instrumentation and has a laboratory dedicated to reflectivity and transmissivity optical measurements. Consequently, the polarizing filters described in Chapter 2 have been optically characterized at the Padua Institute for Photonics and Nanotechnologies facilities.

The purpose of this analysis is to establish which one between EnVisS polarizing filters' candidates is the most suitable for the all-sky camera scientific task.

At first, the polarizers optical properties (in terms of transmissivity[1] and reflectivity[2]) have been evaluated by means of a Bentham Reflectometer. For every filter, data have been collected, analyzed and compared with the other polarizers' one and also with the specifications provided by the manufacturer (see Chapter 5).

Moreover, the surface morphology of the polarizing filters has been studied by means of the Atomic Force Microscope (XE-70, Park System). As it will be shown later, this analysis is particularly relevant to evaluate the features of the Moxtek filters since they present a nanometric wire-grid structure, while for the Polarcor polarizer the focus of this analysis is on its coating's roughness.

Both laboratories setups and measurements will be described in this chapter.

[1]Transmissivity, or transmittance, is the percentage of light that passes through a surface or an optical element. It is expressed as the ratio of the transmitted to the incident radiation of light.

[2]Reflectivity, or reflectance, is the percentage of light that is reflected from a surface or an optical element. It is expressed as the ratio of the reflected to the incident radiation of light.

3.1 Bentham Reflectometer

A reflectometer is an optical instrument used to measure the transmitted or reflected signal of a light beam passing through an object or being reflected by it as a function of the light's wavelength.

As previously mentioned, to test the optical properties of the polarizer candidates for the EnVisS camera, a Bentham Reflectometer has been used.

3.1.1 Instrument configuration

The Bentham instrument has triple diffraction gratings which allows the measurements of transmissivity and reflectivity of optical components in the UV, visible and NIR spectral range, i.e., in the 200-1800 nm wavelength range [13].

The instrument setup features four different units: lamp unit, monochromator unit, measurement station and electronic unit (see Figure 3.1).

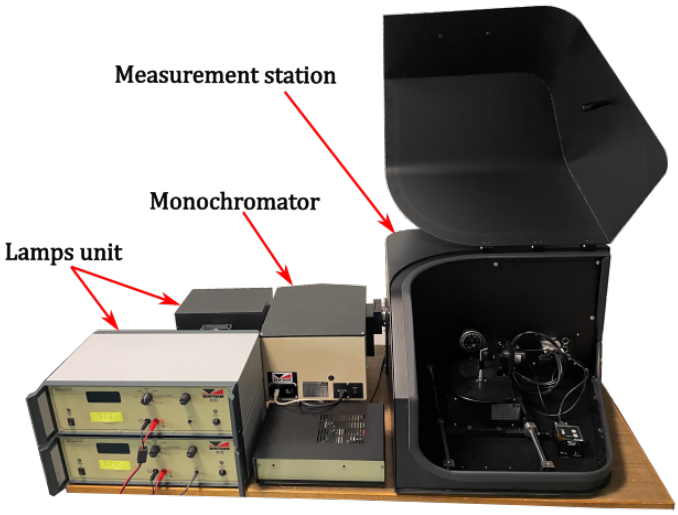


Figure 3.1: Main units of the Bentham Reflectometer.

The illumination system consists of two different light sources with an optomechanical interface for automatic source selection. The first is a 75 W short arc Xenon lamp (250-1500 nm), while the second is a 100 W quartz halogen lamp (250-3000 nm).

The spectral selection is realized by the monochromator, which has a focal length of 300 mm and can host up to three different gratings on a motorized column and up to six different

filters on a motorized filter wheel. For the analysis object of this work, the monochromator mounts two plane ruled gratings, respectively blazed at 500 nm and 750 nm and both with a groove density of 1200 g/mm, and two long-pass order sorting filters, centered at 400 nm and 700 nm.

A light-proof measurement station hosts an optical breadboard compatible with various types of optical elements and mechanisms. In the current settings, a single axis goniometer with independent motorized sample holder and a detector stage are present.

Lastly, various electronic units control the different items and a current amplifier with an integrated Analog-to-Digital Converter (ADC) module.

3.1.2 Laboratory setup and Measurement procedure

Measurements of the transmissivity and reflectivity have been performed at standard temperature and pressure, by two different operators.

Preliminary analysis has shown that the light provided by the monochromator of the Bentham Reflectometer is partially polarized. In order to properly characterize the polarizing filters object of this study, the light incident on the filters themselves must be totally polarized. For realizing a totally polarized light beam incident of the filters under test, one of the three available Moxtek RCV8N2EC polarizers has been mounted along the optical path just in front of the sample stage on a motorized precision rotation stage (Thorlabs PRM1Z8).

In addition, the sample stage given by Bentham has been replaced by an ad hoc realized holder, made in the CNR-IFN laboratory, in which a 30 mm cage rotation mount (Thorlabs CRM1/M) with 2° dial graduations labeled every 20° has been installed.

A view of the optical breadboard, goniometer, sample/detector stages and motorized rotation mount is shown in Figure 3.2.

This equipment can be employed for measurements of both transmissivity and reflectivity with different angles of polarization and different angles of incidence.

Since both optical properties to be measured are given by the ratio of the transmitted/reflected signal to the incident one, the measurement of the incident beam intensity is necessary.

Incident signal

The measurement of the incident light beam intensity has been carried out with the goniometer rotated by 180° from its home position and by detecting the signal passing through the

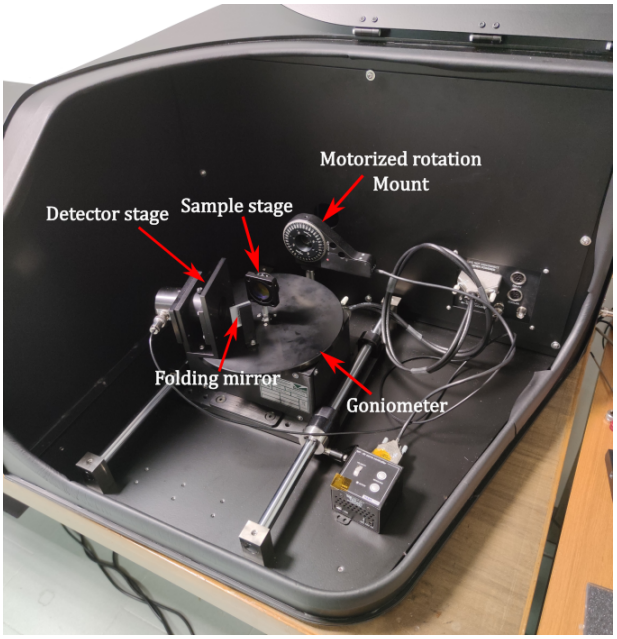


Figure 3.2: View of the optical breadboard, goniometer, sample/detector stages and motorized rotation mount.

empty sample holder (the described configuration is the one represented in Figure 3.2 where the sample stage has been removed).

As previously mentioned, the monochromator light is partially polarized; hence, to detect an almost completely polarized light with maximum incident signal intensity, different measurements have been carried out changing the orientation of the RCV8N2EC polarizing filter mounted along the reflectometer optical path.

Since the aim of these tests is only to find the orientation for which the RCV8N2EC polarization axis is aligned to the one of the partially polarized light produced by the monochromator, the signal has been measured in a small spectral range (550-600 nm) with step size of 5 nm. The optimal filter orientation[3] has been easily found by means of the BenWin+ Spectral Acquisition software[4].

Once the right orientation of the Moxtek polarizer has been found, measurements of the incident signal have been carried out. These measurements have been realized over the 350-1100 nm spectral range with a step size of 1 nm. An example of the measured signal is shown

[3]The orientation of the RCV8N2EC polarizer inside the motorized rotation mount has been fixed throughout all the samples characterization, with exception of the measurement of the reflectivity R_s, as described later.

[4]BenWin+ is a dedicated spectral acquisition software package, that provides seamless control and data acquisition across the wavelength range selected.

in Figure 3.3.



Figure 3.3: Example of the measured incident signal in the wavelength range 350-1100 nm.

During the first detections, it has been observed that the monochromator light source is not stable throughout the day due to environmental conditions (such as temperature and humidity) and to the lamp functioning itself. In particular, it has come to notice that the signal stabilizes after the first half hour of operation. Thus, for every measurement session the incident signal intensity has been measured 45 minutes after the activation of the reflectometer, in between different types of analysis, and at the end of the session. By doing so, it has been possible to compute the desired optical properties by dividing the transmitted and reflected signal by the most accurate incident one. In particular, the first measurements of the transmitted/reflected signal have been divided by the first detected incident signal; the last transmitted and reflected signals have been divided by the last detection of the incident beam; and the intermediate measurements have been divided by an average of the first and last incident signal.

Transmitted signal

To evaluate the transmitted signal, the configuration setup is similar to the one described to measure the intensity of the incident beam. The only difference is that the configuration includes the sample stage which holds the polarizing filter under test and that it must be set

perpendicular[5] to the incident light beam produced by the monochromator (see Figure 3.4).

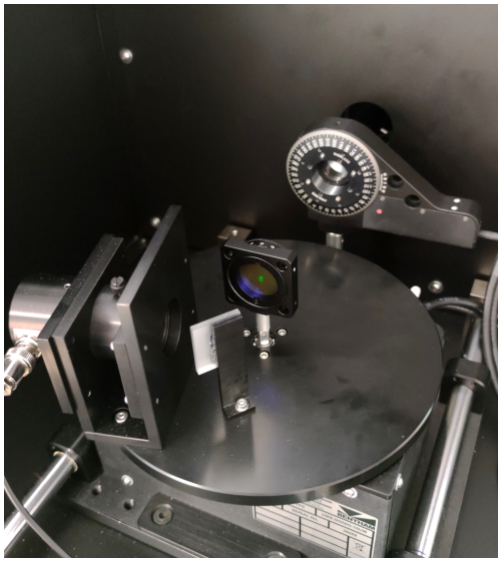


Figure 3.4: Configuration set up for the transmissivity measurements.

Once the right configuration has been set up, the polarization axes of the RCV8N2EC and of the sample filter have been aligned by rotating the cage rotation mount. Then, the detection of the transmitted signal has taken place.

As for the incident beam, the measurements of the signal have been taken over the 350-1100 nm spectral range with a step size of 1 nm. The transmitted signal has been detected with the light beam always perpendicular to the polarizing filter under test, which, measurement by measurement, has been rotated from 0° to 180° with 15° step size. Lastly, another measurement of the signal with the polarization angle at 0° has been taken to compare it to the initial one.

With these operations the polarization axis of the filter has been rotated by 180° (and then back to its initial configuration), allowing the generation of the Malus curve[6] for each considered wavelength. Thanks to this curve it has been possible to check whether the polarizer has symmetric behaviour or not.

Even though the tests have been run over a wide range of polarization angles, the most relevant for the analysis are those corresponding to the transmissivity T_p and T_s. The former is

[5]The correct alignment of the polarizer with respect to the monochromator light beam has been found using the back reflection technique.

[6]The Malus' curve is the transmissivity or reflectivity curve as a function of the polarization angle (α), which follows the trend of $\cos^2\alpha$.

the transmissivity when the incident radiation is fully polarized with a polarization direction parallel to the polarizer axis, while the latter is the transmissivity when the incident radiation is totally polarized with a polarization direction perpendicular to the polarizer axis.

The procedure has been repeated for each polarization filter that needed characterization (i.e., Moxtek RCV8N2EC and UBB01A, and Polarcor Wide Band) and for both sides of the polarizers.

Reflected signal

To measure the reflected signal, two different orientations of the RCV8N2EC polarizer mounted on the motorized rotation stage have been used, based on whether the object of the analysis was the reflectivity R_p or R_s. Just like for the transmissivity, R_p is the reflectivity when the incident radiation is fully polarized with a polarization direction parallel to the polarizer's axis. On the other hand, R_s is the reflectivity when the incident radiation is fully polarized with a polarization direction perpendicular to the polarizer's axis.

For the R_p reflectivity detection, the measurements have been performed in the configuration θ-2θ, where θ is the incident angle of the radiation on the sample and it has been considered equal to 10°, 15° and 20°. The orientation angle of the sample holder has been found setting the filter perpendicular to the incident beam (as it has been done for the transmissivity using the back reflectivity technique) and then rotating the stage by θ. On the other hand, the goniometer rotational angle is equal to 2θ, thus, moving the detector by the same angle (see Figure 3.5).

For Moxtek's polarizing filters RCV8N2EC and UBB01A, the measurements have been taken over the 350-1100 nm spectral range with a step size of 1 nm. For θ = 10°, 15°, the signal reflected by the filter on the sample stage has been measured at a polarization angle ranging from 0° to 180° with step size of 15° and, as done for the transmissivity, another measurement with the polarization angle at 0° has been taken. Since enough data had been already collected to generate the Malus' curve (and thus proving the symmetric behaviour of the polarizers), for θ = 20° it has been chosen to detect the signal only to a few significant polarization angles, i.e., 0°, 85°, 90°, 95°, 180° and then again 0°.

Since Polarcor's Wide Band Polarizer is based on selective absorption due to its material anisotropy, the reflection signal is independent of the polarization angle of the reflective sample, and so it has been studied for each incidence angle θ with a polarization angle equal to 0°, 45°, 90°.

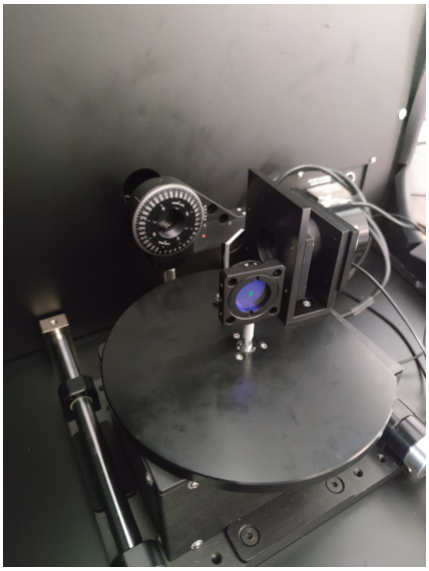


Figure 3.5: Configuration set up for the reflectivity measurements for $\theta = 10°$.

Regarding the reflectivity R_s, the setup and procedure is the same as for R_p, with the difference that the RCV8N2EC polarizer inside the motorized rotator stage has been rotated by 90° and the only tested polarization angle has been the one for which the relative angle between the RCV8N2EC's polarizing axis and the one in the sample is 90°.

The procedure has been repeated for each face of the polarizing filters.

Error estimation

Every quantity that has been experimentally measured is associated to uncertainties. These errors are due to measurement limitations, such as the instrument precision and sensibility, statistic errors or changes in the operational conditions.

For this reason, a specific error has been associated to every measurement realized with the just described optical analysis as it will be illustrated in this paragraph.

In the most general case, a quantity y is a function of x_j measurable variables, where $j = 1, \ldots, n$. Each measured variable is associated to an error Δx_j, and the uncertainty propagates to the function $y = f(x_i)$. Following the propagating error theory [14], with the appropriate

assumptions, the uncertainty associated to the physical property y is[7]:

$$\Delta f = \sum_{j=1}^{n} \left| \frac{\partial f}{\partial x_j} \right|_{x_j = x_{j0}} \Delta x_j$$

In this work the physical properties analyzed are the transmissivity and the reflectivity, while the variables are the incident signal and the one transmitted or reflected by the sample.

The general function f, representing the transmissivity or the reflectivity, is given by the ratio of either the transmitted or reflected signal, S, to the incident one, I (i.e., $f = S/I$).

Consequently, the error on f is:

$$\Delta f = \left| \frac{\partial f}{\partial S} \right| \Delta S + \left| \frac{\partial f}{\partial I} \right| \Delta I \quad \Longrightarrow \quad \Delta f = \frac{\Delta S}{I} + \frac{S}{I^2} \Delta I$$

where ΔS is the error associated to either the measured transmitted or reflected signal, and ΔI the uncertainty associated to the incident one.

In this optical analysis, the main sources of errors on the measurements are the repeatability and reproducibility.

The repeatability error has been determined by performing a series of measurement cycles in which the incident signal is acquired. By comparing the different curves, it has been found that the repeatability uncertainty is equal to 0.2% [13].

On the other hand, reproducibility measures the degree of agreement of an experiment or study performed by different individuals in different conditions using the same measuring equipment. In this work, the reproducibility error has been evaluated by comparing the maximum transmitted signals detected in different conditions, such as:

- Changing operator;
- Waiting for some time;
- Removing and re-screwing the rotator stage with the polarizer into the fixed base;
- Removing and reassembling the polarizer inside the sample holder.

Signals have been computed from 550 nm to 600 nm with a wavelength step of 5 nm. From the calculation of the average and the standard deviation of these measurements, it has

[7] Since the low number of measurements used for this first order error analysis (15), it has been chosen to consider the maximum error propagation rather than the root mean square.

been possible to obtain the relative error of the measured signals as:

$$\Delta S_{\%} = \frac{\Delta S}{S}$$
$$\Delta I_{\%} = \frac{\Delta I}{I}$$

This value is wavelength dependent but, for simplicity, the same value of relative error has been associated to each wavelength. The considered value corresponds to the average of the calculated relative errors and is equal to σ = 0.79%[8].

Since the repeatability error is small compared to the reproducibility one, for this first order uncertainty analysis, only the reproducibility error has been considered.

Finally, it can be found:

$$\Delta f = \frac{\Delta S_{\%}\, S}{I} + \frac{S}{I^2}\Delta I_{\%}\, I$$

Since the same sensor has been used for the detections it has been assumed that the relative error of the measured signals is the same for the two variables ($\Delta S_{\%} = \Delta I_{\%} = \Delta_{\%}$) and it has been considered a level of confidence of 95% ($\Delta_{\%} = 2\sigma = 1.58\%$). The error associated to the obtained results is

$$\Delta f = 2f\Delta_{\%}$$

Data elaboration

All the data of the different signals have been collected by means of the BenWin+ Spectral Acquisition Software and have been converted into Microsoft Excel spreadsheets.

In the spreadsheets the transmissivity, T, and the reflectivity, R, for all the incident angles and both sides of each polarizer have been calculated.

In addition, the Malus curve, the contrast ratio and the absorption of each polarizer have been computed.

Finally, the results obtained for every filter have been compared with both the results of the other polarizers and the data provided by the manufacturer.

All the results of this optical analysis are illustrated in Chapter 5.1.

[8]The calculated relative errors are in the range between 0.76% and 0.82%, in correspondence of 600 nm and 550 nm wavelength, respectively.

3.2 Atomic Force Microscope

The polarizing filters candidate for EnVisS filter strip assembly have been subjected also to a different type of test, in which their surface morphology has been studied.

To analyze the filters' nanometric structure, the XE-70 Park System Atomic Force Microscope (AFM), available in the CNR-IFN laboratories in Padua, has been used.

Atomic Force Microscopy is a type of Scanning Probe Microscopy (SPM), which consists in a high-resolution, non-optical imaging technique. Generally, SPM refers to a series of techniques that use micro-machined cantilever probes with sharp tips to scan a sample surface and thus characterize it [15].

One of the most common uses of AFM is high resolution and non destructive nanoscale measurements of the topographical properties of a sample surface in air, liquid or ultrahigh vacuum [16].

Generally, an AFM can be used in several modes such as contact AFM, true non-contact AFM, lateral force microscopy, force distance spectroscopy, phase imaging, conductive atomic force (I-AFM) microscopy, electric force microscopy (EFM, DC-EFM, External EFM) and force modulation microscopy.

For the analysis object of this work, the XE-70 Park System AFM has been used in true non-contact mode with Park-approved Nanosensor PPP-NCHR 10M tips.

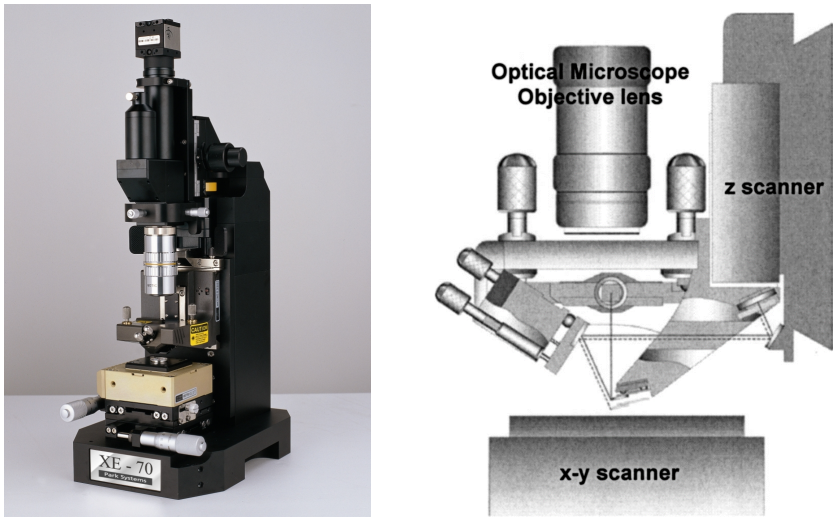
3.2.1 Instrument configuration

The Park System AFM, available in the CNR-IFN laboratories in Padua, is situated inside a hermetically sealed acoustic casing and on a vibration isolation system, to ensure low noise, and thus high resolution imaging [15].

The atomic force microscope features decoupled XY and Z scanner to minimize background curvature, and accomodates samples with diameter up to 100 mm. The XY scanner is a single module parallel-kinematics flexure stage that moves the sample in the xy-plane and has a maximum scan size of 50×50 μm^2 (5×5 μm^2 in low-voltage mode). It also guarantees minimum out-of-plane motion and high orthogonality. On the other hand, the Z scanner is a one-dimensional flexure stage that controls the probe along the z-axis with a range of 12 μm (1.7 μm in low-voltage mode).

This setup also includes direct on-axis optical microscope objective lens with manual Z focus stage.

In Figure 3.6 the AFM used for the analysis is shown.



(a) Microscope picture. **(b)** Microscope sectional diagram.

Figure 3.6: Park System XE-70 Atomic Force Microscope.

This system uses the laser beam bounce detection method (see Figure 3.7). A micromachined cantilever with a sharp tip on the edge is used as a probe and is mounted on a piezoelectric tube that acts as a three-dimensional actuator [17]. The interaction between the tip and the sample causes the cantilever deflection which is then measured by casting a laser on the cantilever and detecting the reflected beam with a position sensitive photodetector (PSPD).

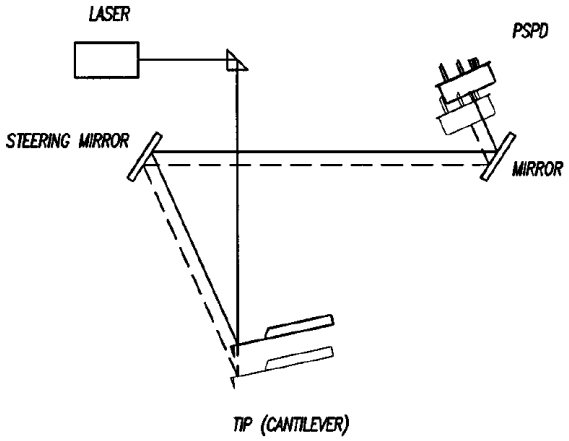


Figure 3.7: Laser beam bounce detection mechanism.

In addition to the laser source, the PSPD, the cantilever and the tip, to perform the laser

beam bounce detection mechanism the AFM probing unit must include also optical components, such as mirrors, lenses and fine screw, in order to achieve the necessary optical alignment. The laser path, in fact, must be adjusted so that the beam correctly falls on the cantilever and hits the center of the photodetector.

As previously mentioned, for the purpose of this work the atomic force microscope has been used in the non-contact mode. In this method the cantilever[9] oscillates at its resonance frequency (or at a near value) with an amplitude of 1 nm or less. The tip is kept at an appropriate distance from the sample surface (usually between a few nanometers and tens of nanometers), such that is included in the region of attractive interaction forces (see Figure 3.8).

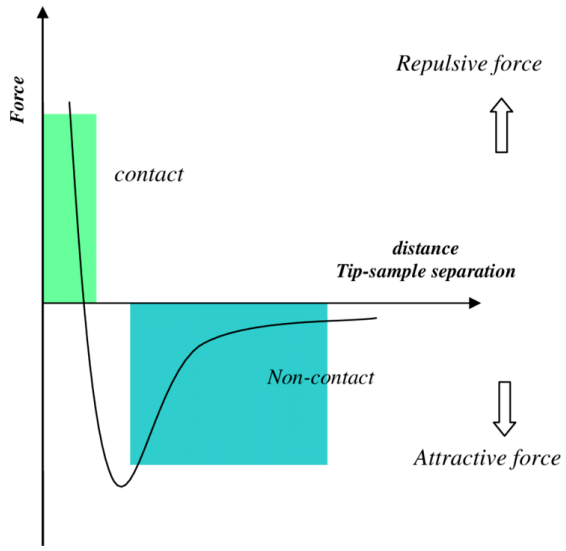


Figure 3.8: AFM tip-sample potential energy representation and related scanning modes.

To obtain the desired distances high performance feedback controls are needed.

Moreover, high resolution imaging is achieved only if the sharpness of the tip is preserved during the measurement. This is guaranteed by the small interaction forces between the tip and the sample surface but, inevitably, after some time the tip wear and contamination make the tip unusable for quality images.

In addition, a lamp unit, a scanning probe controller and monitors are included in the setup.

[9]AFM cantilevers with high force constants and high resonance frequencies are most suitable for non-contact mode.

3.2.2 Measurement procedure

Measurements of the surface morphology of the polarizing filters under examination have been performed at standard temperature and pressure.

First of all, the Scanning Probe Controller and Monitors have been turned on, and the tip has been mounted on the cantilever while the sample has been placed on the stage [18].

Then, after having switched on the Light Bank and Laser, the operations to aim the laser on the end of the cantilever to make it center the photodetector have begun. These operations consist in adjusting the position of the first mirror hit by the laser beam. They can be accomplished by using the uEye Demo software (which, through the optical microscope, allows to see the cantilever and whether the laser hits it near its end or not) and the two knobs that regulate the mirror position.

Afterwards, the adjustment of the second mirror hit by the beam has been performed. This has been accomplished by means of the two knobs dedicated to the positioning of the second mirror and the XEP Data Acquisition Software, in which a schematic view of the photodectector is represented as four quadrants. The software indicates the position of the laser with a red dot and the correct alignment is found when this point is on the center of the PSPD.

The functioning mode, scanning and frequency have then been selected; in particular, for the formers the non-contact mode, XY and Z large scanning have been used. Regarding the frequency, the software automatically detects the cantilever's resonance peak and selects a driving frequency. This value has been manually adjusted depending on each case.

By using the Z-stage control window of the XEP software, the initial approach to the sample surface (within a few microns distance) has been done manually and then, an automatic approach has been performed until the distance between the tip and the surface was the appropriate one to start the imaging.

The image scan size has been set to 1×1 μm^2 and once the scan parameters, such as the Z-servogain, the scan rate, the set point and the drive[10] have been optimized, the imaging has taken place. Once all the data have been collected, the images have been modified and elaborated by means of the XEI Data Analysis Software.

This procedure has been done for all three polarizing filters and the obtained results are shown in Chapter 5.2.

[10]These parameters are optimized to have the trace and retrace of the scanning with the same topography, when the two curves have the same shape, then the scanning produces a high quality image.

4

Finite Element Analysis

So far the optical analysis performed on the EnVisS camera candidate polarizing filters has been illustrated. In this chapter, the focus will be on the structural-mechanical properties of the filter strip assembly.

For this project, in fact, a preliminary Finite Element Analysis (FEA) of the FSA simplified model has been realized to learn if the optical components of the filter package are prone to structural changes, whenever they are subjected to external loads.

The simulation has been carried out by means of the pre-processing software for finite element analysis, Patran, and the post-processing for multiple solvers, MSC Nastran. This solver allows the user to simulate stress, dynamics, or vibration of real-world, complex systems.

Before going into the details of the simulation, an overview on the filter strip assembly features will be described.

4.1 Filter Strip Assembly

The EnVisS camera filter strip assembly is one of the key elements to study the radiance and polarization properties of the comet's coma diffused light. As already described in Chapter 1.2, the filter package will be mounted between the ten-lenses optical head of the camera and the CMOS monochrome sensor. Its design is developed by CNR-Institute for Photonics and Nanotechnologies of Padua and Leonardo SpA.

Currently, the design foresees three filter strips, glued side by side, each having the same operational size of $1.1 \times 12.5 \times 1\ mm^3$ but different optical properties (see Figure 4.1).

The central strip is a high transmission broadband (BB) filter in the range $550 - 800$ nm, with no polarization properties. It is realized on a 1 mm thick fused silica substrate, and has a custom coating, developed by Materion Corporation[1], applied on both surfaces of the filter.

The side strips are linear polarization filters (described in the previous chapters) with the same transmission bandpass as the BB and with polarization axis at 45° from one another to measure the Q and U Stokes components. Since it is foreseen that the most suitable polarizing filters for EnVisS scientific task are Moxtek Ultra Broad Band UBB01A (as it will be shown in Chapter 5), in this analysis the FSA has been considered composed by these polarizers. As described in Chapter 2.2.1, the UBB01A filters have a 1 mm thick fused silica substrate and feature a wire-grid surface on one side, while the other face of the polarizer, in the standard configuration, is uncoated. To protect the wire-grid structure of the polarizing filter, Materion plans to laminate it with an uncoated 1 mm fused silica wafer. This 2 mm thick laminated filter will be then ground and polished down to the desired 1 mm thickness.

The manufacturer also foresees to coat both surfaces of the entire filter strip assembly with the band defining coatings (the proposed deposition materials are ion-assisted Ta_2O_5 and SiO_2).

Considering the coating layer, to maintain the same optical focus position for all the filter strips, a tolerance of $\pm$ 20-30 microns on their thickness has been assumed.

As shown in Figure 4.1, the global size of the FSA is $15 \times 15 \times 1\ mm^3$. The central filter actual size will be of $1.1 \times 15 \times 1\ mm^3$, while the lateral polarizers will be $6.77 \times 15 \times 1\ mm^3$.

The filters will be glued side by side with a 0.18 mm thick layer of adhesive material. This glued region, like the unused part of the filter package, will be covered by a black coating to minimize scattering and give the desired dimensions of the three filter strips.

The instantaneous field of view selected by each filter generates a footprint in the filter plane with diameter of about 0.9 mm. To avoid vignetting over the field of view of each filter, it has been decided to overestimate the dimensions of the filter strips designing them with size equal to $1.1 \times 15 \times 1\ mm^3$.

The external part of the filter package (i.e., the portion external to the centered square of 13.2 mm side) is predicted to be used as the interface between the FSA and its aluminum mounting frame. In future analysis it will be decided if this portion will be completely coated

[1]Materion Corporation is the global provider of high-tech solutions in charge of the realization of the EnVisS FSA.

or not.

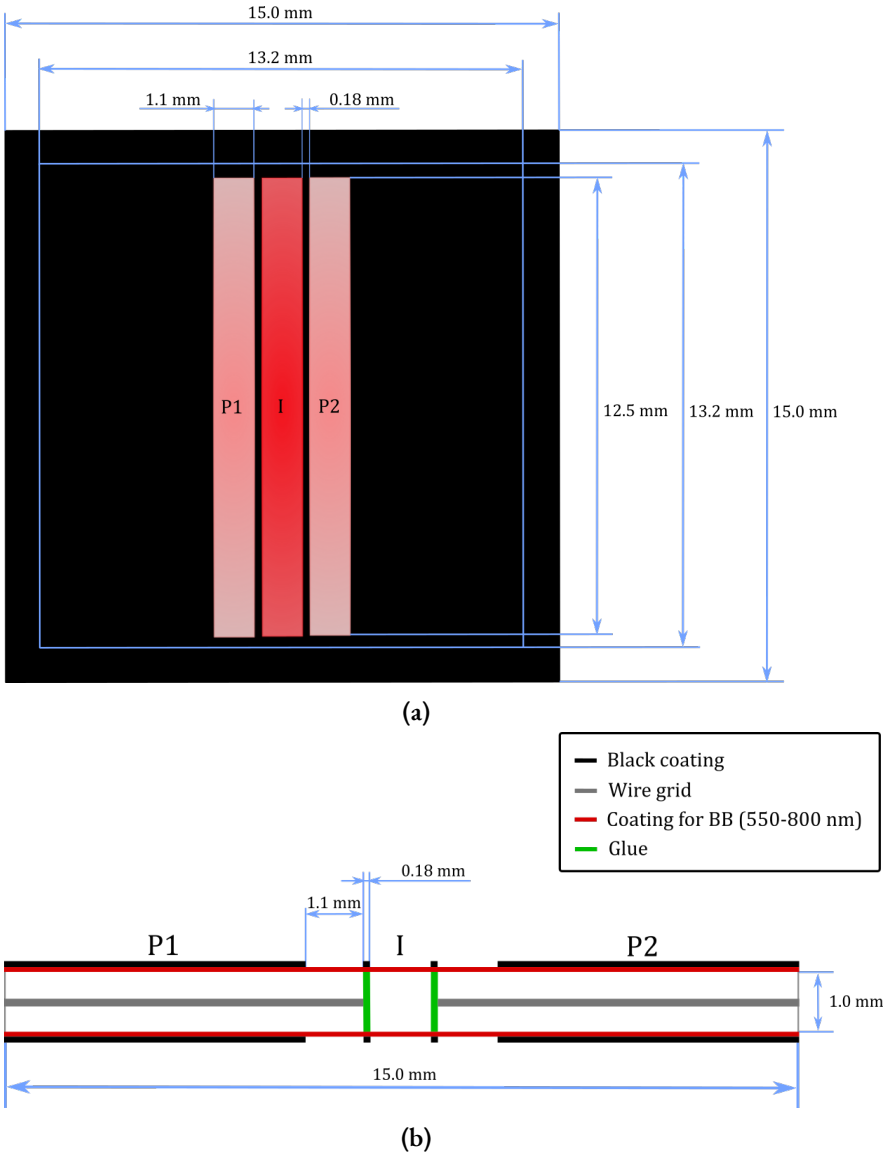


Figure 4.1: Schematic of EnVisS FSA. Note that the two images are not to scale.

The aluminum mounting frame shown in Figure 4.2 is the supporting structure in which the FSA is to be mounted. This frame will link the filter package to the 3D-Plus detector package shown in Figure 1.4 (by means of screws in the four internal threaded holes) and to the remaining part of optical instrument (using screws in the six external threaded holes). The central hole and pin are used for the correct alignment between the FSA and the camera.

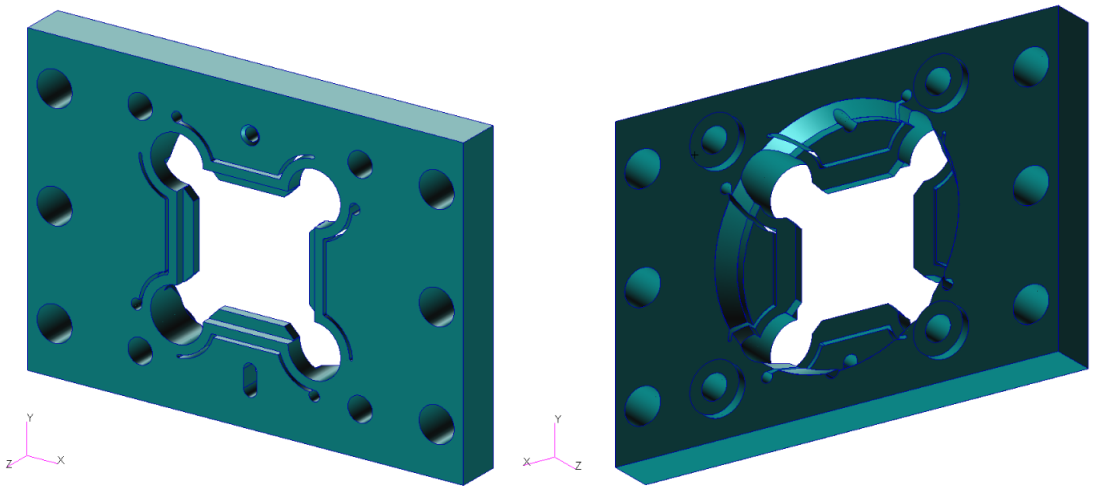


Figure 4.2: CAD model of the aluminum mounting frame, courtesy of Leonardo SpA.

The filter package will be placed in the center of the supporting structure and glued to it with a 0.3 mm thick adhesive material (Ec9323-2, provided by 3M) on the FSA lateral sides (see Figure 4.4).

It can be observed that the structure also presents four flexures which are necessary both to reduce the mounting frame mass and to avoid damaging the FSA due to differential thermal expansions between the filters and the frame, which are made of fused silica and aluminum, respectively (the coefficient of thermal expansion of these materials are reported in Table 4.1).

4.2 Simulation

The subsystem consisting of the filter strip assembly glued to the aluminum mounting frame has been modeled using the pre-processing software, Patran, and its structural-mechanical changes due to different physical phenomena have been simulated with the MSC Nastran post-processing software, which is a Finite Element Analysis (FEA) program. The FEA is the simulation of any physical phenomenon acting on an object using the Finite Element Method (FEM) technique (see Appendix 8.4). This approximate method is used to obtain the solutions of general problems whose physical phenomena are governed by differential equations by dividing a large system into a series of discrete finite elements [19].

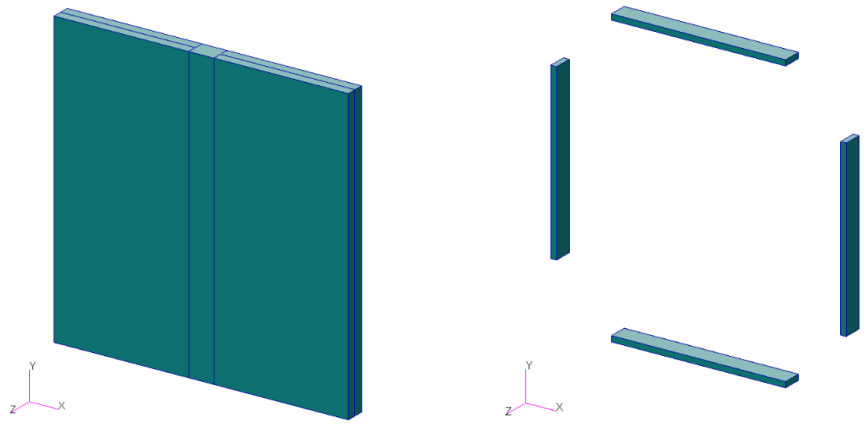
In this chapter, the Patran model of the FSA and supporting frame subsystem will be thoroughly described, while the analysis results obtained with Nastran will be discussed in Chapter 5.3.

To correctly simulate the changes of a system when subjected to a certain type of load, different steps have to be made in the pre-processing software. First, the geometry of each element composing the system has to be defined, then, a mesh and suitable properties (both in terms of material and type of object) have to be associated to each of them. Next, boundary conditions and loads acting on the system have to be set; finally, before launching the simulation, the type of analysis to be performed has to be selected.

The model that has been simulated consists of three main groups: one includes the supporting mounting frame of the filter package, another consists of the five blocks representing the filter strips and the last one is composed of the four glue layers that link the FSA and the mount.

4.2.1 Geometry

The entire system has been modeled with solid objects. The geometry of the supporting structure has been imported from a 3D SolidWorks CAD model, courtesy of Leonardo SpA (see Figure 4.2), while both glue and filter strips have been considered as parallelepipeds with different dimensions and positions with respect to the origin of the system.



(a) Filter strip assembly **(b)** Glue

Figure 4.3: Geometry of the FSA and glue layers.

The filter strip assembly has been simulated as a simplified model composed of five blocks:

one for the central broadband filter and two for each polarizer to highlight the lamination that will be performed by Materion in correspondence of the wire-grid structure. Moreover, for simplicity, the coating layers that cover the entire filter package have been neglected, and the 0.18 mm glue between the central filter and the lateral ones has been considered as an infinitesimal glue layer. Consequently, the filters dimensions have been overestimated, in particular, the central block has been modeled with $1.28 \times 15 \times 1$ mm^3 size and the other four parallelepipeds with dimensions $6.86 \times 15 \times 0.5$ mm^3 (see Figure 4.3a).

The center of the FSA coincides with the center of the supporting structure and between these elements four strips with $9.2 \times 0.3 \times 1$ mm^3 dimension, representing the glue, have been modeled (see Figure 4.3b).

The entire geometry of the analyzed system is shown in Figure 4.4.

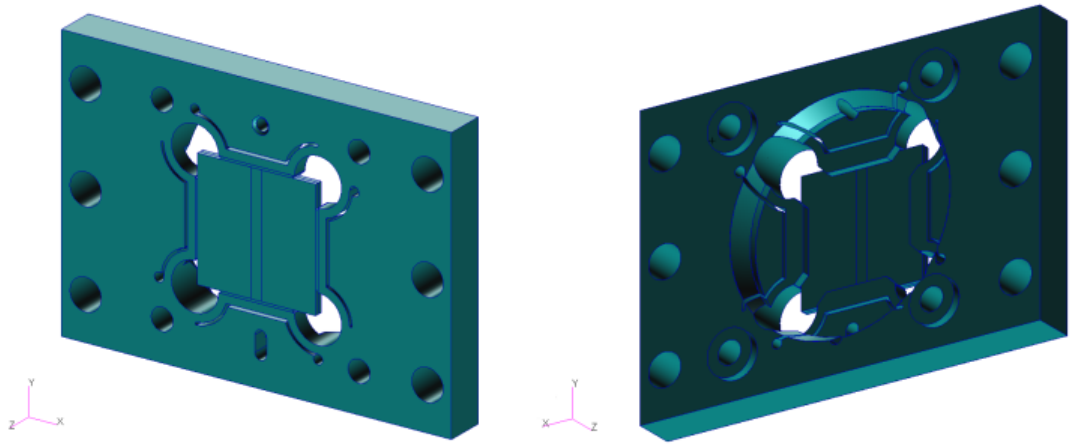


Figure 4.4: Complete geometry of the simulated model.

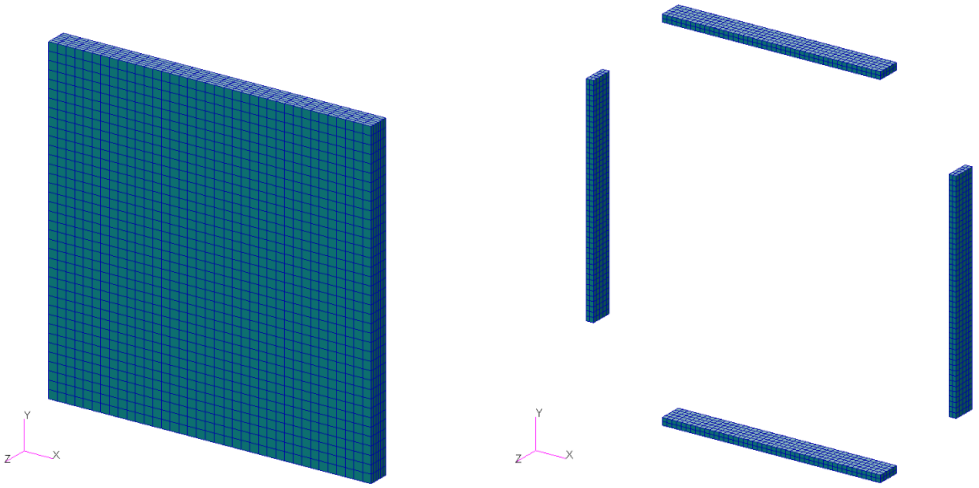
4.2.2 Meshing

To compute the finite element analysis, the system previously described has to be divided into a series of smaller elements by creating a mesh.

Since both FSA and glue have a regular shape geometry, they have been discretized by the three-dimensional hexahedral elements, which can be used only in a system with parametric coordinates. These elements consist of six faces, eight nodes and straight edges, and they offer geometric accuracy and meshing efficiency, giving the best results when compared to the other 3D finite element available in the pre-processing software.

The meshing of the filter package and the glue layers are shown in Figure 4.5; the filter strip assembly mesh has a total of 12324 nodes and 8436 elements, while the mesh of glue

consists of 3384 nodes and 1840 elements.



(a) Filter strip assembly **(b)** Glue

Figure 4.5: Mesh of the FSA and glue layers.

On the other hand, the supporting structure has a complex and irregular shape, so, the hexahedral elements cannot be used. As it can be seen in Figure 4.6, the elements used for this meshing are the three-dimensional tetrahedral, which present four faces, four nodes and straight edges. These elements are particularly suitable for complex geometries with curved surfaces but the achievable results are not as accurate as those provided by an hexahedral element discretization.

The mesh of the supporting structure has a total of 110349 nodes and 71094 elements.

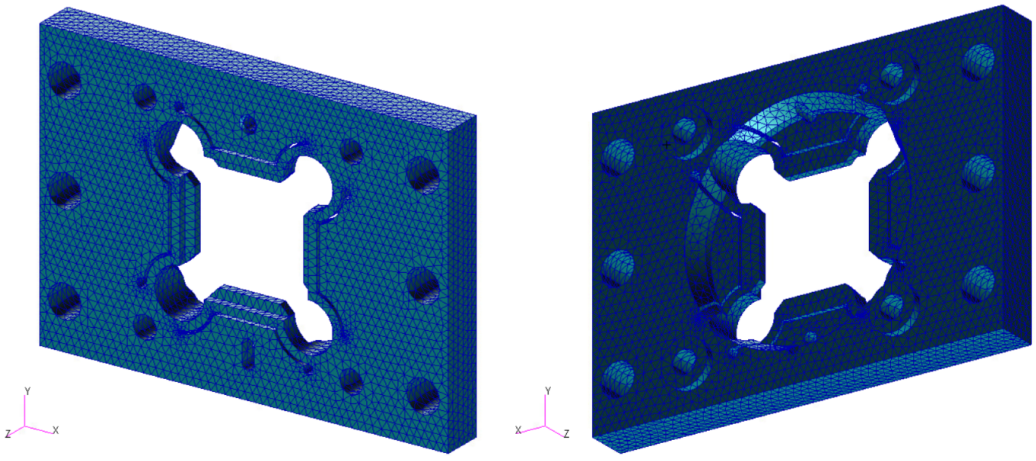


Figure 4.6: Mesh of the supporting frame.

Furthermore, the CMOS detector and its electronics have been simulated as a concentrated mass of 62 grams, positioned where the sensor's center of mass would be. This mass has been connected to the four internal through holes by means of the Rigid Body Elements Type 2 (RBE2)[2] Multi-Point Constraints (MPC) meshing object.

As it can be observed in Figure 4.7, five different RBE2 have been used: four to link all the nodes of the holes to a single node, and one to connect these four nodes to the concentrated mass. In Figure 4.8 a zoom of the rigid body connection is shown.

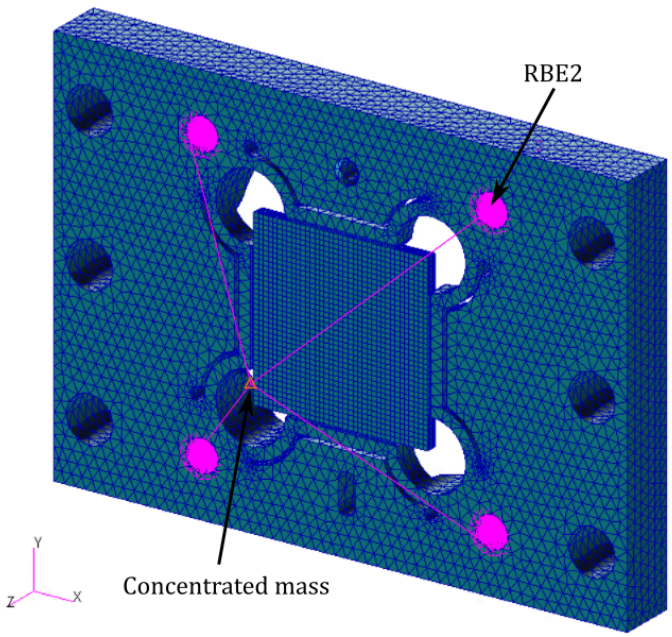


Figure 4.7: Rigid Body Elements connecting the sensor mass to the supporting structure of the FSA.

[2]The RBE2 elements are used to represent rigid body connections between nodes.

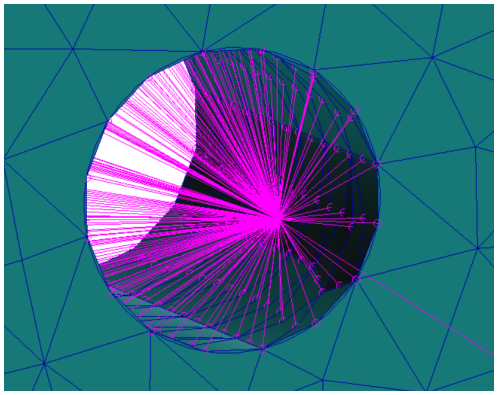


Figure 4.8: Zoom of one of the RBE2.

4.2.3 Properties

The properties of the analyzed system, in terms of material and finite element type, have been defined to describe the behaviour of the components of the model.

The material properties define the mechanical features of the used material, such as Young's modulus, Poisson's ratio, density, coefficient of thermal expansion, and so on. The used materials are aluminum for the supporting structure, fused silica for the filter strips and adhesive Ec9323-2 for the glue (manufactured by 3M [20]). For simplicity, all the used materials have been considered isotropic; the properties used in the simulation are shown in Table 4.1[3].

Material Name	Elastic Modulus [GPa]	Poisson ratio	Density [kg/m^3]	Thermal Expansion Coefficient (CTE) [K^{-}1]
Aluminum	69	0.33	2700	24×10^{-6}
Fused Silica	73	0.17	2200	0.55×10^{-6}
Ec9323-2	2.4	0.4	1040	60×10^{-6}

Table 4.1: Material properties used in the model.

Then, each material has been associated to the corresponding elements of the system, which have all been defined as 3D solid objects.

[3]Note that the values reported for the 3M scotch material (which is an epoxy resin) have been found in literature, [21], [22], [23], since they are not provided by the manufacturer.

4.2.4 Boundary Conditions

To correctly test the mechanical changes of the described model, boundary conditions have to be defined.

To simulate the six screws that connect the aluminum structure to the rest of the optical instrument, pinned supports have been used. In particular, six RBE2 have been applied to link all the nodes of the threaded holes to a single node, in which a boundary condition has been set to constrain the nodes to three translational degrees of freedom (see Figure 4.9).

Moreover, to ensure that every surface in contact with another adheres and allows the transfer of forces, moments, and displacements between them, a contact boundary condition has been inserted[4].

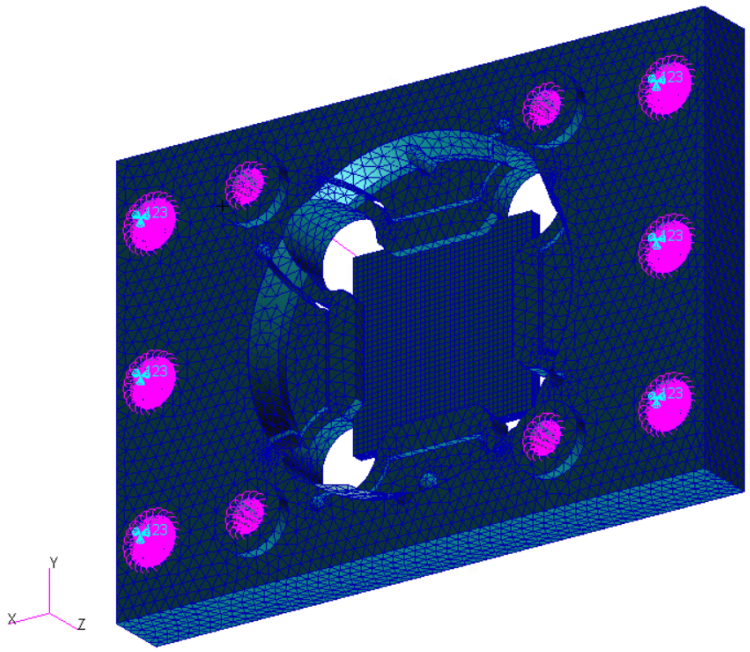


Figure 4.9: Simulation of the pinned support of the structure.

4.2.5 Loads and Analysis

For this work different physical phenomena have been simulated. In particular, the system has been subjected to two types of analysis: one to test the effect of a quasi-static acceleration

[4]The type of this contact (i.e. glued or touched) has been defined in the "Contact Table" option when selecting the analysis mode.

acting on the system and one to simulate the effect of the non-planarity of the mechanical interface between the support structure and the FSA.

All the simulations have been performed by means of a linear static structural analysis[5] with same type of contact between the components and different types of load.

The contacts between one filter and another, between filters and glue layers, and between adhesive layers and supporting structure have been considered as glued, while the contacts between filters and supporting structure have been considered as simply touched.

Since during future testing activities the FSA will be handled in different ways and the launch satellite vibrational spectrum along the different axis is yet unknown, the gravity effect has been simulated in the x, y, and z directions, both in the positive and negative verse. The maximum load required by ESA's specification for the preliminary design of the EnVisS camera is of 56 g, thus, as a first approximation, this inertial load value has been used to simulate the quasi-static acceleration effect on the FSA subsystem. To evaluate the dynamic effects of this inertial load on the subsystem, more accurate finite element models will be necessary.

Furthermore, the non-planarity of the mechanical interface has been simulated with a displacement of 5 μm in the positive z-direction, in correspondence of one of the nodes representing the screws linking the mount to the remaining part of the optical instrument. This simulation has been performed for each of the six screws to better see the overall effect of the non-planarity.

All the results obtained from these simulations are presented in Chapter 5.3.

[5]This type of simulation assumes that the response of a system subjected to an external load remains within the linear static range, hence, the deformation is proportional to the applied load.

5 Results

In Chapter 3, the optical analysis of the candidate polarizing filters for EnVisS filter strip assembly has been illustrated. In particular, the laboratory setup and experimental procedure have been described for both the tests performed with the Bentham reflectometer to study the polarizers optical properties, and those carried out by means of the Atomic Force Microscope to study the filters topography.

Moreover, the finite element analysis, performed to study the mechanical changes of the FSA whenever subjected to external loads, has been described in Chapter 4.

In the following paragraphs, all the results obtained from the aforementioned analysis have been gathered and illustrated.

5.1 Optical Properties

As previously explained, the optical properties (in terms of transmissivity and reflectivity) of all the polarizing filters candidate for the EnVisS camera have been obtained by performing several tests using the Bentham Reflectometer, available in the CNR-IFN laboratories in Padua.

Both surfaces of every sample filter have been tested, and even though the achieved results do not show significant differences in terms of optical throughput, both have been reported for the transmissivity and the reflectivity. For the Moxtek polarizing filters, the results obtained when the incident light beam hits the polarizer's surface that has the wire-grid

structure have been identified as "Surface A", while "Surface B" indicates the values obtained when the incident beam hits the other surface. For the Polarcor filter, where there is no frame to distinguish one surface with respect to the other, the first tested surface has been called "Surface A", while the opposite one has been denominated "Surface B".

In the following, the experimental data have been reported in several plots to which two dashed lines have been added to show the $\pm 2\sigma$ level of confidence of the measurements, calculated as described at the end of Section 3.1.2. Note that in some of the plots the curves have a jump in correspondence of 700 nm. This is a instrument calibration error due to the switch of the grating of the Bentham monochromator and it is not possible reducing it at instrument level. It could be possible to compensate this difference by manually changing the data, but it has been preferred to report the actual measured data.

5.1.1 Moxtek RCV8N2EC

The first analyzed filter is Moxtek RCV8N2EC. For simplicity, only the transmissivities T_p and T_s and reflectivities R_p and R_s results have been reported[1], while the plots showing the transmissivity and reflectivity for every polarization angle are reported in Appendix 8.5.

The Moxtek RCV8N2EC measured transmissivities are shown in Figures 5.1 and 5.2, while reflectivities can be seen in Figures 5.3 and 5.4. In all plots also the data provided by the manufacturer are added for comparison.

It can be observed that the measured transmissivity T_p for both surfaces perfectly fits the provider's values for almost the entire wavelength range, and that are larger than 90% in the visible range. Even the transmissivity T_s well fits the provided data and, at wavelengths larger than 500 nm, it is lower than 0.05%.

Regarding the reflectivities only the measurements done at a 10° angle of incidence (AOI) are shown in this chapter, while those achieved in the configurations with 15° and 20° AOI are shown in Appendix 8.5. Both measured reflectivities R_p and R_s with 10° AOI are slightly overestimated with respect to provider's data. In particular, this difference is larger for the reflectivity R_s where the Moxtek data are within the error range of measurement only in the infrared portion of the spectrum. Moreover, in EnVisS operational bandwidth (i.e., 550-800 nm) the measured R_p is lower than 6%, while R_s is between 67% and 77%.

[1] Remember that T_p and R_p are the optical properties measured with the sample polarization axis aligned with the one of the polarizer mounted on the motorized rotation stage, while T_s and R_s are those obtained with the polarizing axes at a 90° relative angle.

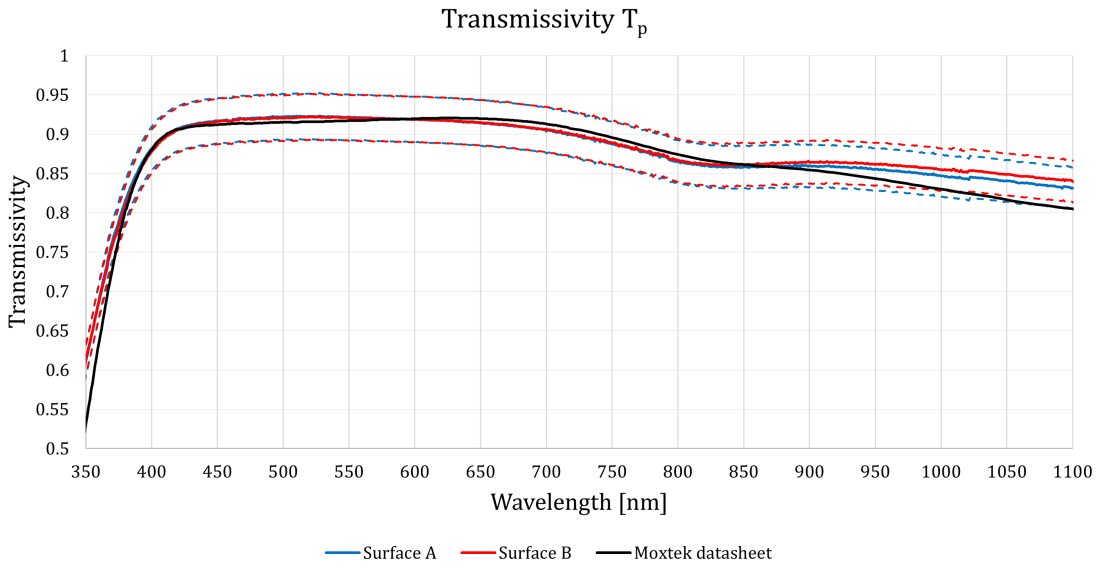


Figure 5.1: Transmissivity T_p of Moxtek RCV8N2EC polarizer in the wavelength range 350-1100 nm. Dashed lines give the confidence range of the measurements.

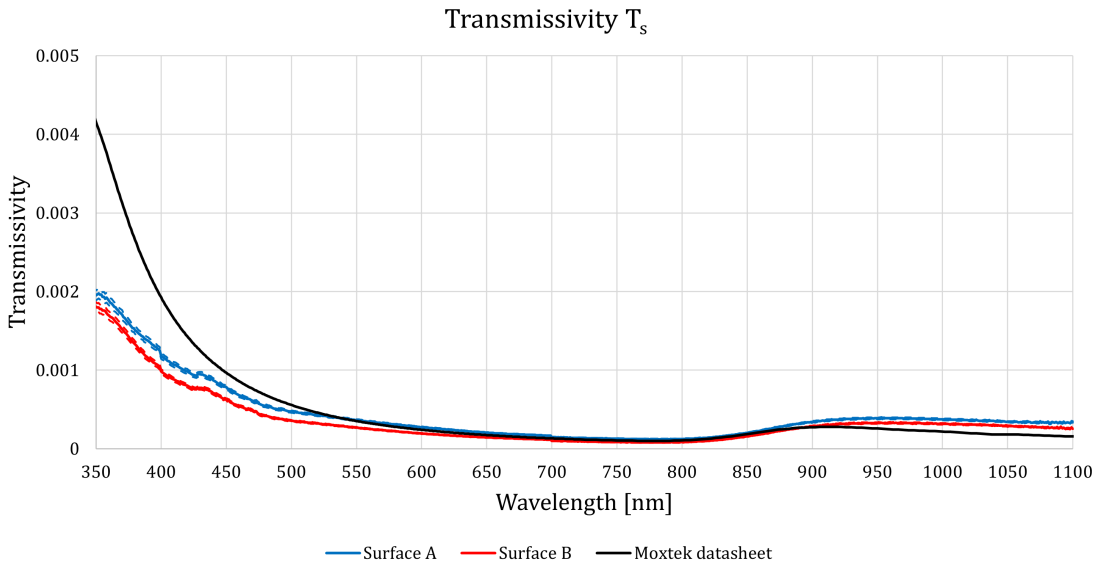


Figure 5.2: Transmissivity T_s of Moxtek RCV8N2EC polarizer in the wavelength range 350-1100 nm. Dashed lines give the confidence range of the measurements.

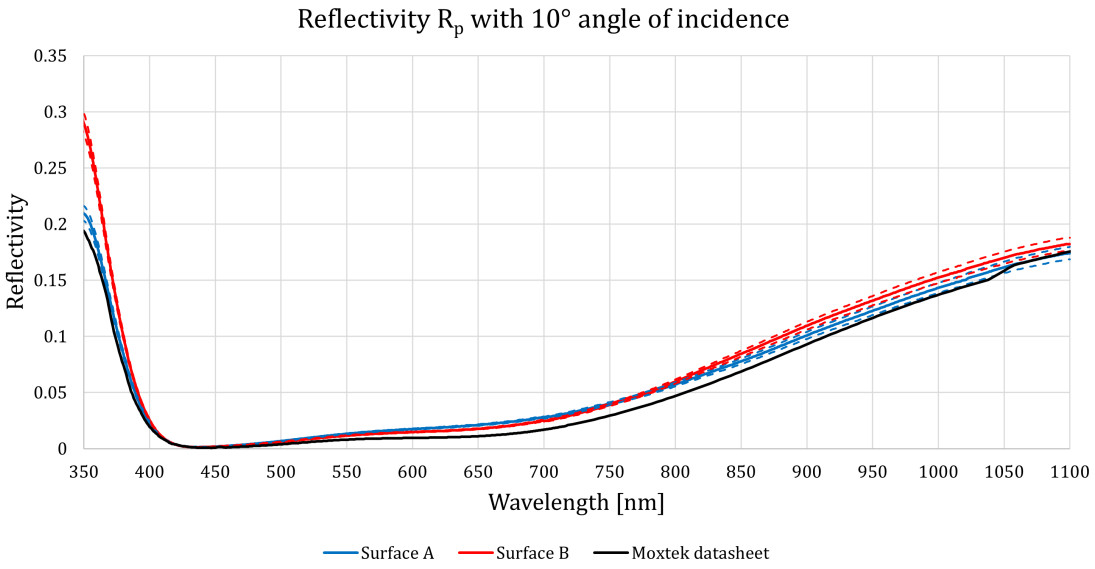


Figure 5.3: Reflectivity R_p of Moxtek RCV8N2EC polarizer with a 10° AOI in the wavelength range 350-1100 nm. Dashed lines give the confidence range of the measurements.

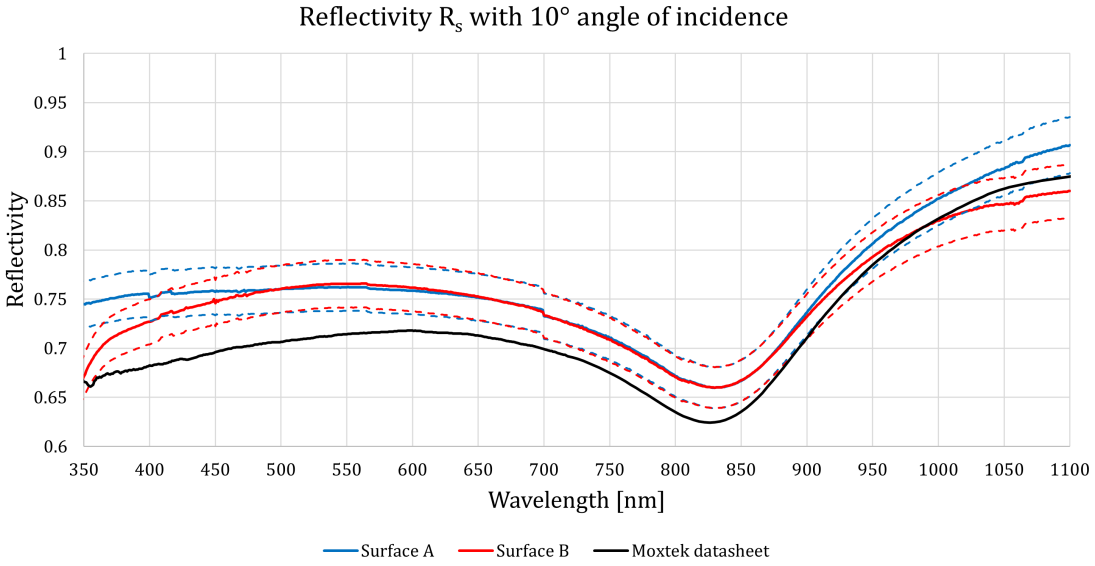


Figure 5.4: Reflectivity R_s of Moxtek RCV8N2EC polarizer with a 10° AOI in the wavelength range 350-1100 nm. Dashed lines give the confidence range of the measurements.

Since no appreciable difference between the results obtained by testing the two surfaces of the polarizer has been observed, the following plots indicate only the measurement data

collected when the incident beam hits Surface B.

The dynamic range of the CMOS sensor is 10 bits, thus, the contrast ratio (CR = T_p/T_s) of the filter has to be at least 1024 to use the whole dynamic range of the detector. In Figure 5.5 the CR of the Moxtek RCV8N2EC polarizer and its comparison with the provider data is shown. It can be observed that the measured data and those provided by the manufacturer follow the same trend and, in EnVisS operational wavelength, the CR is larger than 1024, proving that the sensor will detect only the T_p transmissivity component. The difference between the two curves is probably due to the difference in the measurement of the transmissivity T_s, since the detected transmitted signal is very low and is difficult to measure it with enough precision.

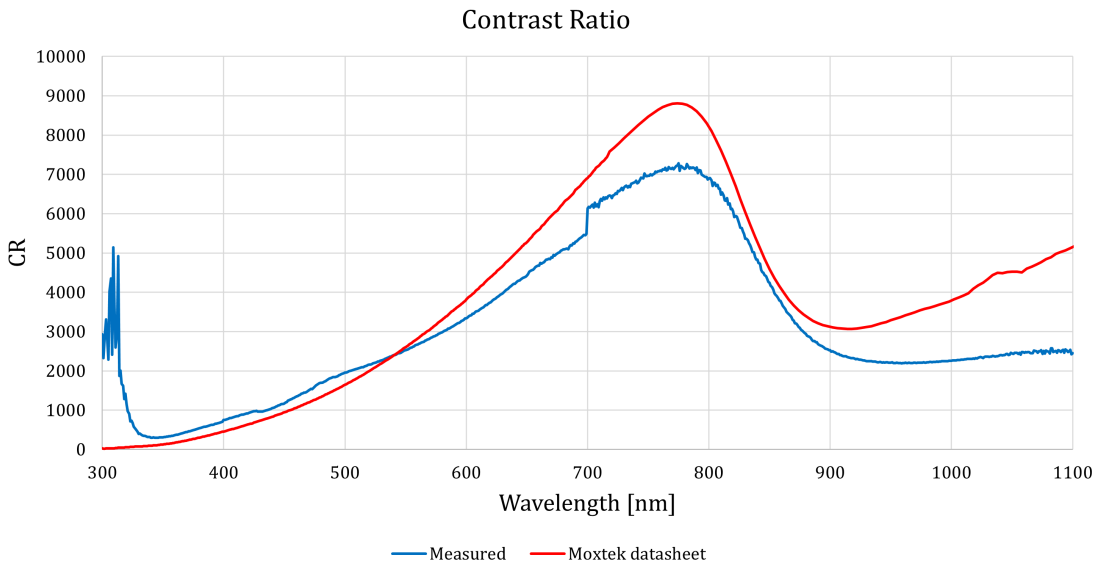


Figure 5.5: Contrast ratio of Moxtek RCV8N2EC polarizer.

As illustrated in Chapter 3, the transmissivity and reflectivity have been sampled by rotating the tested filter in the rotator stage, thus changing the orientation of its polarization axis from 0° to 180° with a step of 15°, and allowing the creation of the Malus' curves, which are shown in Figures 5.6 and 5.7.

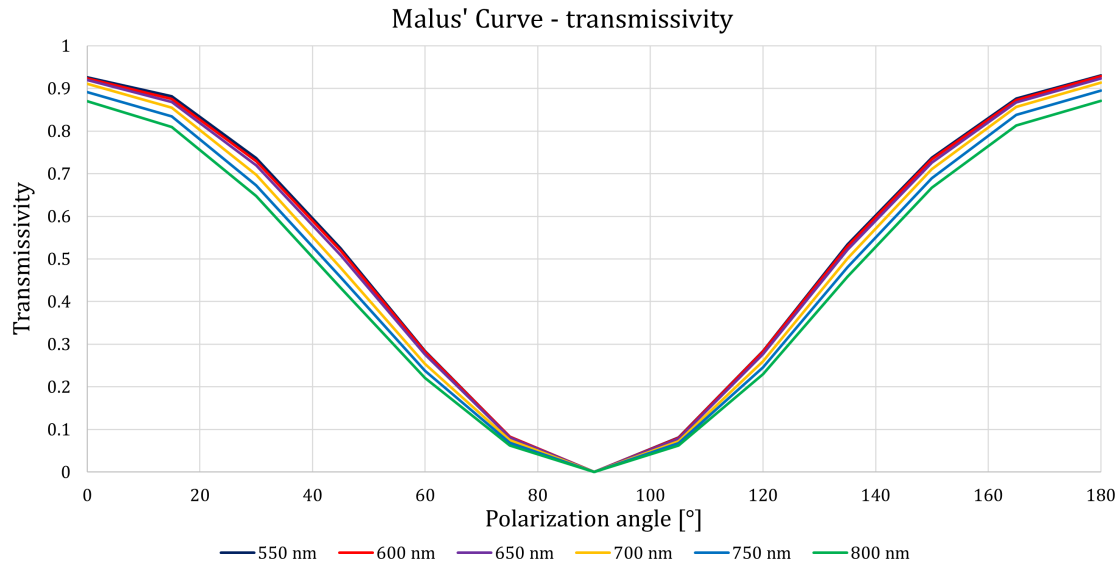


Figure 5.6: Malus' curve of Moxtek RCV8N2EC polarizer transmissivity for specific wavelengths.

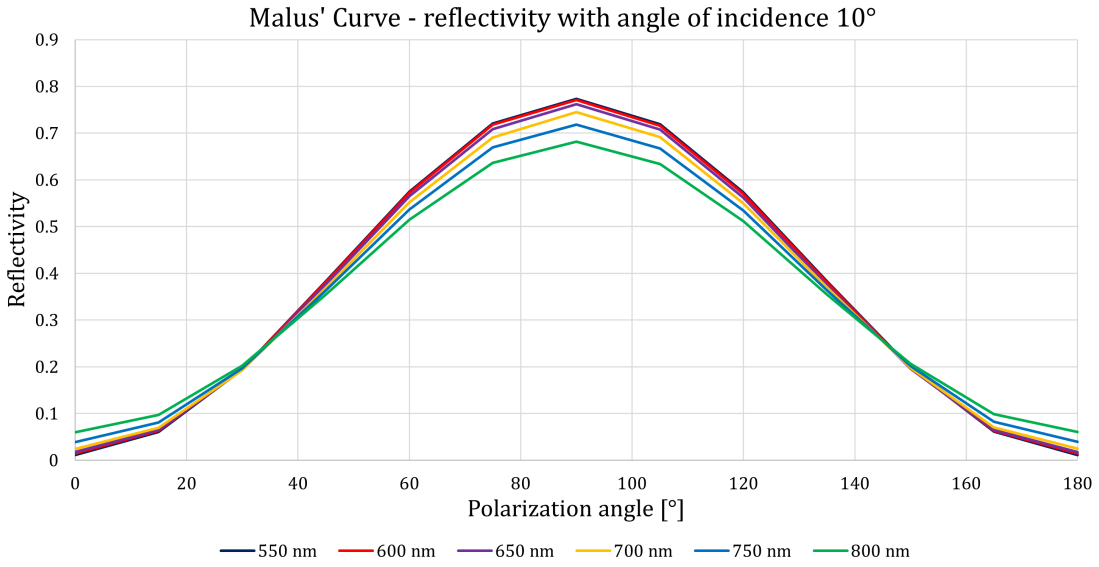


Figure 5.7: Malus' curve of Moxtek RCV8N2EC polarizer reflectivity for specific wavelengths.

It can be observed that the curves fit the $\cos^2\theta$ curve, where θ is the polarization angle, and are symmetric with respect to the 90° polarization angle, thus proving the symmetric behaviour of the polarizer.

As already mentioned, the reflectivity has been measured also for the incident angles of 15° and 20°. The manufacturer, though, provided the reflectivity values for incident angles of 10°, 20°, 25°, 35°, 45°, 55° and 65°; hence, an interpolation of the Moxtek data for all the provided incident angles has been performed to estimate the filter's reflectivity at 15° and make a comparison between all the data collected with different AOI.

Lastly, Figures 5.8 and 5.9 show how reflectivities R_p and R_s change as function of the incident angle. In particular, both the values from datasheet and the measured data have been reported for three specific wavelengths in EnVisS operational bandwidth (i.e., 550 nm, 675 nm, 800 nm). As it can be observed, the obtained results and the data provided by the manufacturer are rather different. The reason for this behaviour is yet unknown but is under discussion with the provider.

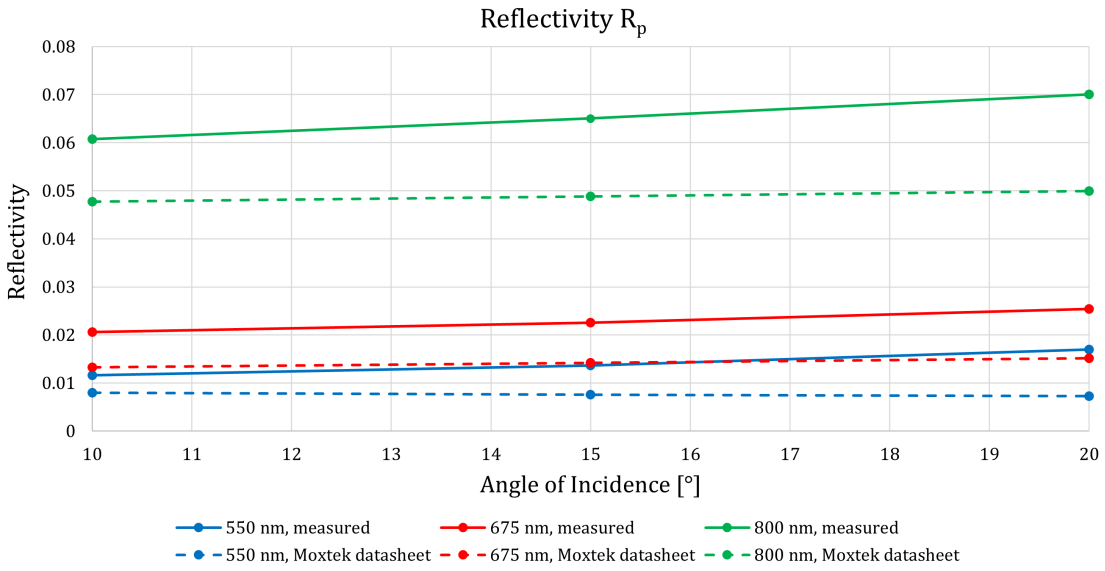


Figure 5.8: Comparison between measured and datasheet values of the reflectivity R_p of Moxtek RCV8N2EC polarizer as function of the incident angle for specific wavelengths.

5.1.2 Moxtek UBB01A

The same methodology of data processing used for the previous filter has been adopted for the Moxtek UBB01A polarizer[2].

[2]As for Moxtek RCV8N2EC, in this chapter have been reported only the results in terms of T_p, T_s, R_p and R_s, while plots representing the transmissivity and reflectivity for every polarization angle are reported in Appendix 8.5.

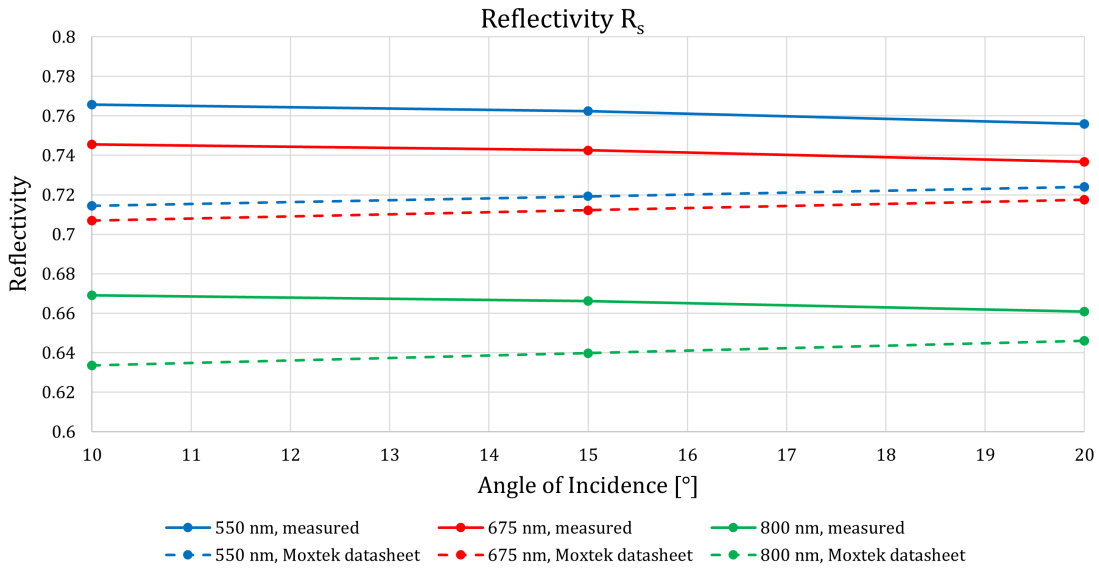


Figure 5.9: Comparison between measured and datasheet values of the reflectivity R_s of Moxtek RCV8N2EC polarizer as function of the incident angle for specific wavelengths.

The Moxtek UBB01A measured transmissivities T_p and T_s are shown in Figures 5.10 and 5.11, where the curve representing the data provided by Moxtek and the dashed lines giving the level of confidence range of the measurements have been added.

From the plots, it is clear that both transmissivities overestimate the values provided by the manufacturer, and, as for Moxtek RCV8N2EC, the comparison between the results achieved from the measurement on the two surfaces of the polarizer does not show significant differences.

Moreover, it can be observed that T_p is larger than 80% over the entire considered wavelength range, exceeding 85% in the EnVisS camera operational bandwidth; while T_s is lower than 0.05% for wavelength larger than 500 nm.

The reflectivities R_p and R_s measured with an incident angle of 10° are shown in Figures 5.12 and 5.13, in which also their respective $\pm 2\sigma$ error range and the data provided by Moxtek for these optical properties have been reported.

As for the transmissivity, no appreciable difference between the results of the two sides of the polarizer can be seen, except for the R_s plot, where the curves are slightly different but always inside the error ranges.

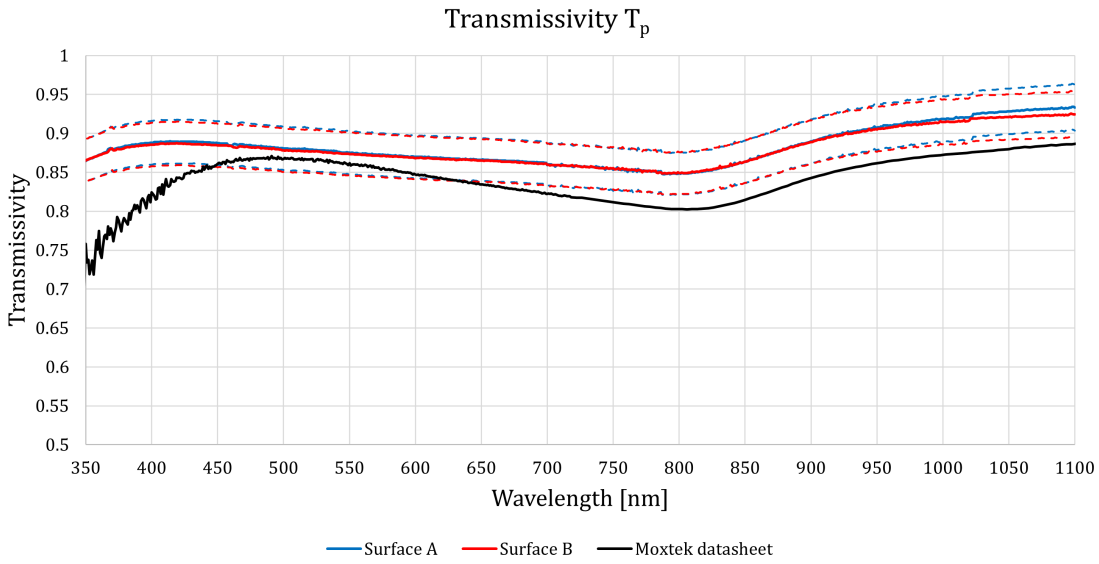


Figure 5.10: Transmissivity T_p of Moxtek UBB01A polarizer in the wavelength range 350-1100 nm. Dashed lines give the confidence range of the measurements.

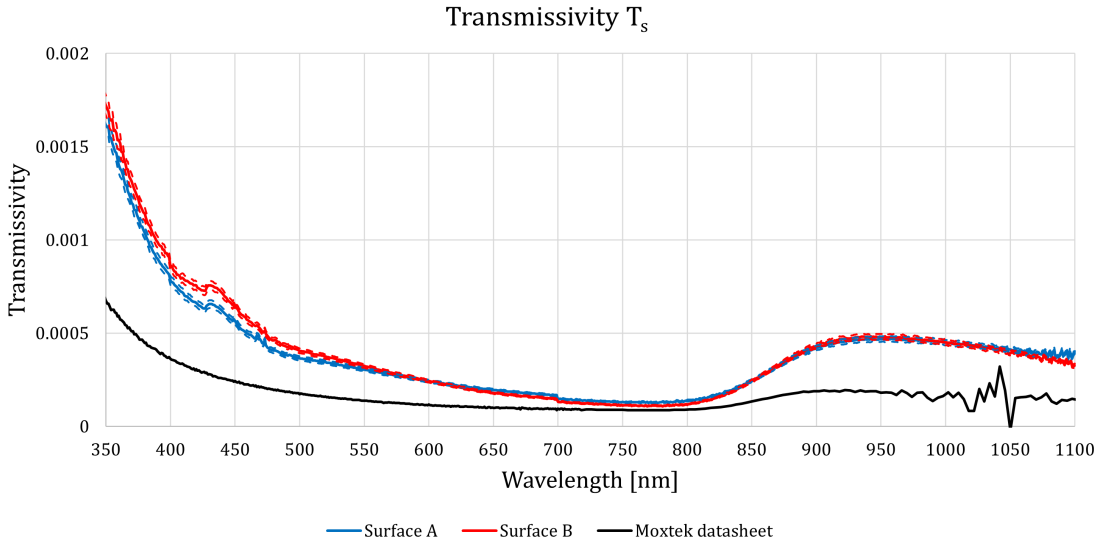


Figure 5.11: Transmissivity T_s of Moxtek UBB01A polarizer in the wavelength range 350-1100 nm. Dashed lines give the confidence range of the measurements.

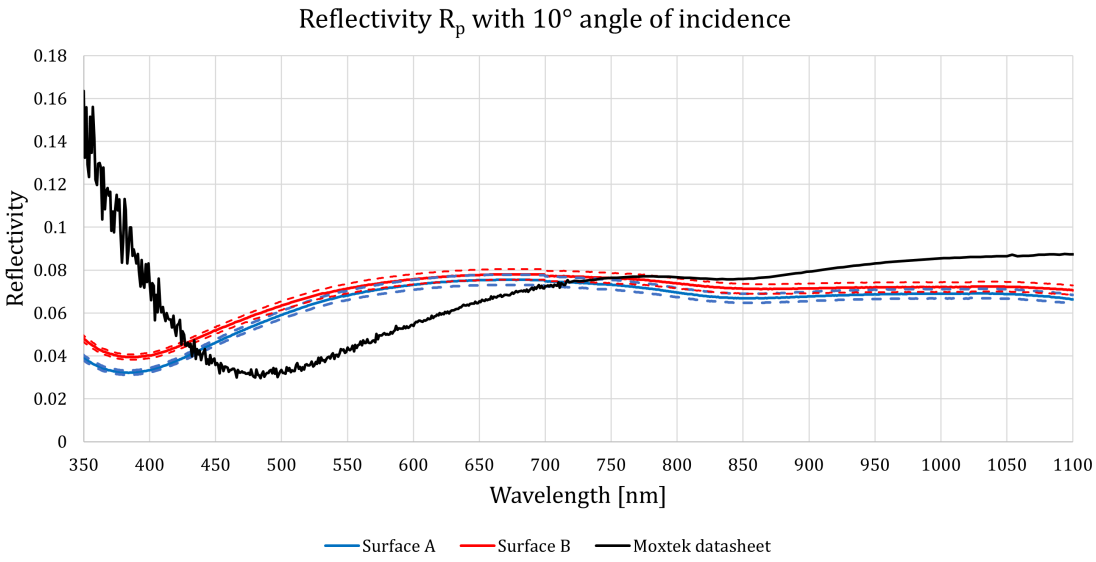


Figure 5.12: Reflectivity R_p of Moxtek UBB01A polarizer with a 10° AOI in the wavelength range 350-1100 nm. Dashed lines give the confidence range of the measurements.

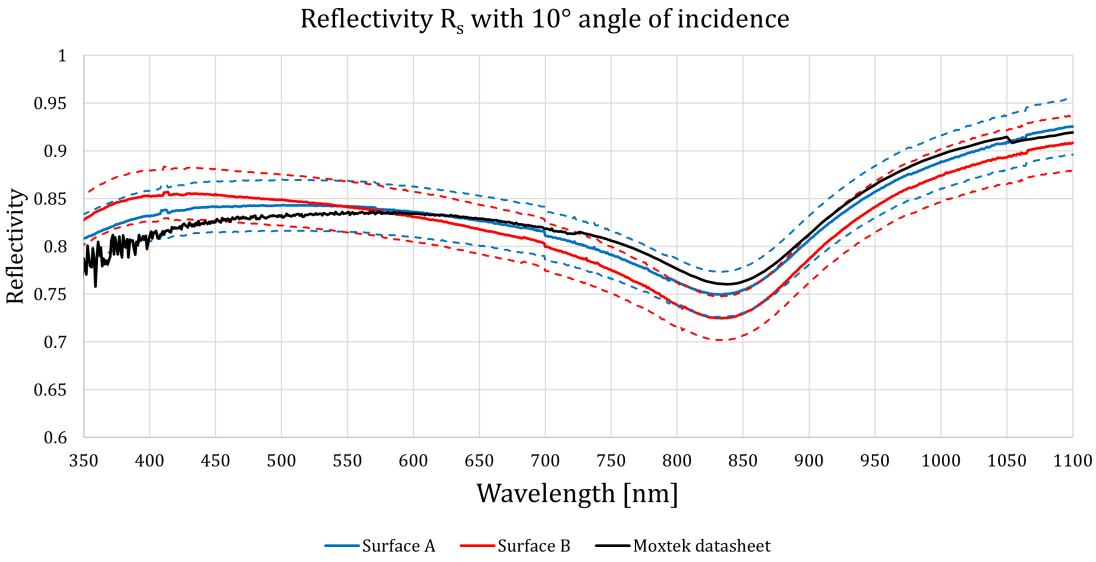


Figure 5.13: Reflectivity R_s of Moxtek UBB01A polarizer with a 10° AOI in the wavelength range 350-1100 nm. Dashed lines give the confidence range of the measurements.

It can be observed that the measured reflectivity R_p does not fit well the values from Moxtek datasheet, while the data provided for reflectivity R_s is enclosed in the level of confidence of the measured results.

Furthermore, R_p is less than 8% in the whole wavelength range, and R_s varies from 70% to 85% in the range 550-800 nm.

In Figure 5.14 the contrast ratio of the Moxtek UBB01A polarizer and its comparison with the provider data is shown. As for the previous analyzed filter, the measured data and those provided by the manufacturer follow approximately the same trend and, in EnVisS operational wavelength, the CR is larger than 1024, proving that the sensor will detect only the T_p transmissivity component. Also in this case the reason behind the different values of the two curves is probably due to the difference in the measurement of the transmissivity T_s, as previously explained.

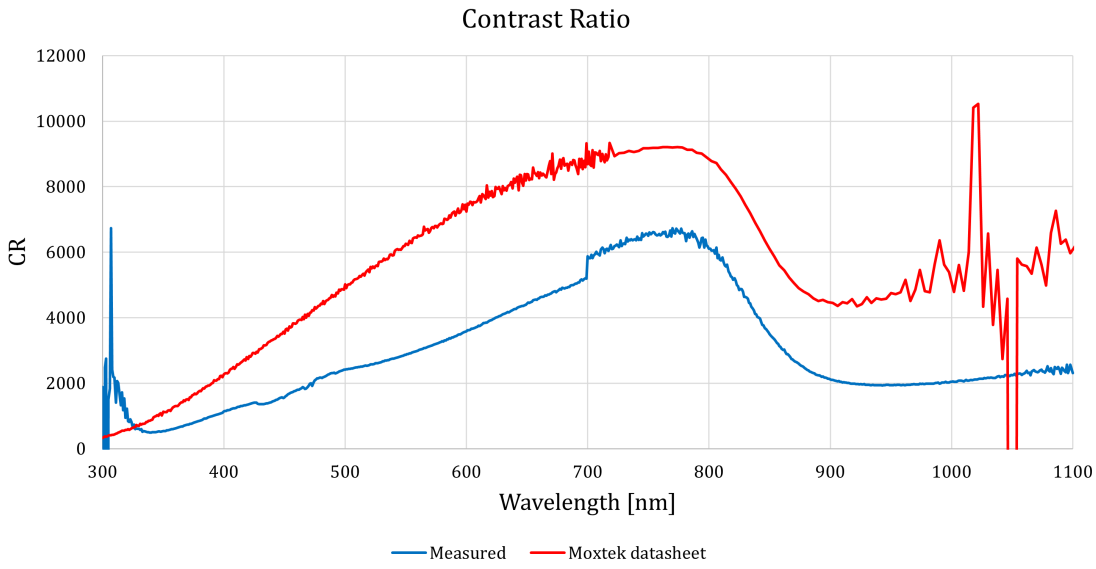


Figure 5.14: Contrast ratio of Moxtek UBB01A polarizer.

As it has been done for Moxtek RCV8N2EC, the following graphs will indicate only the measurement data collected when the incident beam hits Surface B, since no appreciable difference is shown between the two sides of the UBB01A filter.

The Malus' curves for both transmissivity and reflectivity have been computed by rotating the tested filter from 0° to 180° with a step of 15° and the results are shown in Figures 5.15 and 5.16. As for Moxtek RCV8N2EC, the curves fit the $\cos^2\theta$ curve, where θ is the polarization angle, and are symmetric with respect to the 90° polarization angle, thus proving the symmetric behaviour of the polarizer.

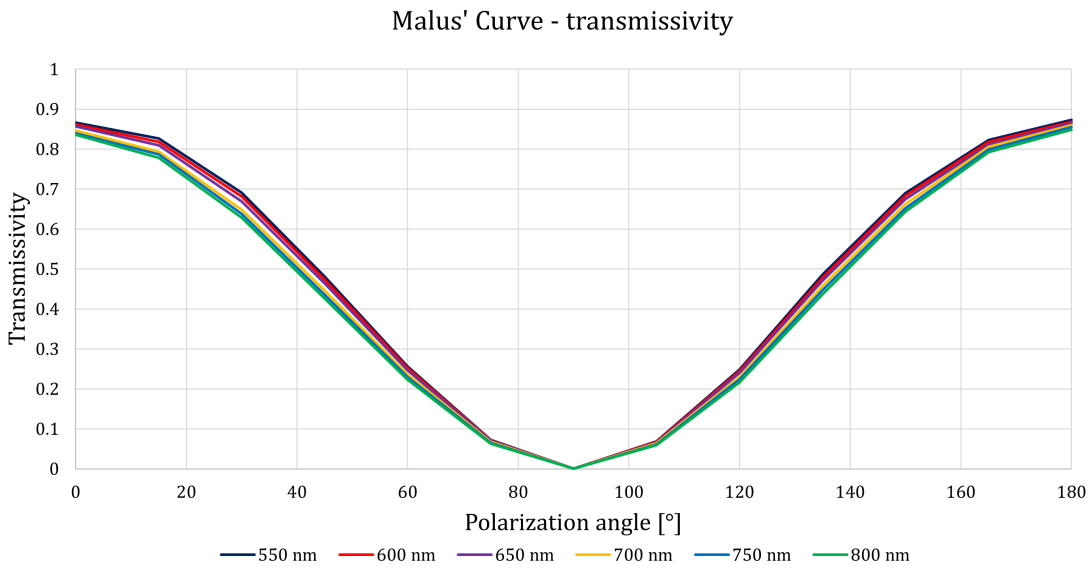


Figure 5.15: Malus' curve of Moxtek UBB01A polarizer transmissivity for specific wavelengths.

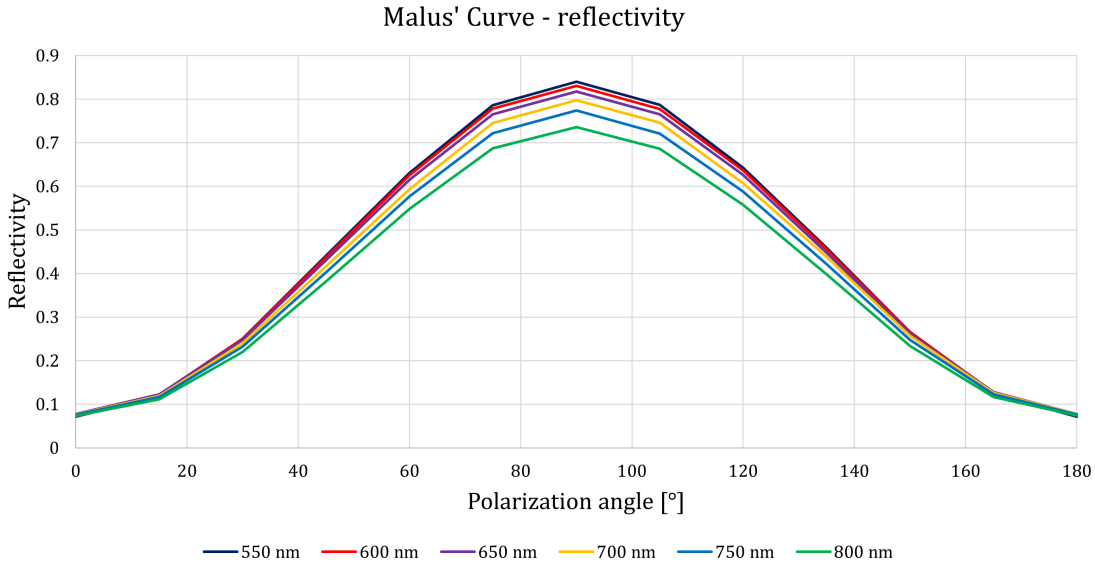


Figure 5.16: Malus' curve of Moxtek UBB01A polarizer reflectivity for specific wavelengths.

Also in this case, the reflectivity has been measured for the AOIs equal to 10°, 15°, 20°. For UBB01A, the manufacturer provided the reflectivity values for the incident angles 10°, 20°, 25°; so, in order to compare the collected data with 15° AOI, an interpolation of the Moxtek values has been performed.

Finally, in Figures 5.17 and 5.18, the dependence of the reflectivities on the incident angle is shown. Both the values from datasheet and the measured data have been reported for three specific wavelengths in EnVisS operational bandwidth (i.e., 550 nm, 675 nm, 800 nm).

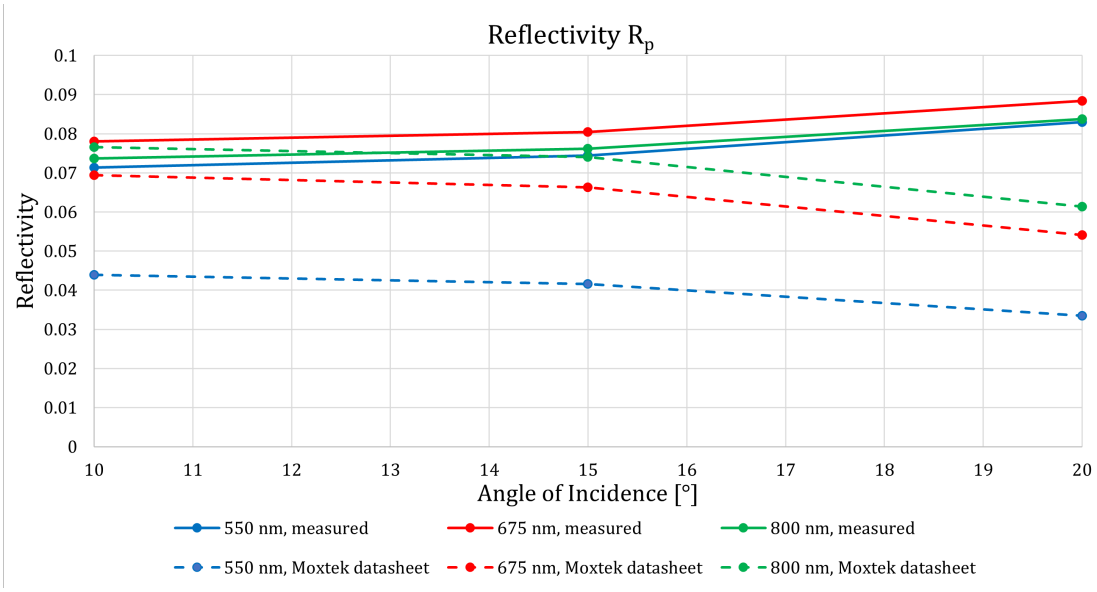


Figure 5.17: Comparison between measured and datasheet values of the reflectivity R_p of Moxtek UBB01A polarizer as function of the incident angle for specific wavelengths.

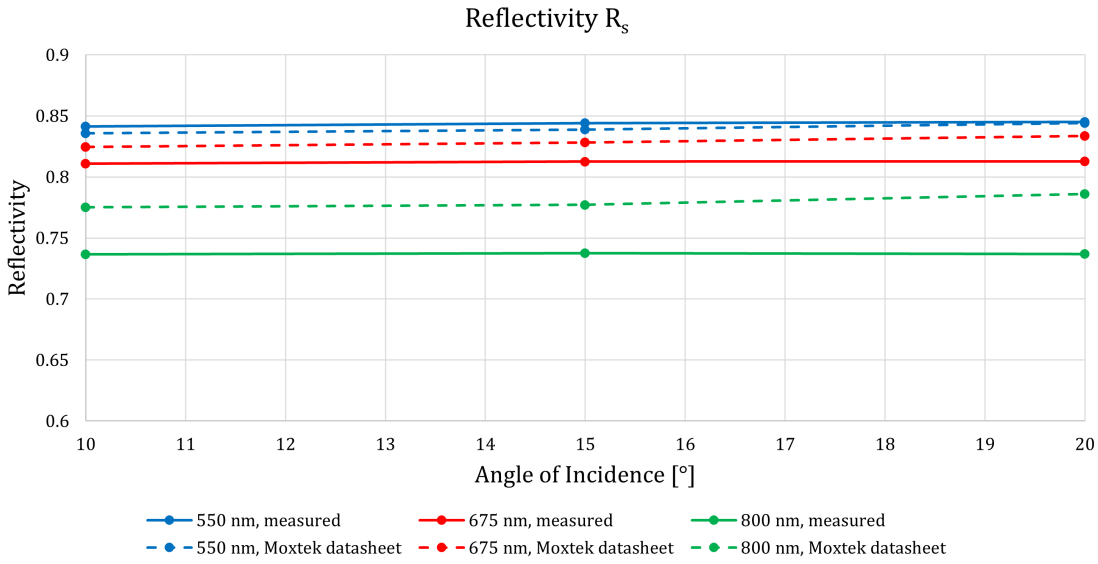


Figure 5.18: Comparison between measured and datasheet values of the reflectivity R_s of Moxtek UBB01A polarizer as function of the incident angle for specific wavelengths.

As it can be observed, the obtained results and the data provided by manufacturer are rather different. In particular, the slope of the measured R_p curves is in contrast with that of Moxtek data, since their reflectivity values decrease with the increase of the incident angle. Usually, the glass reflectivity increases with the increase of the AOI, so the measured data are more in line with what was expected. The reason for the behaviour of the data given by Moxtek is yet unknown but is under discussion with the provider.

5.1.3 Polarcor Wide Band

The last tested polarizing filter is Polarcor Wide Band Polarizer.

The Polarcor Wide Band Polarizer measured transmissivities T_p and T_s are reported in Figures 5.19 and 5.20. The filter manufacturer has not provided any datasheet, so comparisons have been performed only between the two tested surfaces. To appreciate the results achieved for the transmissivity T_s, in Figure 5.21 a zoomed view of the values in the wavelength range 500−1100 nm has been shown.

Polarcor's transmissivity is strongly influenced by the considered wavelength and starts to correctly work for wavelengths longer than 500 nm. Moreover, the curve do not show a rapid rise, reaching the 80% transmissivity T_p above 650 nm and extending over 90% above 750 nm. Consequently, it can already be observed that the behaviour of this polarizing filter does not fit EnVisS purposes. It can also be pointed out thay transmissivity T_s is less than 0.01% in most of EnVisS operational bandwidth.

As explained in Section 2.2.2, Polarcor Wide Band polarizer is based on selective absorption due to its material anisotropy, and so the reflection signal is independent of the polarization angle of the reflective sample.

For this reason, the behavior of this filter's reflectivity is very different from what resulted for the Moxtek polarizers, as it can be seen in Figure 5.22, where the reflectivity measured at 10° AOI and polarization angle of 0°, 45° and 90° have been reported.

Note that since no appreciable difference between the transmissivity results obtained by testing the two surfaces of the polarizer comes out, the following plots represents the values achieved when the incident beam hit the Surface B.

In Figure 5.23 the contrast ratio of the Polarcor Wide Band polarizer is shown. Since no data have been provided by the manufacturer, the only thing that can be observed is that, due to the extremely low values of the transmissivity T_s, the CR results are very high, reaching approximately 16000 between 700 and 800 nm.

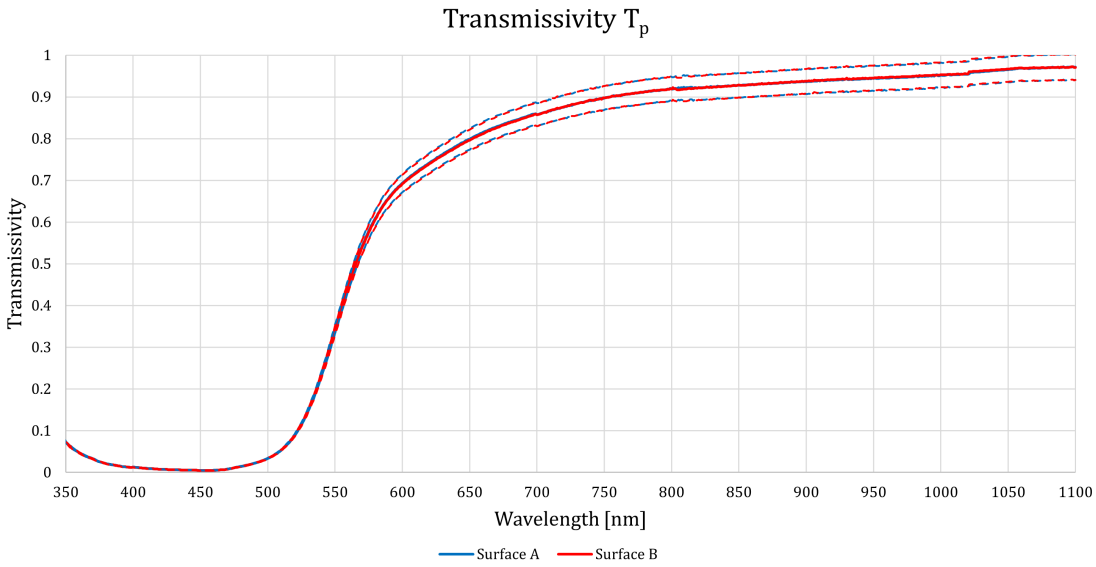


Figure 5.19: Transmissivity T_p of Polarcor Wide Band polarizer in the wavelength range 350-1100 nm. Dashed lines give the confidence range of the measurements.

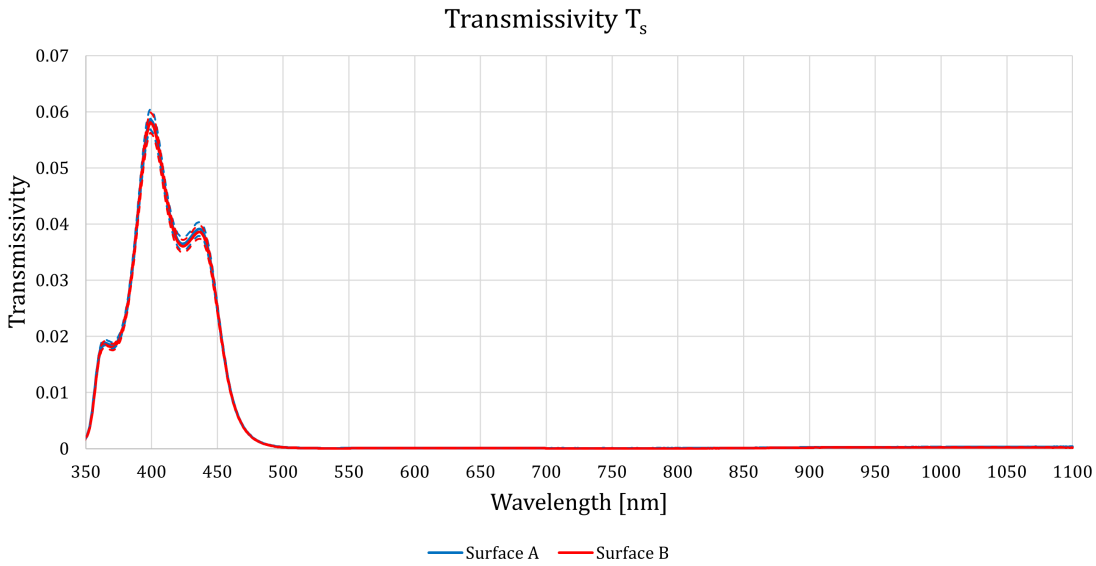


Figure 5.20: Transmissivity T_s of Polarcor Wide Band polarizer in the wavelength range 350-1100 nm. Dashed lines give the confidence range of the measurements.

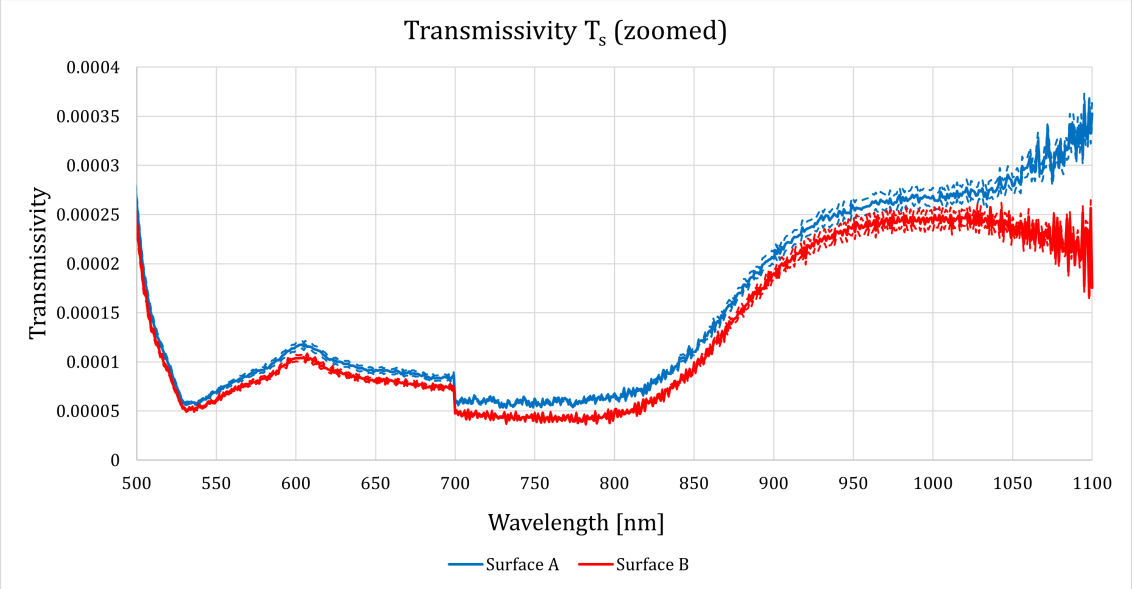


Figure 5.21: Zoom of the transmissivity T_s of Polarcor Wide Band polarizer in the wavelength range 500-1100 nm. Dashed lines give the confidence range of the measurements.

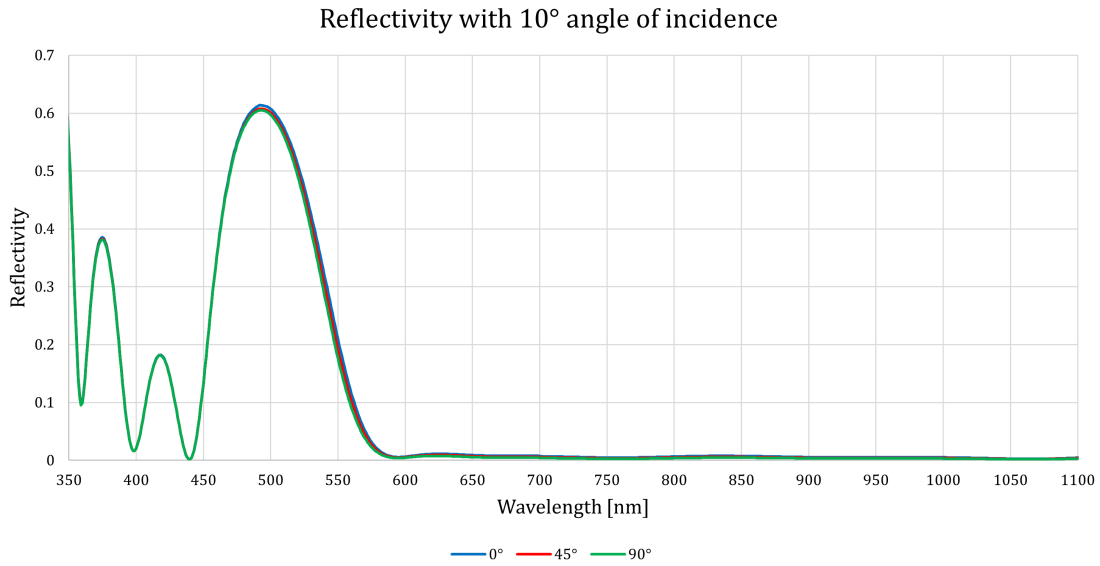


Figure 5.22: Reflectivity of Polarcor Wide Band polarizer with an AOI of 10° at 0°, 45° and 90° polarization angle, in the wavelength range 350-1100 nm.

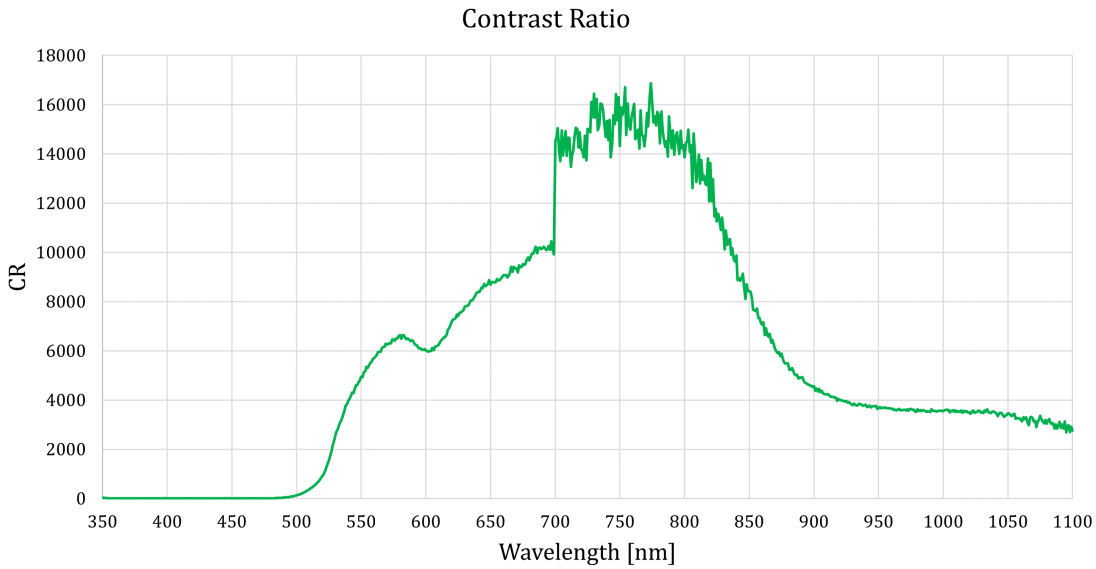


Figure 5.23: Contrast ratio of Polarcor Wide Band polarizer.

Furthermore, in Figure 5.24 a comparison between the reflectivity curves for different incident angles has been shown and it can be seen that the results present only small differences.

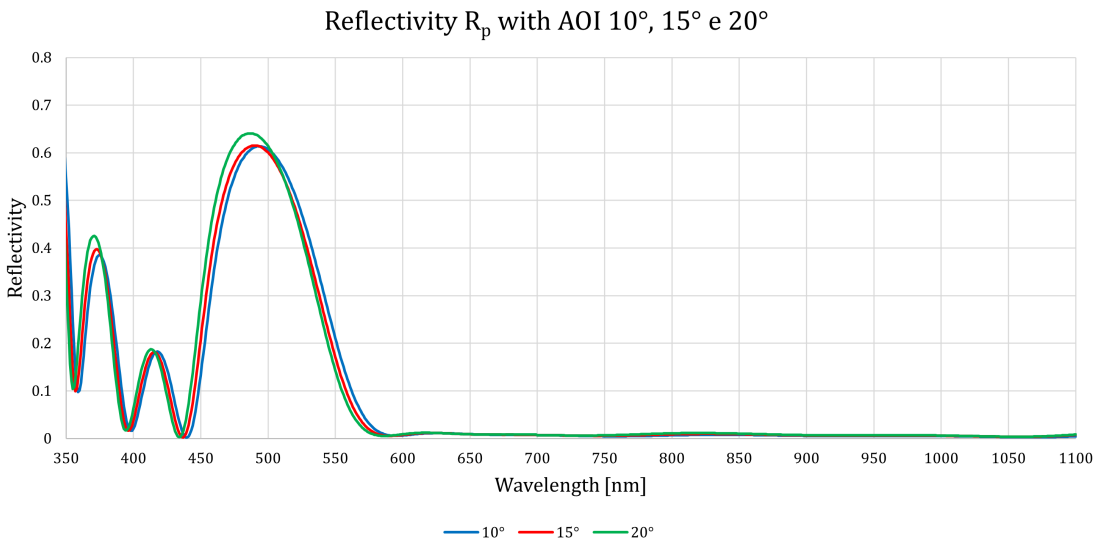


Figure 5.24: Reflectivity of Polarcor Wide Band polarizer considering an AOI of 10°, 15° and 20°, in the wavelength range 350-1100 nm.

Finally, Malus' curve for transmissivity is shown in Figure 5.25 and, as for the Moxtek

polarizers, the symmetric behaviour of the filter is proved and the curves fit the $\cos^2\theta$ trend.

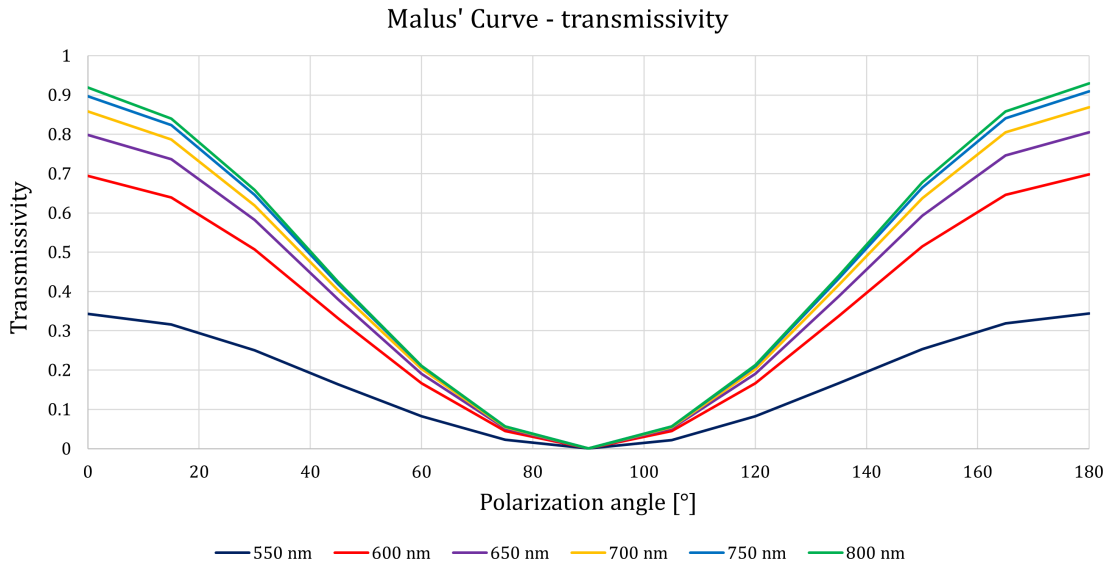


Figure 5.25: Malus' curve of Polarcor Wide Band polarizer transmissivity for specific wavelengths.

5.1.4 Comparison

In this paragraph, comparisons between the same properties among Moxtek RCV8N2EC and UBB01A, and Polarcor Wide Band polarizers are shown.

In addition to the optical properties T_p, T_s, R_p and R_s, curves for absorption A_p and A_s and contrast ratio CR have been reported. As for the previous plots, the dashed lines represent the confidence range of the measurements.

In Figures 5.26 and 5.27 the transmissivities T_p and T_s for the three different characterized filters are shown. It can be seen that RCV8N2EC has the highest transmissivity T_p up to about 740 nm, while at longer wavelengths Polarcor polarizer's T_p is larger. Moxtek UBB01A's transmissivity T_p is lower than the RCV8N2EC one up to 830 nm. On the other hand, the Wide Band transmissivity T_s is lower than the Moxtek one for wavelengths longer than 500 nm, while Moxtek polarizing filters show approximately the same values.

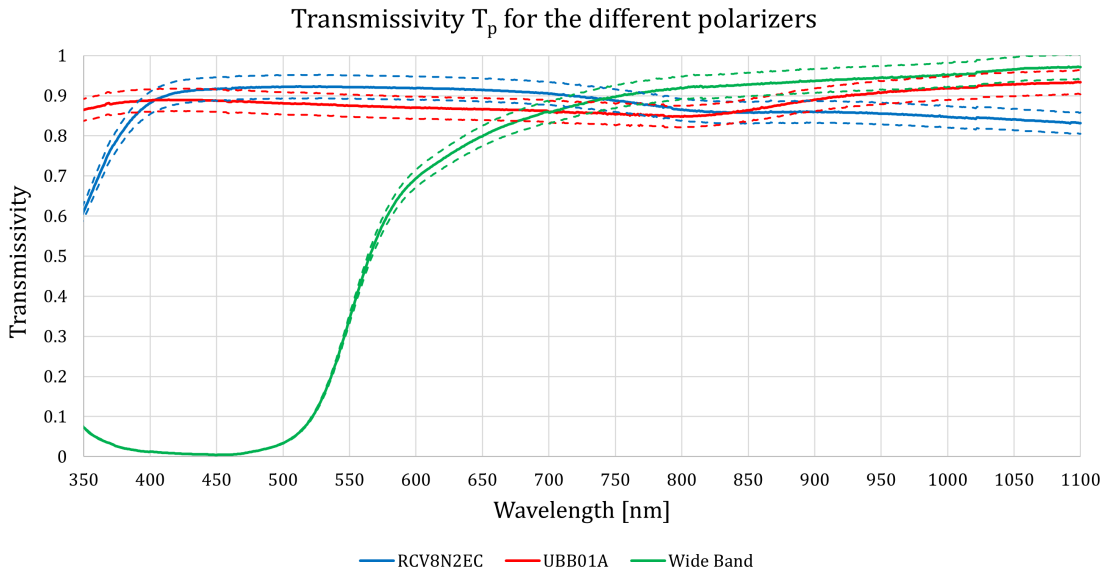


Figure 5.26: Transmissivity T_p of Moxtek RCV8N2EC, Moxtek UBB01A, Polarcor Wide Band polarizers, in the wavelength range 350-1100 nm. Dashed lines give the confidence range of the measurements.

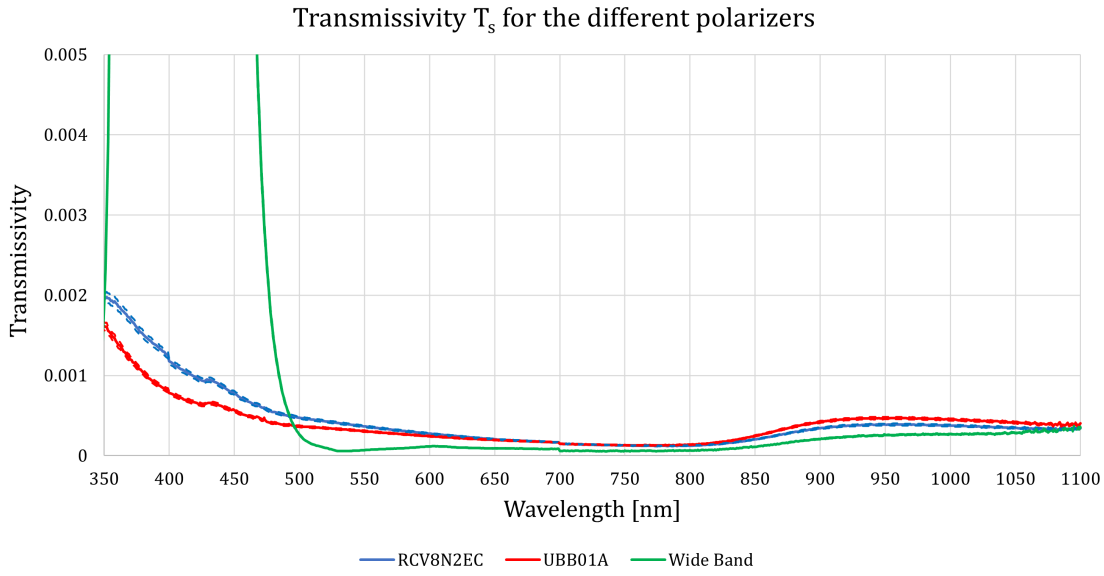


Figure 5.27: Transmissivity T_s of Moxtek RCV8N2EC, Moxtek UBB01A, Polarcor Wide Band polarizers, in the wavelength range 350-1100 nm. Dashed lines give the confidence range of the measurements.

From these two figures, it can be already pointed out that Polarcor Wide Band polarizer has overall the highest transmissivity T_p and the lowest transmissivity T_s, that gives the highest

contrast ratio (as shown in Figure 5.32), which is the optimal feature of a polarizing filter. Unfortunately, the Wide Band transmissivity T_p does not satisfy EnVisS requirements in the entire operational wavelength range, since it is lower than 80% for wavelengths shorter than 650 nm.

In Figures 5.28 and 5.29 the reflectivities R_p and R_s are reported. Moxtek UBB01A reflectivity R_p shows a behavior rather independent of the wavelength (more than RCV8N2EC) and is higher than that of RCV8N2EC up to 820 nm. Polarcor Wide Band reflectivity R_p deeply changes around 600 nm: up to 600 nm intense peaks take place, while over this wavelength the R_p value is lower than 1.2%.

Since the Polarcor filter reflectivity does not depend on the polarization angle, no differences arise from considering R_p or R_s. The shape of the reflectivity R_s curve is similar for the Moxtek polarizers. The main difference is that UBB01A reflects around 8% more than RCV8N2EC in the range 550 – 800 nm.

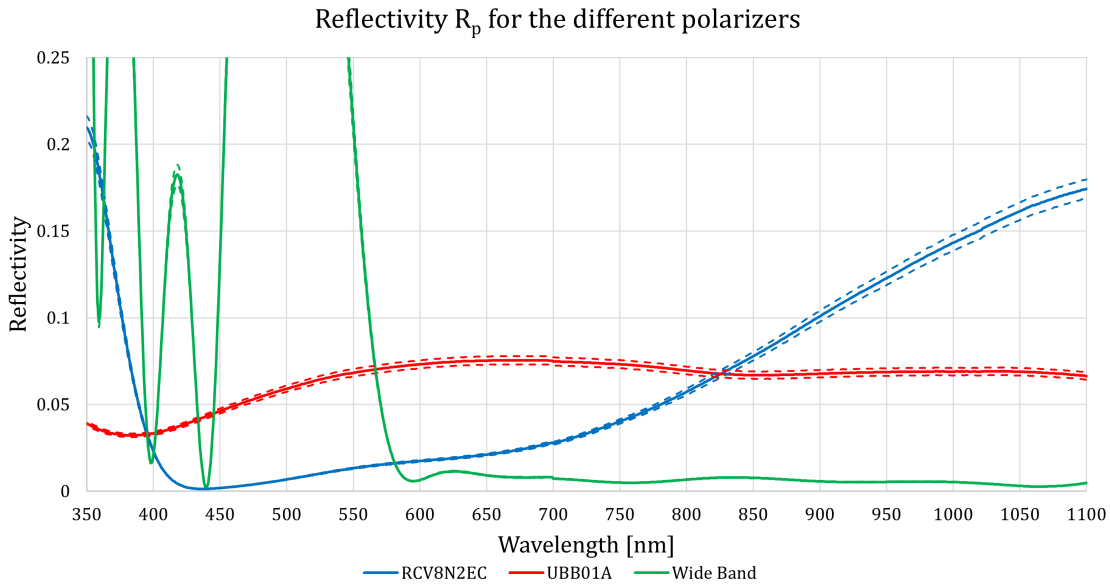


Figure 5.28: Reflectivity R_p of Moxtek RCV8N2EC, Moxtek UBB01A, Polarcor Wide Band polarizers with a 10° AOI, in the wavelength range 350-1100 nm. Dashed lines give the confidence range of the measurements.

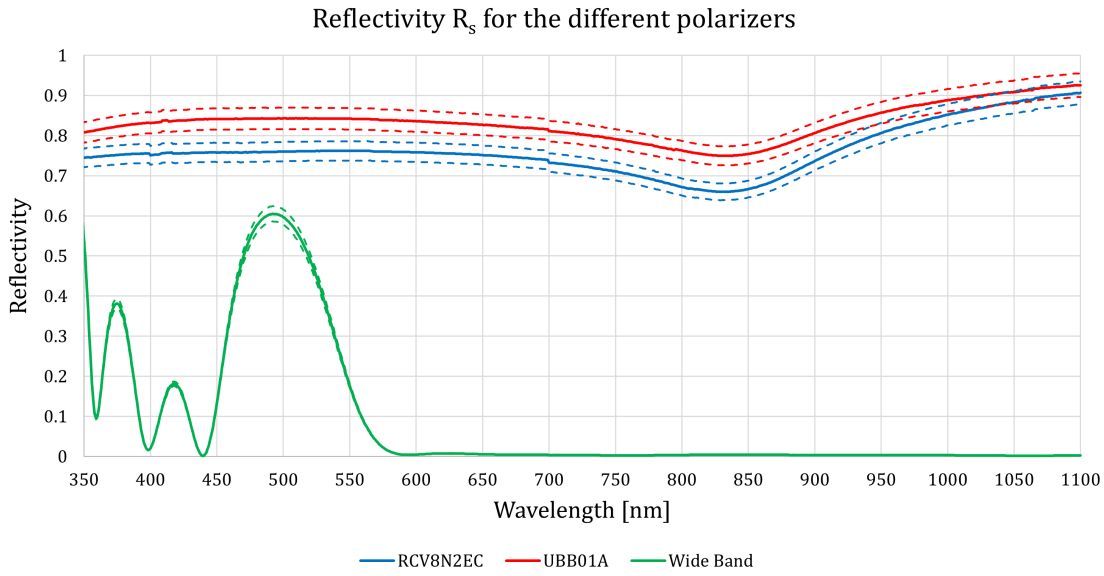


Figure 5.29: Reflectivity R_s of Moxtek RCV8N2EC, Moxtek UBB01A, Polarcor Wide Band polarizers with a 10° AOI, in the wavelength range 350-1100 nm. Dashed lines give the confidence range of the measurements.

In Figures 5.30 and 5.31 the absorption A_p and A_s for the different polarizers are depicted. The absorption is given by $A_i = 1 - (T_i + R_i)$ [6]. The absorption has to be calculated using the transmissivity and reflectivity in the same configurations. In this work the two optical properties have been measured with different incident angles, AOI = 0° for the transmissivity and AOI = 10°, 15° and 20° for the reflectivity. Consequently, to compute the absorption an approximation has been necessary, in particular, the reflectivity at 0° AOI has been approximated to that at 10°, overestimating the absorption results.

An ideal selective absorption filter should have $A_p = 0$ and $A_s = 1$. From the plots it can be observed that Polarcor polarizer is clearly based on selective absorption since from wavelength greater than 700 nm, A_p is almost equal to zero, while As is equal to 1. on the other hand, Moxtek filters work mainly by reflecting the s-component, even though there is a 20-30% of absorption.

Overall, it can be observed that Polarcor polarizer's absorption is higher than that of Moxtek filters in both A_p and A_s. Moreover, the Wide Band polarizer behavior is steadier over 600 nm and gradually decreases in the p-direction with the increase of the wavelength, while it approaches the 100% in the s-direction. While A_p is approximately the same for the two Moxtek filters, RCV8N2EC A_s is 8% higher than that of UBB01A in EnVisS operational range.

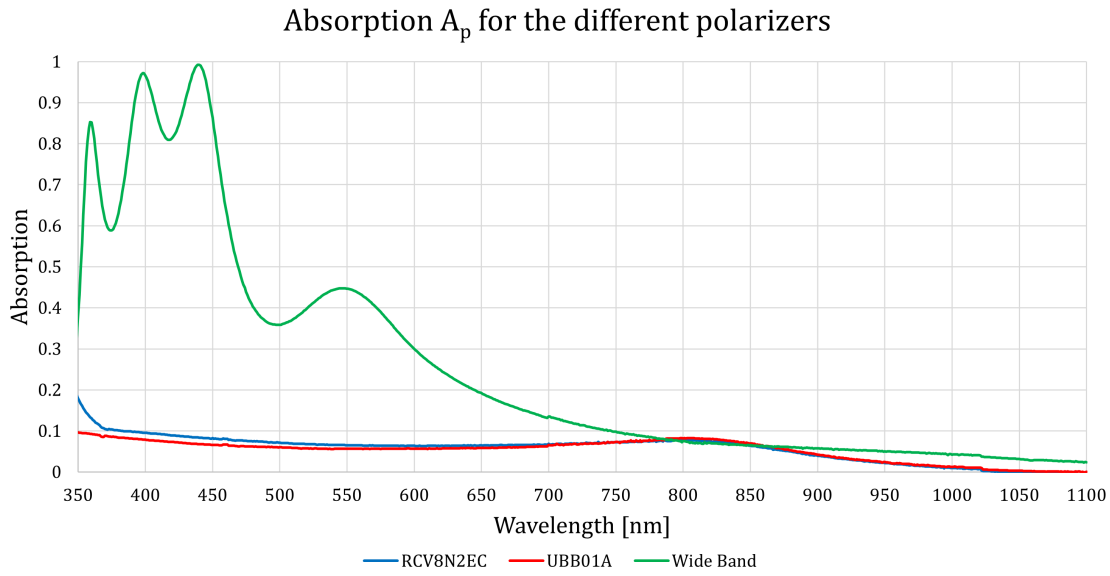


Figure 5.30: Absorption A_p of Moxtek RCV8N2EC, Moxtek UBB01A, Polarcor Wide Band polarizers.

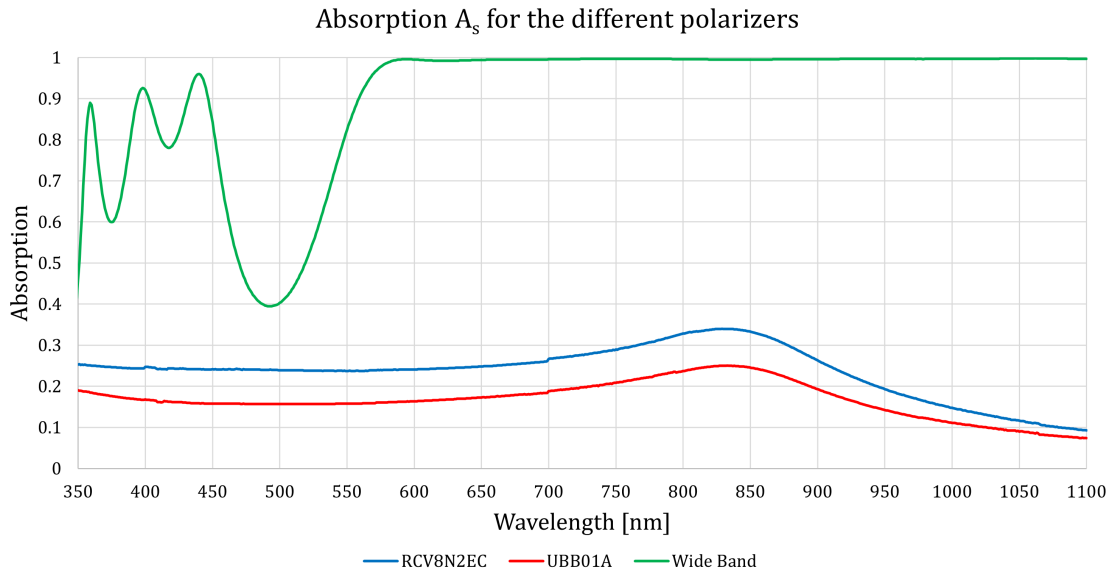


Figure 5.31: Absorption A_s of Moxtek RCV8N2EC, Moxtek UBB01A, Polarcor Wide Band polarizers.

Finally, in Figure 5.32 the contrast ratio is shown. Since Polarcor filter has a high T_p and a low T_s, the highest CR belongs to the Wide Band polarizer, which is up to twice that of the Moxtek polarizing filters. As already shown in the previous paragraphs, the curves display

CR values with peaks of 6700 for Moxtek UBB01A, 7000 for Moxtek RCV8N2EC, and 16000 for Polarcor Wide Band.

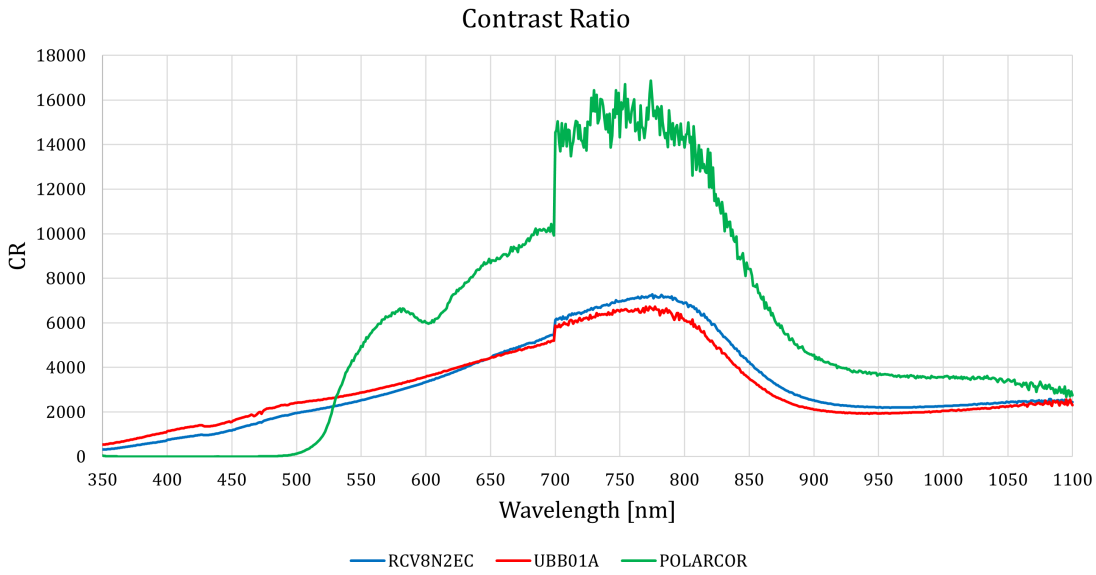


Figure 5.32: Contrast ratio of Moxtek RCV8N2EC, Moxtek UBB01A, Polarcor Wide Band polarizers.

In conclusion, the obtained contrast ratio results prove that all the three candidate polarizers for EnVisS filter strip assembly have optimal performance. From the analysis of the transmissivity and reflectivity it can be pointed out that Polarcor Wide Band polarizer does not meet the scientific performance required for EnVisS purposes in its operational wavelength range, leaving Moxtek polarizing filters as the only candidates. Moreover, Moxtek RCV8N2EC and UBB01A have approximately the same level of performance, but due to its fused silica substrate, Moxtek UBB01A polarizing filter is the best candidate for EnVisS FSA.

5.2 Topography

As illustrated in Chapter 3.2, the three polarizing filters under examination have been subjected to a surface morphology analysis. These tests have been performed by means of the XE-70 Park System Atomic Force Microscope in true non-contact mode, available in the CNR-IFN laboratories in Padua.

This analysis has been particularly relevant to evaluate the topography of the Moxtek's filters since they present a nanometric wire-grid structure, as it will be shown in the following

paragraphs.

For each polarizing filter only one side has been tested; in particular, for Moxtek's polarizers only the surface presenting the wire-grid structure has been characterized, while, since Polarcor filter presents no difference between the two sides, the tested surface of the Wide Band polarizer has been chosen arbitrarily.

In the next paragraphs the resulting topography has been reported, where the image scan size has been set to $1 \times 1\ \mu m^2$.

5.2.1 Moxtek RCV8N2EC

Moxtek RCV8N2EC polarizing filter presents a nanometric wire-grid structure on one side, as it can be clearly seen in Figure 5.33. This image represents the topography of the surface; to better characterize the surface structure, two lines have been drawn perpendicularly to the wires.

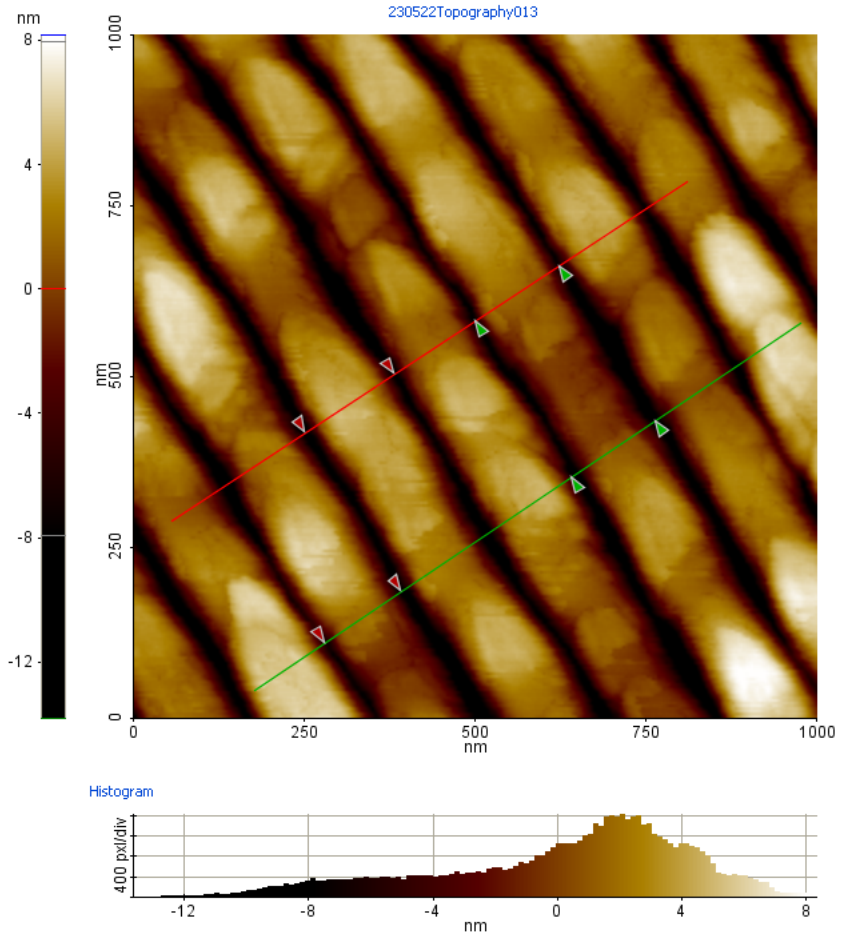
The table in Figure 5.33b shows the wires surface properties along the red and green lines. In particular, the reported properties are: minimum and maximum height of the wire-grid structure and their mid value, the mean value of the height of the overall wires considered, and different linear roughness parameters[3]. It can be observed that the values reported for the two lines are slightly different. Since we are talking about nanometric structures, this difference is probably due to uncertainties in the measurements or in the manufacturing of the filter itself.

In Figure 5.34[4], a 2D plot of filter's topography is shown. Moreover, different points have been selected to better define the structure.

From this imaging it is possible to establish that Moxtek RCV8N2EC wire-grid structure has wires with approximately 10-12 nm height and period between 135 and 155 nm.

[3] A brief explanation of the roughness parameters is reported in Appendix 8.6.

[4] Note that in the tables of this figure, ΔX and ΔY are the horizontal and vertical difference between the cursors of the same colors, while "Angle" represents the angle between these points, which, in radiance, is determined by dividing the vertical difference by the horizontal difference.



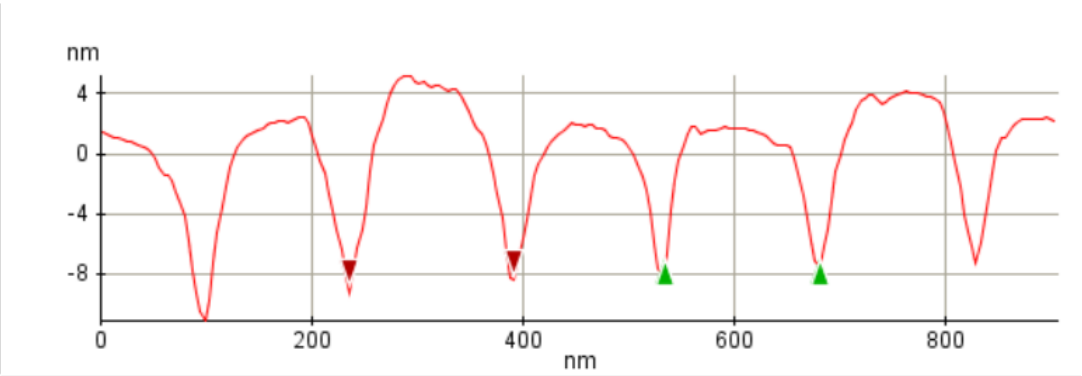
(a)

Statistics

Line	Min(nm)	Max(nm)	Mid(nm)	Mean(nm)	Rpv(nm)	Rq(nm)	Ra(nm)	Rz(nm)	Rsk	Rku
Red	-11.135	5.173	-2.981	-0.082	16.308	3.613	2.852	13.487	1.024	3.310
Green	-9.300	6.403	-1.448	0.284	15.703	4.166	3.335	15.205	0.578	2.492

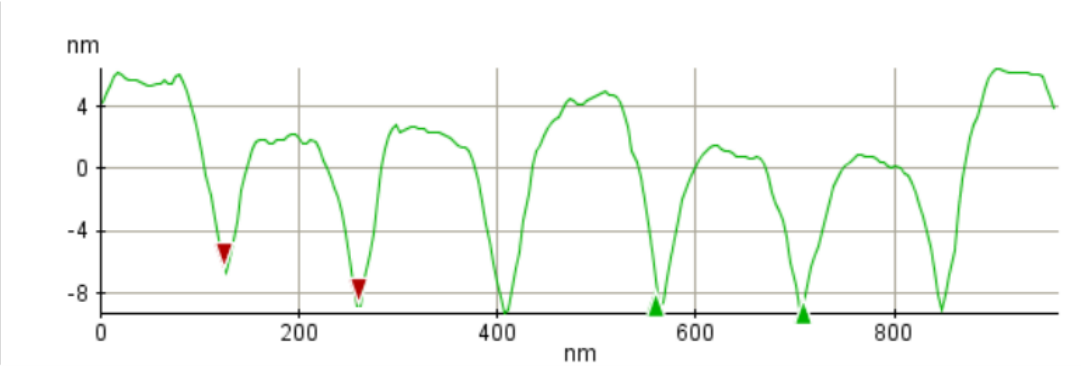
(b)

Figure 5.33: Topography of Moxtek RCV8N2EC wire-grid structure and its roughness parameters.



Cursor	ΔX(nm)	ΔY(nm)	Angle(deg)
Red	155.762	0.564	0.208
Green	146.912	-0.004	-0.002

(a)



Cursor	ΔX(nm)	ΔY(nm)	Angle(deg)
Red	135.681	-2.287	-0.966
Green	148.872	-0.578	-0.223

(b)

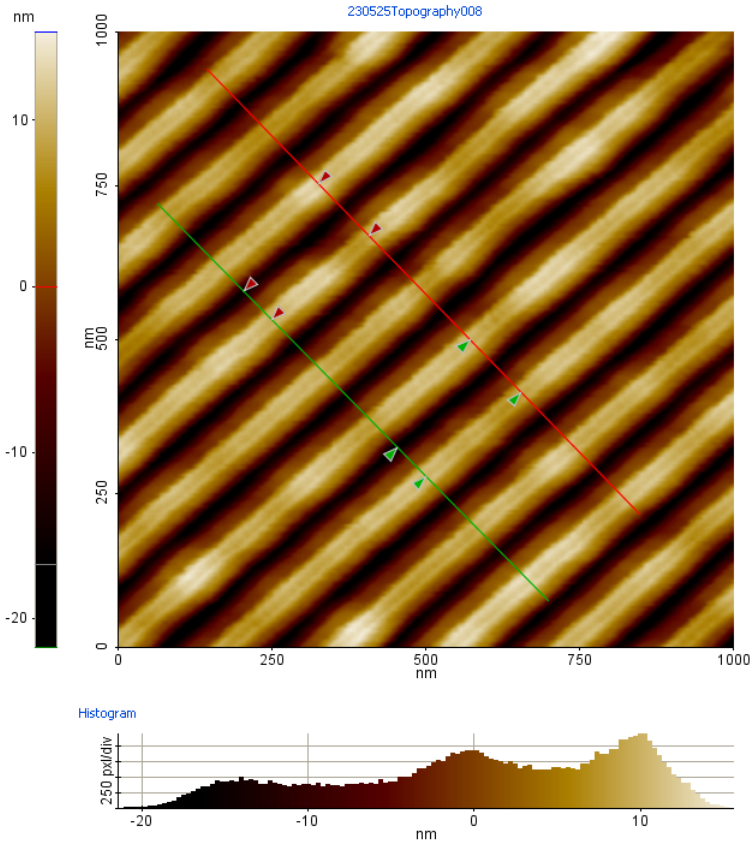
Figure 5.34: 2D plot of the Moxtek RCV8N2EC wires height as a function of the sampling length.

5.2.2 Moxtek UBB01A

The same operational procedure has been carried out for the other Moxtek polarizer: UBB01A. As the previous filter, the UBB01A polarizer presents a nanometric wire-grid structure on one side and its topography is shown in Figure 5.35.

The first thing that comes to notice is that this scan looks more homogeneous than the

one presented for Moxtek RCV8N2EC polarizer. This is due to the quality of the used tip, in fact, even though for all the measurements a brand new tip has been used, they are very easily subjected to wear and contamination, hence the different quality of the images. Another possible reason for this difference is the background noise and possible vibrations in the working place, which make the imaging quality worse.



(a)

Statistics

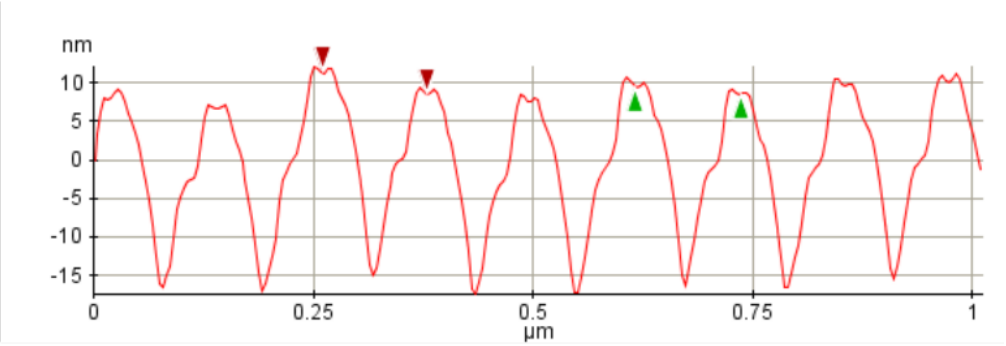
Line	Min(nm)	Max(nm)	Mid(nm)	Mean(nm)	Rpv(nm)	Rq(nm)	Ra(nm)	Rz(nm)	Rsk	Rku
Red	-17.451	12.056	-2.698	-0.204	29.507	8.306	6.954	28.311	0.489	2.123
Green	-17.933	13.759	-2.087	0.380	31.692	8.384	7.006	28.461	0.514	2.173

(b)

Figure 5.35: Topography of Moxtek UBB01A wire-grid structure and its roughness parameters.

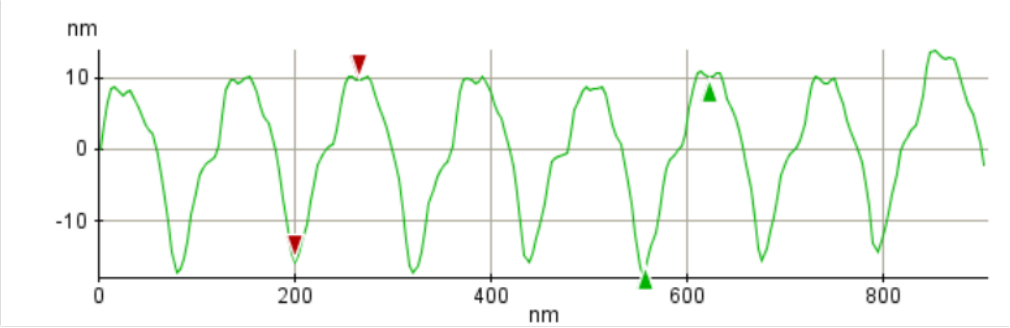
As done for the other Moxtek filter, in the topography two lines have been drawn perpendicularly to the wires in order to better characterize the structure, and their 2D plots are shown in Figure 5.36.

From this analysis comes out that the wires height is approximately 25-30 nm and have period of about 120 nm.



Cursor	ΔX(nm)	ΔY(nm)	Angle(deg)
Red	118.561	-2.818	-1.362
Green	120.537	-0.881	-0.419

(a)



Cursor	ΔX(nm)	ΔY(nm)	Angle(deg)
Red	65.491	25.031	20.917
Green	65.491	26.180	21.789

(b)

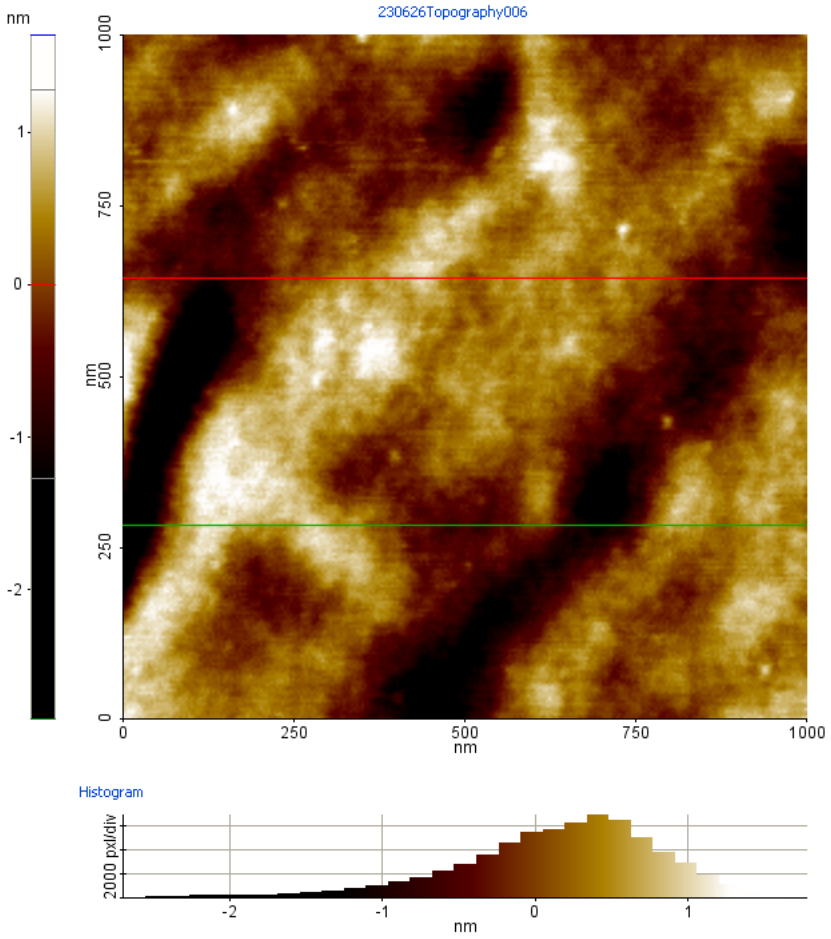
Figure 5.36: 2D plot of the Moxtek RCV8N2EC wires height as a function of the sampling length.

It can be observed that Moxtek UBB01A polarizer has higher and closer wires than RCV8N2EC, which proves because the operational spectral range of this polarizer starts at 300 nm, while RCV8N2EC's from 420 nm[5].

[5] Remember that a wire-grid polarizer consists of a metallic grating with period smaller than the wavelength for which the filter is used [10], hence, the smaller the period, the smaller the wavelength which can be polarized.

5.2.3 Polarcor Wide Band

The last analyzed filter is Polarcor Wide Band polarizer, whose functioning is based on selective absorption due to its material anisotropy, hence, it does not present any type of structure, as it can be clearly seen in Figure 5.37.



(a)

Statistics

Line	Min(nm)	Max(nm)	Mid(nm)	Mean(nm)	Rpv(nm)	Rq(nm)	Ra(nm)	Rz(nm)	Rsk	Rku
Red	-0.966	1.033	0.034	0.000	2.000	0.522	0.457	1.728	0.081	1.829
Green	-2.246	1.268	-0.489	0.000	3.514	0.785	0.661	2.694	0.689	2.847

(b)

Figure 5.37: Topography of Polarcor Wide Band polarizer and its roughness parameters.

The general roughness parameters are obviously smaller than those presented by the Moxtek filters, and do not show periodicity (see Figure 5.38).

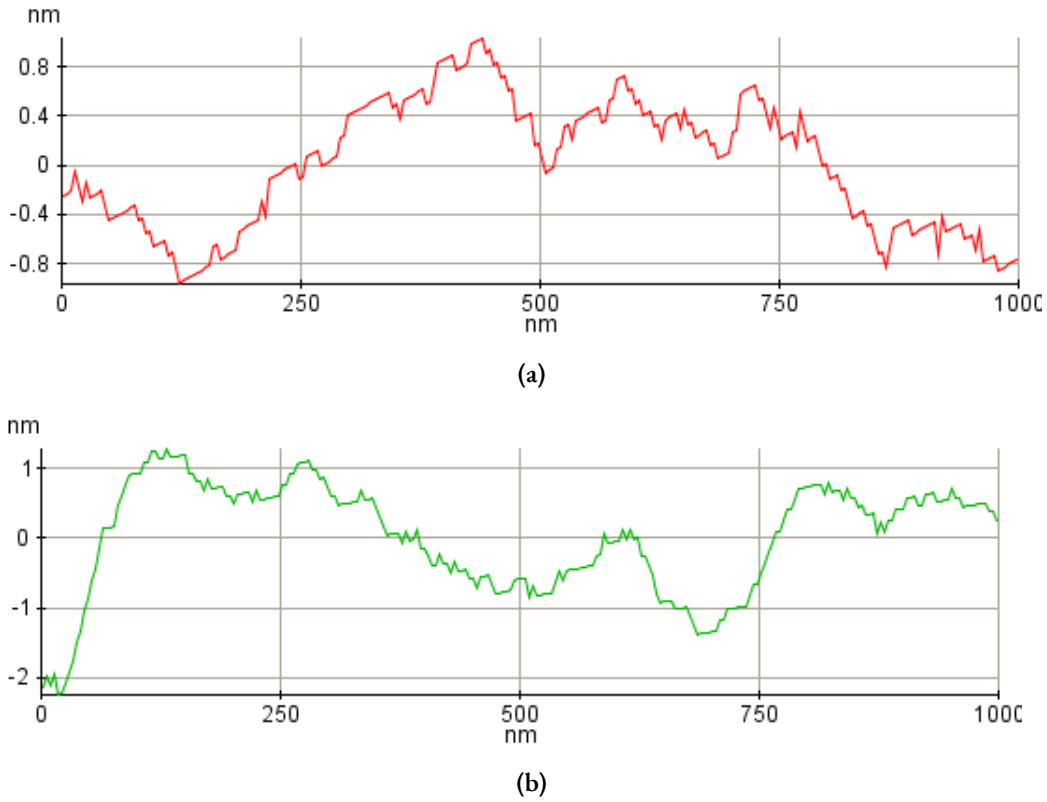


Figure 5.38: 2D plot of the Polarcor Wide Band polarizer roughness as a function of the sampling length.

5.3 Finite Element Analysis

In Chapter 4, the finite element analysis performed on the system composed by EnVisS filter strip assembly, its mounting frame and the glue layers linking the two, has been explained. The simulations have been carried out by means of the Patran-Nastran software to study the changes of the system when subjected to quasi-static accelerations and non-planarity of the mechanical interface. In particular, the aim of the analysis is to understand if the system is subjected to failure due to different physical phenomena, hence, the results reported in this chapter are in terms of deformation and stress distribution on the system[6].

[6]Note that the reported results are obtained from a preliminary analysis in which only EnVisS described subsystem has been tested. For a more accurate evaluation of the behaviour of the subsystem the entire instrument should be considered.

A particular attention has been paid to the stress level on the adhesive layers, to verify that the gluing is keeping the system together without breaking.

5.3.1 Quasi-static acceleration effect

The first simulation shows the mechanical changes of the system due to a quasi-static inertial load of 56g acting along one direction. The analysis has been performed with the load acting along the x, y and z-directions both in the positive and negative verse.

Since the system is symmetric with respect to the x and y-axes, the behaviour of the structure when subjected to 56g along the positive x-direction is the same (speculated) of that with 56g along the negative x-direction, same applies with the inertial load along the positive and negative y-direction. Consequently, in this chapter only the results obtained with the load along the positive x and y-directions, and both positive and negative z-direction have been presented.

In Figures 5.39, 5.40, 5.41 and 5.42 the deformations of the system when under a 56g inertial load along the aforementioned directions are shown[7]. It can be observed that in each simulation the area around the six pinned through holes is the least subjected to deformation with displacements from tens to a few hundreds nanometers, while the most deformed areas change with the direction in which the inertial load is applied.

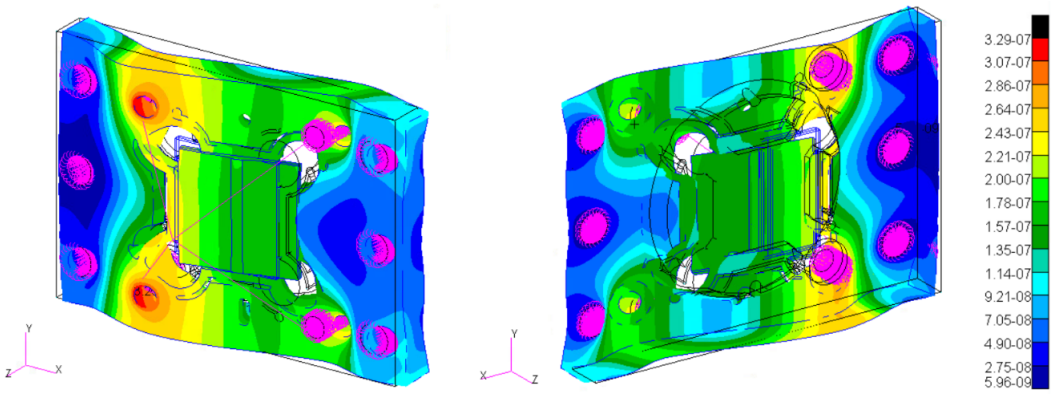


Figure 5.39: Deformation of the analyzed system when subjected to 56g inertial load along the positive x-axis.

[7]Note that the images also show the undeformed configuration of the model.

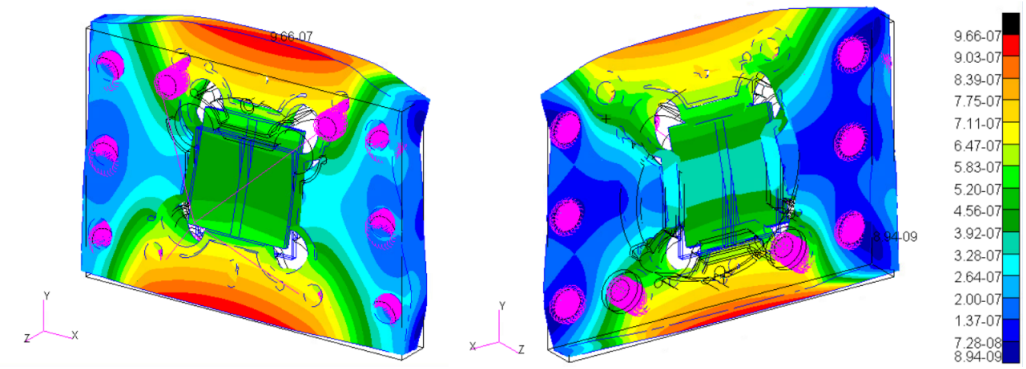


Figure 5.40: Deformation of the analyzed system when subjected to 56g inertial load along the positive y-axis.

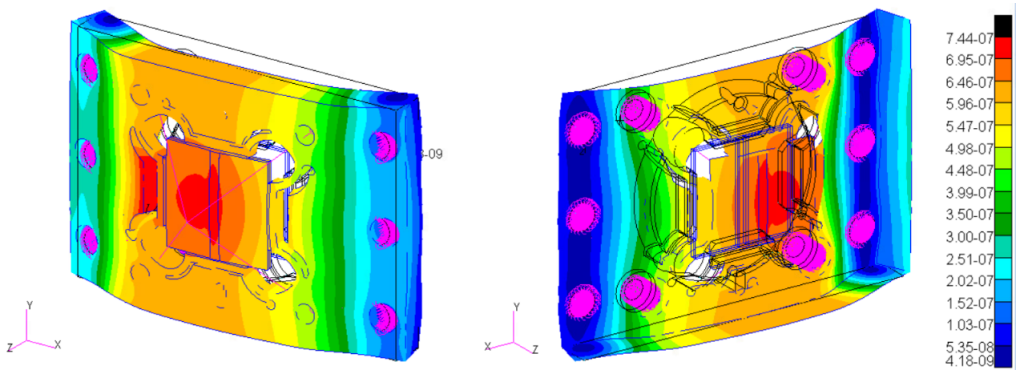


Figure 5.41: Deformation of the analyzed system when subjected to 56g inertial load along the positive z-axis.

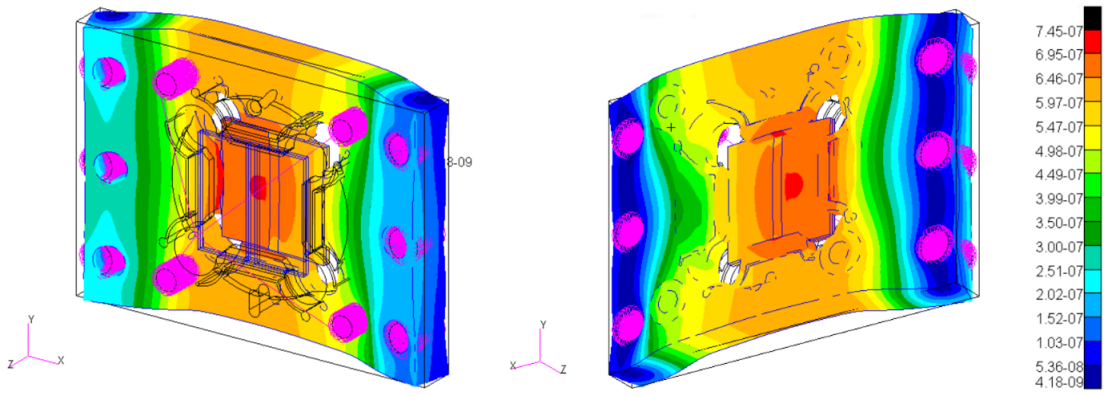


Figure 5.42: Deformation of the analyzed system when subjected to 56g inertial load along the negative z-axis.

When the 56g load is acting along the x-axis the four internal holes connecting the system to the camera package are the ones that show the larger displacement, while for the inertial

load applied in the y-direction the top and bottom part of the mounting frame are the most deformed ones. Regarding the load acting along the z-direction, the central part of the system is the most subjected to deformation. Between the case of the load applied in the positive direction and that on the negative one only small differences in terms of magnitude and deformation distribution are shown.

Overall, the maximum translational displacement is shown when the system is subjected to 56g inertial load along the positive y-axis, reaching almost 1 µm, whereas in the other cases the shown deformation is slightly smaller. These deformations fit the tolerable displacements of the system without affecting its optical performance.

Furthermore, with these analysis the stress distribution on the system has been studied. Since the results obtained in the different load configurations do not show significant differences, in this chapter only the results of the simulation with 56g inertial load along the x-axis has been reported, while the remaining results are presented in Appendix 8.5.

In Figure 5.43 the von Mises stress distribution[8] on the entire system is shown.

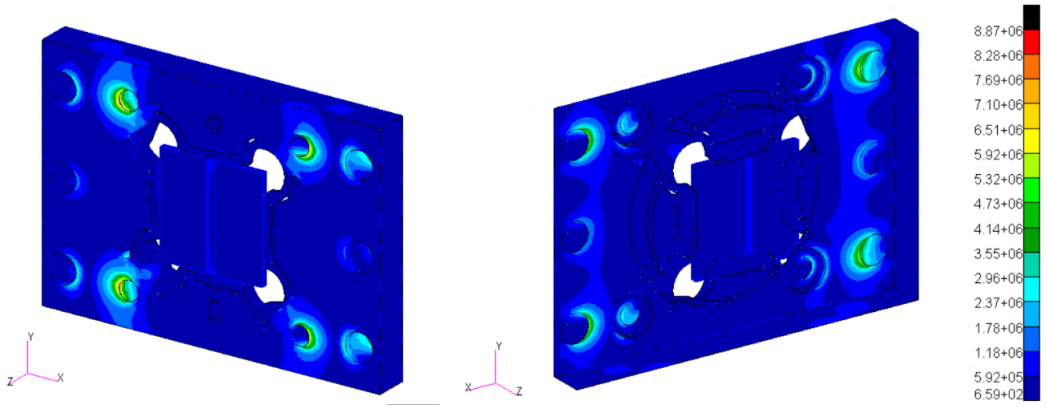


Figure 5.43: Von Mises stress distribution on the analyzed system when subjected to 56g inertial load along the positive x-axis.

It can be observed that, being the zone of interface between the system and the remaining part of the instrument, the most stressed areas are those in correspondence of the through

[8]Remember that the von Mises stress is a scalar quantity derived from the stress tensor used to determine if a given material yields or fracture when under a certain load. In the most general case it is calculated as:

$$\sigma_{VM} = \sqrt{\frac{1}{2}[(\sigma_1 - \sigma_2)^2 + (\sigma_2 - \sigma_3)^2 + (\sigma_3 - \sigma_1)^2] + 3(\tau_1^2 + \tau_2^2 + \tau_3^2)}$$

where σ_1, σ_2 and σ_3 are the stresses along the principal axis, and τ_1, τ_2 and τ_3 are the shear stresses.

holes showing a maximum of almost 10 MPa. These values of stress are low compared to the ones that the system can bear, proving that it will not fracture when subjected to 56g quasi-static acceleration.

Moreover, in this analysis a particular interest has been addressed to the stress distribution on the glue layers, to assure that the level of stress acting on the system does not exceed the overlap shear strength[9] of the glue, thus, creating a detachment of the FSA from the mounting frame.

For these results, the von Mises stresses and also the X and Y-component of the stress tensor (which represent the stress acting in the x and y-directions, respectively) have been used to provide both an overall measurement of the equivalent stress and information about the stress distribution along a particular axis acting on the glue layers.

From the Ec9323-2 glue datasheet, the overlap shear strength of the adhesive in the non-operational temperature range of EnVisS (−40°C-70°C) is approximately between 12 and 30 MPa.

Figure 5.44 shows that the maximum value of the von Mises stress is a little over 2 MPa, proving that the glue layers will not detach when subjected to 56g inertial load along the x-axis.

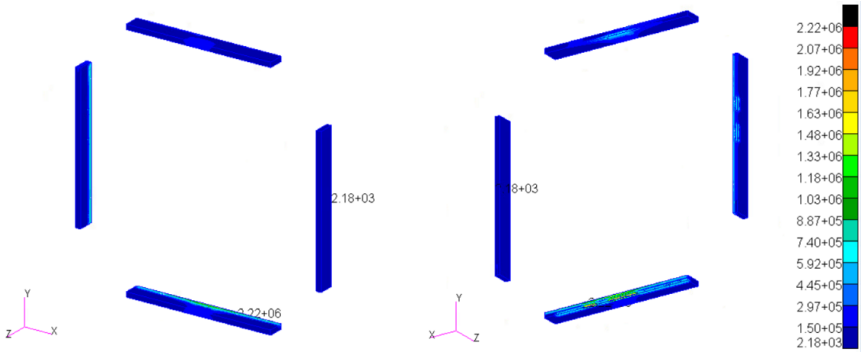


Figure 5.44: Von Mises stress distribution on the glue layers when subjected to 56g inertial load along the positive x-axis.

The X and Y-component of the stress tensor will be smaller than the von Mises stress, so it can already be concluded that the system will not be subjected to yields or fractures. Notheless, in Figures 5.45 and 5.46 the results of the X and Y-components of the stress tensor acting on the glue layers are shown. In Figure 5.47 a zoom of a vertical glue layer with

[9]The overlap shear stress is the measure of the maximum shear stress that an adhesive material can withstand before failure or loss of structural integrity.

X-component stress distribution and an horizontal glue layer with Y-component stress distribution is reported to highlight the critical areas subjected to the stresses along these particular axes.

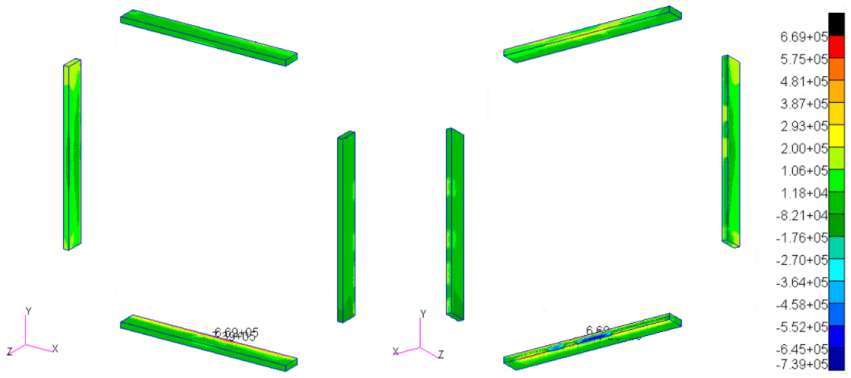


Figure 5.45: X-component of the stress tensor acting on the glue layers when subjected to 56g inertial load along the positive x-axis.

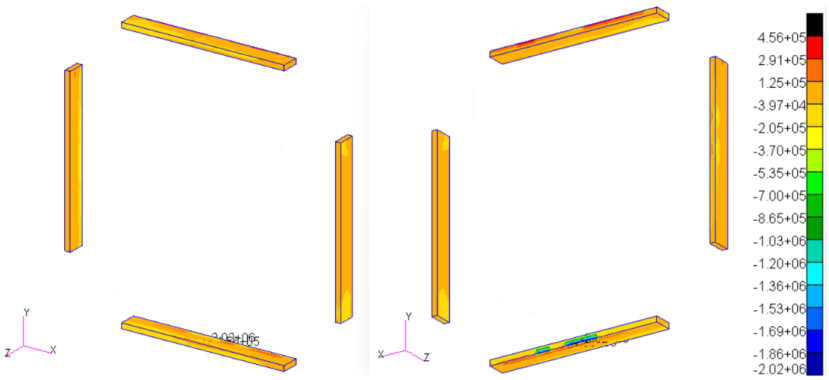
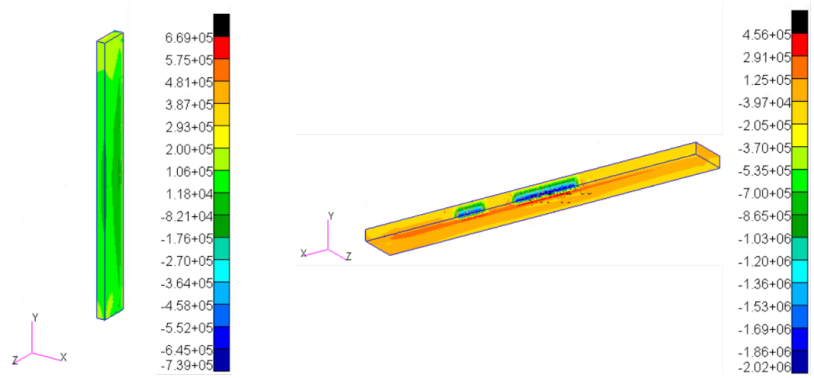


Figure 5.46: Y-component of the stress tensor acting on the glue layers when subjected to 56g inertial load along the positive x-axis.

5.3.2 Non-planarity of the mechanical interface

As explained in the previous chapter, another effect that has been analyzed is the non-planarity of the mechanical interface between the support structure and the FSA, to simulate the wrong assembly of the mounting frame with respect to the remaining part of the optical instrument.

At first, this effect has been simulated in a worst case scenario with a displacement of 100 µm in the positive z-axis in correspondence of one of the nodes representing the screws link-



(a) **(b)**

Figure 5.47: Zoom on one of the vertical/horizontal glue layers to highlight the X and Y-component stress tensor on the most critical glue area, when subjected to 56g inertial load along the positive x-axis.

ing the mount to the instrument. This simulation has been performed for each of the six nodes to better see the overall effect of the non-planarity in terms of displacements and stress distribution.

For simplicity, since the analyzed structure is symmetric with respect to both the x and y-axes, only the results obtained by imposing the displacement on one of the corners holes and a central one have been reported. In particular, in this paragraph, the results achieved by moving the top left corner through hole have been illustrated, while the effect of the displacement on one of the central screws is shown in Appendix 8.5.

In Figure 5.48 the deformation of the model is shown. As expected, the most deformed area is in correspondence of the top left corner, showing a maximum displacement of 1.37×10^{-4} m.

Moreover, the von Mises stress distribution on the system in Figure 5.49 shows significant values, reaching a maximum of 685 MPa in correspondence of the interface areas. This stress value is greater than the ultimate tensile strength of the aluminum, proving that under these conditions the system will break. Once again, the performed simulation wants to be a preliminary analysis, so the high values of stress in correspondence of the six through holes are not representative of the realistic ones since the screws have been modeled as RBE2. To achieve more accurate stress values in those areas, a more detailed model is needed.

As for the previous simulation, a particular interest has been placed on the stress distribution on the glue layers of the system. In Figures 5.50, 5.51 and 5.52, the von Mises stress and the X and Y-component of the stress tensor distribution are shown.

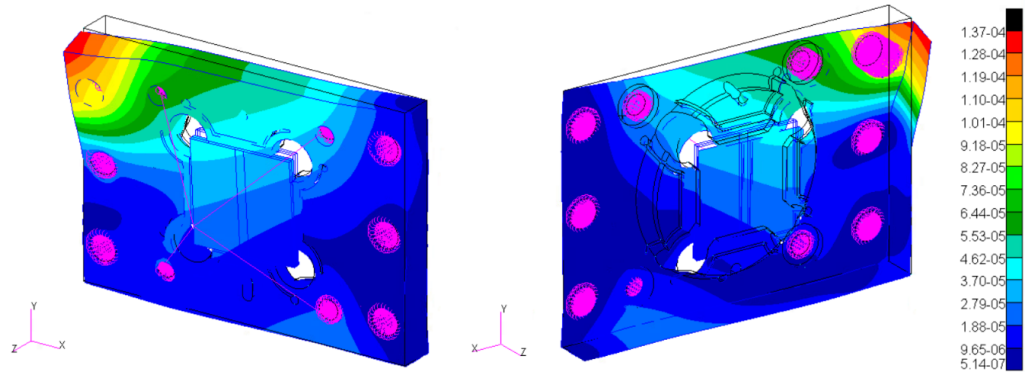


Figure 5.48: Deformation of the analyzed system when subjected to a 100 μm displacement of one of the pinned nodes.

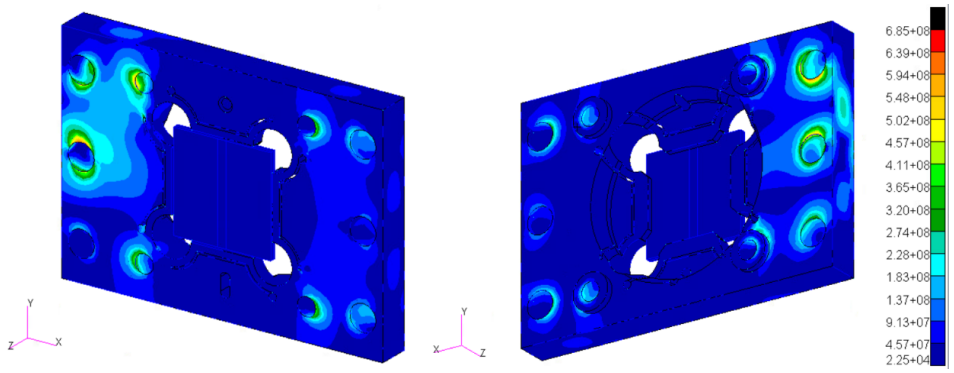


Figure 5.49: Von Mises stress distribution on the analyzed system when subjected to a 100 μm displacement of one of the pinned nodes.

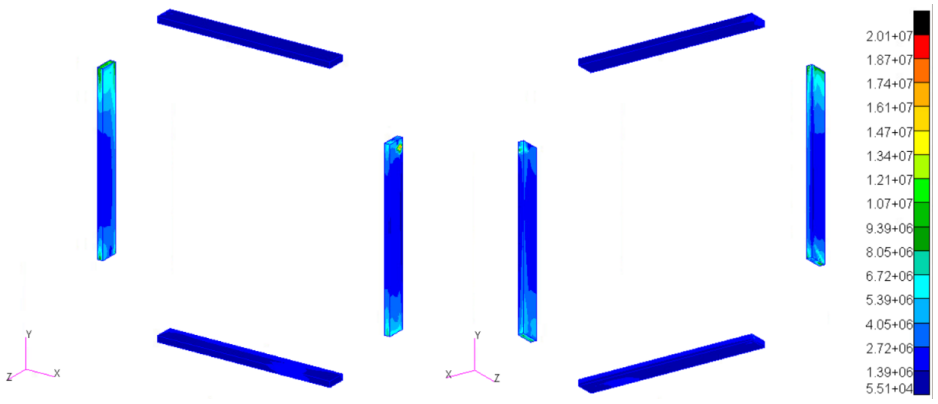


Figure 5.50: Von Mises stress distribution on the glue layers when subjected to a 100 μm displacement of one of the pinned nodes.

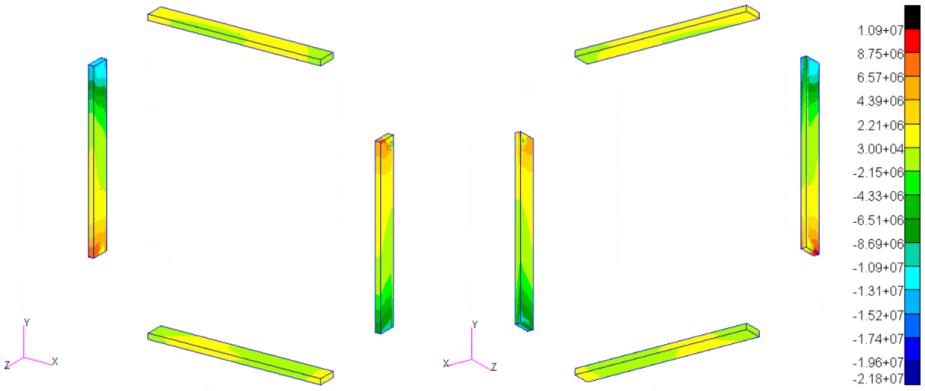


Figure 5.51: X-component of the stress tensor acting on the glue layers when subjected to a 100 µm displacement of one of the pinned nodes.

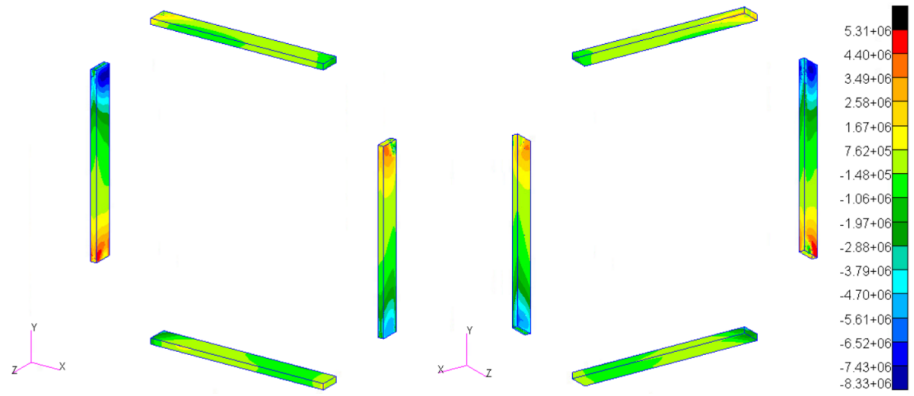


Figure 5.52: Y-component of the stress tensor acting on the glue layers when subjected to a 100 µm displacement of one of the pinned nodes.

It can be observed that the stress values are significantly lower than those acting on the entire system and the X and Y-component fall within the overlap shear strength of the glue, showing that even under these extreme conditions the adhesive would held.

Moreover, since the displacements to which the system is subjected are small and the behaviour of the different materials is supposed linear, it has been assumed that the entire system behaviour is linear. Consequently, to analyze a more realistic non-planarity error, such as 5 µm displacement, a scaling of a factor 20 of the previous result has been computed.

The distribution of the stress and deformation is the same shown in the previous figures, whereas the maximum deformation is 6.85 µm and the maximum stress on the entire system is 34.25 MPa. These values prove that the system will not yield when subjected to a 5 µm displacement of one of the nodes and that its optical performance will not be affected.

The same procedure can be done for the glue stress distribution, achieving even smaller stress values, demonstrating once again that the adhesive will not be subjected to detachment.

6

Future activities

Further development of the EnVisS space camera are planned for the next next years. In Table 6.1 the main EnVisS milestones are listed.

Milestone	Date
Instrument Critical Design Review (I-CDR) data packages to be delivered to ESA	September 4th, 2023
Instrument EFM and STM Delivery Review Board (DRB)	February 1st, 2024
End of EFM and STM campaigns	September, 2024
Instrument PFM Delivery Review Board (DRB)	October 1st, 2025
Probe B2 integration and functional tests	Q1 2026
Payload Qualification and Acceptance Review (QAR) completed by	Q1 2026
Delivery of integrated B1 and B2	Q2 2026
End of S/C integration and functional tests	Q4 2026

Table 6.1: EnVisS main milestones. EFM, STM and PFM stand for Electrical/Engineering Functional Model, Structural and Thermal Model, and Proto-Flight Model respectively.

Comet Interceptor will be launched in 2029, so EnVisS high level schedule follows that of the mission. It is evident that the schedule is very tight: the CDR is foreseen in just a few months from now, and then the PFM has to be delivered to ESA after two years. This will require great efforts of all the teams involved in the project.

The CNR-IFN team (Padua) in collaboration with Leonardo SpA (Campi Bisanzio, Florence) will first contribute to the completion of the instrument CDR. Then, while industry will start the instrument development phase, we will continue to work on the BreadBoard (BB) to learn as much as possible from this prototype, by means of optical tests, by estimating the instrument performance, by developing suitable software for a proper data analysis and calibration, and so on. Then, we will contribute to all the experimental activies relative to the PFM: in particular, we will participate to the Alignment, Integration, Test and Verification (AIT/AIV), where we will take advantage of the insights learned with the instrument breadboard. With the instrument aligned, it will be then possible to perform the on-ground calibration activities, to be realized before the DRB of October 1st 2025. After this deadline, the collected pre-flight data will be analyzed and elaborated to characterize the instrument optical performance and to define a suitable calibration pipeline for the scientific use of the in-flight collected data. In addition, the EnVisS radiometric model will be realized to estimate the actual instrument signal-to-noise ratio as a function of the integration time.

These, and many other activities that will be done before and after the instrument delivery to ESA, are fundamental steps in the process of getting the better knowledge of the instrument working process and of the data analysis. They will allow to finally obtain the best possible calibrated datasets of the target comet, from which scientists will be able to perform in an optimal way the foreseen science and to reach the expected scientific objectives.

7

Conclusions

EnVisS is a all-sky camera that will fly aboard the Comet Interceptor mission and aims to dynamically image, in the visible range, the coma of a long period comet yet to be discovered. Before reaching the detector, the light reflected from the comet coma entering the optical instrument will cross a filter strip assembly composed of a central broadband filter and two lateral linear polarizers.

For the latters, three different polarizing filters have been characterized in the laboratory of CNR-IFN in Padua: Moxtek RCV8N2EC, Moxtek UBB01A and Polarcor Wide Band. The filters optical properties have been measured and then compared to each other and to data given by the supplier, to better understand which polarizer has the most fitting properties for EnVisS scientific task. The setup used for the tests is the Bentham Reflectometer available in the CNR-IFN laboratories and the configuration of its stages differs between the different types of analysis.

Overall, measurements of the filters' transmissivity and reflectivity agree with those provided by the supplier and mostly fit EnVisS' purposes thanks to their optimal performance.

From the optical analysis it has been observed that Polarcor Wide Band polarizer does not meet the required scientific performance for EnVisS purposes in its entire operational wavelength range, leaving Moxtek polarizing filters as the only candidates. Both Moxtek filters have approximately the same level of performance, but due to its fused silica substrate, it has been concluded that Moxtek UBB01A polarizing filter is the best candidate for EnVisS FSA.

Moreover, by means of the XE-70 Park Atomic Force Microscope, available in the CNR-

IFN laboratories, these filters' topography has been studied and, in particular, it has been possible to measure the Moxtek polarizers nano-wire structure properties in terms of height and period of the wires.

In addition, a Finite Element Analysis on the EnVisS subsystem composed by the FSA, its supporting structure and the glue layers linking the two, has been performed to study the behaviour of the system when subjected to different physical phenomena. It has been demonstrated that a quasi-static inertial load of 56g and a non-planarity of the mounting frame of 5 µm elastically deform the system inducing stress levels far below the limit stresses of materials and glue. These results will also have to be confirmed by a further refined model including the supporting structure of the 3D-Plus package which, at the moment, has been considered preliminarly as a rigid body.

Future tests will be performed on both the chosen polarizing filter and the filter strip assembly, to deepen the knowledge of these components and their properties. Furthermore, in the next few years, the CNR-IFN team in collaboration with Leonardo SpA will contribute to the completion of the whole EnViS camera, for it to be launched aboard the Comet Interceptor mission by the end of 2029.

8 Appendix

8.1 Electromagnetic spectrum

Thanks to the work of J.C. Maxwell and the following studies, light is considered to have electromagnetic nature since the end of the 1800s.

With the classical electrodynamics theory, light can be described as a continuous transfer of energy by means of electromagnetic waves [6]. On the other hand, with the more modern view of quantum electrodynamics, the electromagnetic interaction and transport of energy are described in terms of photons, defined as massless elementary particles. This dual nature of light can be clearly seen considering that light propagates through space in form of a wave, while it shows particle-like behavior during the process of emission and absorption. In several optics applications, the quantum nature of light radiation is not of practical interest, as in this work where light will be considered as an electromagnetic wave.

The classical electromagnetic field equations of Maxwell describe the wave nature of light, which, in vacuum conditions (charge density $\rho = 0$ and current density $j = 0$), can be

written in differential form as:

$$\begin{cases} \vec{\nabla} \cdot \vec{E} = 0 \\ \vec{\nabla} \cdot \vec{B} = 0 \\ \vec{\nabla} \times \vec{E} = -\dfrac{\partial \vec{B}}{\partial t} \\ \vec{\nabla} \times \vec{B} = \varepsilon_0 \mu_0 \dfrac{\partial \vec{E}}{\partial t} \end{cases}$$

Here $\vec{E}$ and $\vec{B}$ are the electrical and magnetic fields, while ε_0 and μ_0 are the dielectric constant and the magnetic permeability of the vacuum, respectively.

These equations can be manipulated into the form of two vector expressions, commonly known as wave equations or D'Alembert equations:

$$\begin{cases} \nabla^2 \vec{E} = \varepsilon_0 \mu_0 \dfrac{\partial^2 \vec{E}}{\partial t^2} \\ \nabla^2 \vec{B} = \varepsilon_0 \mu_0 \dfrac{\partial^2 \vec{B}}{\partial t^2} \end{cases}$$

By solving these equations it can be found (always considering free space) that the propagation speed of electromagnetic waves in vacuum is

$$v = \frac{1}{\sqrt{\varepsilon_0 \mu_0}} = c = 2.99792458 \cdot 10^8 \text{ m/s}$$

The D'Alembert equations relate the space and time variation of a physical quantity and describe wave phenomena. Each and every component of the electromagnetic field obeys the scalar differential wave equation:

$$\frac{\partial^2 \psi}{\partial x^2} + \frac{\partial^2 \psi}{\partial y^2} + \frac{\partial^2 \psi}{\partial z^2} = \frac{1}{v^2} \frac{\partial^2 \psi}{\partial t^2}$$

Using Maxwell equations and the wave ones, it can be found that the magnetic and electrical fields propagate in free space with velocity c and are perpendicular to each other and to the propagation direction. Assuming, for simplicity, a wave propagating along the positive z direction and an electrical field oscillating along the x axis, the equations of the two fields

are:

$$\vec{E}_x(z,t) = E_{0x}\cos(kz - \omega t)$$
$$\vec{B}_y(z,t) = \frac{1}{c}E_{0x}\cos(kz - \omega t)$$

with $k = \frac{2\pi}{\lambda}$ (λ, wavelength [nm]) and $\omega = 2\pi f$ (ω, wave angular frequency [rad/s]; f frequency [Hz]).

These transverse waves that propagate through space form the electromagnetic radiation. Depending on the frequency of oscillation (which can vary from 1 kHz to 10^{22} Hz), different wavelengths of electromagnetic spectrum are produced, and the mode of interaction between waves and matter varies.

Visible light is only a small portion of this electromagnetic spectrum (Figure 8.1). The radiation which is visible to the human eye has wavelength in the range 390-780 nm and frequency in the range between 3.84×10^{14} and 7.69×10^{14} Hz.

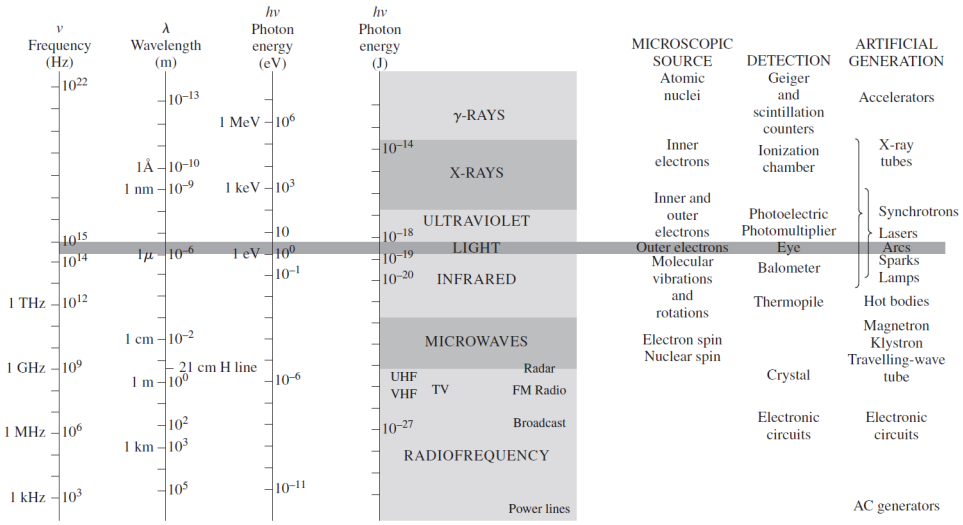


Figure 8.1: Electromagnetic spectrum.

8.2 Polarization Ellipse

In this Appendix the mathematical steps necessary to find the polarization ellipse will be described [5].

The two components of the electrical field can be described as:

$$\begin{aligned} E_x(z,t) &= E_{0x}\cos(kz-\omega t+\delta_x) \\ E_y(z,t) &= E_{0y}\cos(kz-\omega t+\delta_y) \end{aligned} \tag{8.1}$$

which can also be written as

$$\frac{E_x}{E_{0x}} = \cos(kz-\omega t)\cos\delta_x - \sin(kz-\omega t)\sin\delta_x \tag{8.2}$$

$$\frac{E_y}{E_{0y}} = \cos(kz-\omega t)\cos\delta_y - \sin(kz-\omega t)\sin\delta_y \tag{8.3}$$

By multiplying 8.2 to $\sin\delta_y$ and 8.3 to $\sin\delta_x$ it is obtained:

$$\frac{E_x}{E_{0x}}\sin\delta_y = \cos(kz-\omega t)\cos\delta_x\sin\delta_y - \sin(kz-\omega t)\sin\delta_x\sin\delta_y \tag{8.4}$$

$$\frac{E_y}{E_{0y}}\sin\delta_x = \cos(kz-\omega t)\cos\delta_y\sin\delta_x - \sin(kz-\omega t)\sin\delta_y\sin\delta_x \tag{8.5}$$

And by subtracting 8.5 from 8.4 it can be found:

$$\frac{E_x}{E_{0x}}\sin\delta_y - \frac{E_y}{E_{0y}}\sin\delta_x = \cos(kz-\omega t)\sin(\delta_y-\delta_x) \tag{8.6}$$

The same procedure can be done by multiplying 8.2 to $\cos\delta_y$ and 8.3 to $\cos\delta_x$, then by subtracting the two. The achieved result is

$$\frac{E_x}{E_{0x}}\cos\delta_y - \frac{E_y}{E_{0y}}\cos\delta_x = \sin(kz-\omega t)\sin(\delta_y-\delta_x) \tag{8.7}$$

By squaring Equations 8.6 and 8.7, and then adding the two, the polarization ellipse is finally found:

$$\frac{E_x^2}{E_{0x}^2} + \frac{E_y^2}{E_{0y}^2} - 2\,\frac{E_xE_y}{E_{0x}E_{0y}}\cos(\delta_y-\delta_x) = \sin^2(\delta_y-\delta_x) \tag{8.8}$$

The polarization ellipse is valid only for any given instant of time and its equation with its parameters expressed as a funtion of time is the following [5].

$$\frac{E_x^2(t)}{E_{0x}^2(t)} + \frac{E_y^2(t)}{E_{0y}^2(t)} - 2\,\frac{E_x(t)\,E_y(t)}{E_{0x}(t)\,E_{0y}(t)}\cos\delta(t) = \sin^2\delta(t) \tag{8.9}$$

where $\delta(t) = \delta_y(t) - \delta_x(t)$.

Considering E_{0x}, E_{0y} and δ constant over time, and E_x and E_y implicitly dependent on it, the previous equation reduces to:

$$\frac{E_x^2(t)}{E_{0x}^2} + \frac{E_y^2(t)}{E_{0y}^2} - 2\,\frac{E_x(t)\,E_y(t)}{E_{0x}\,E_{0y}}\cos\delta = \sin^2\delta \tag{8.10}$$

To represent 8.10 in terms of the observable of the optical field, an average over the observation time is needed. Since $E_x(t)$ and $E_y(t)$ are periodic, the average can be done over a single period of oscillation, hence

$$\frac{\langle E_x^2(t)\rangle}{E_{0x}^2} + \frac{\langle E_y^2(t)\rangle}{E_{0y}^2} - \frac{2\,\langle E_x(t)\,E_y(t)\rangle}{E_{0x}\,E_{0y}}\cos\delta = \sin^2\delta \tag{8.11}$$

where

$$\langle E_i(t)\,E_j(t)\rangle = \lim_{T\to+\infty}\frac{1}{T}\int_0^T E_i(t)\,E_j(t)\,dt \qquad i,j = x,y \tag{8.12}$$

Multiplying 8.11 by $4\,E_{0x}^2\,E_{0y}^2$ it can be observed that

$$4\,E_{0y}^2\langle E_x^2(t)\rangle + 4\,E_{0x}^2\langle E_y^2(t)\rangle - 8\,E_{0x}\,E_{0y}\,\langle E_x(t)\,E_x(t)\rangle\cos\delta = (2\,E_{0x}\,E_{0y}\sin\delta)^2 \tag{8.13}$$

From the definition of electrical field, for which

$$\begin{aligned} E_x(t) &= E_{0x}(t)\cos(\omega t + \delta_x(t)) \\ E_y(t) &= E_{0y}(t)\cos(\omega t + \delta_y(t)) \end{aligned} \tag{8.14}$$

where it has been considered $z = 0$, it can be found that

$$\begin{aligned} \langle E_x^2(t) \rangle &= \frac{1}{2} E_{0x}^2 \\ \langle E_y^2(t) \rangle &= \frac{1}{2} E_{0y}^2 \\ \langle E_x(t)\, E_y(t) \rangle &= \frac{1}{2} E_{0x}\, E_{0y} \cos\delta \end{aligned} \tag{8.15}$$

By substituting 8.15 into 8.13 it is obtained:

$$2\, E_{0x}^2\, E_{0y}^2 + 2\, E_{0x}^2\, E_{0y}^2 - (2\, E_{0x}\, E_{0y} \cos\delta)^2 = (2\, E_{0x}\, E_{0y} \sin\delta)^2 \tag{8.16}$$

Then by adding and subtracting $E_{0x}^4\, E_{0y}^4$ to the left side of the previous equation, it is finally found

$$(E_{0x}^2 + E_{0y}^2)^2 - (E_{0x}^2 - E_{0y}^2)^2 - (2\, E_{0x}\, E_{0y} \cos\delta)^2 = (2\, E_{0x}\, E_{0y} \sin\delta)^2 \tag{8.17}$$

From which the Stokes parameters are:

$$\begin{cases} S_0 = E_{0x}^2 + E_{0y}^2 & = I \\ S_1 = E_{0x}^2 - E_{0y}^2 & = Q \\ S_2 = 2\, E_{0x}\, E_{0y} \cos\delta & = U \\ S_3 = 2\, E_{0x}\, E_{0y} \sin\delta & = V \end{cases} \tag{8.18}$$

The polarization state of light can be identified by the four parameter Stokes vector $S = (S_0\, S_1\, S_2\, S_3)^T$:

- **Linear vertically polarized light:**

$$E_{0x} = 0 \quad \Longrightarrow \quad I_0 \begin{pmatrix} 1 \\ -1 \\ 0 \\ 0 \end{pmatrix} \quad \text{with} \quad I_0 = E_{0y}^2 \tag{8.19}$$

- **Linear horizontally polarized light:**

$$E_{0y} = 0 \quad \Longrightarrow \quad I_0 \begin{pmatrix} 1 \\ 1 \\ 0 \\ 0 \end{pmatrix} \quad \text{with} \quad I_0 = E_{0x}^2 \tag{8.20}$$

- **Linear $\pm 45^\circ$ polarized light:**

$$E_{0x} = E_{0y} = E_0;\ \ \delta = 0, \pi \quad \Longrightarrow \quad I_0 \begin{pmatrix} 1 \\ 0 \\ \pm 1 \\ 0 \end{pmatrix} \quad \text{with} \quad I_0 = 2\, E_0^2 \tag{8.21}$$

- **Right and Left circularly polarized light:**

$$E_{0x} = E_{0y} = E_0;\ \ \delta = \pm \pi/2 \quad \Longrightarrow \quad I_0 \begin{pmatrix} 1 \\ 0 \\ 0 \\ \pm 1 \end{pmatrix} \quad \text{with} \quad I_0 = 2\, E_0^2 \tag{8.22}$$

8.4 Finite Element Method

The finite element method (FEM) is a numerical technique used to solve general problems involving partial differential equations [19]. In this section an overview of the main steps of this technique are described.

The basic concept behind the FEM is to divide a complex system into smaller and simpler components called finite elements. The beaviour of every discretized element is described by a set of equations with unknown coefficients derived from the partial differential equation governing the system. Thus, the solution of the whole system is approximated by a finite number of unknown coefficients.

The first step is the discretization of the entire model into smaller elements with associated nodes. These components can have different shape and dimension, depending on the complexity of the problem. Moreover, the way in which the system is divided affects the accuracy of the results. The nodes of each element have a certain number of degrees of freedom, depending on whether they are subjected to constraints or not.

Each finite element is then associated to interpolation functions, usually polynomials, to provide an approximation of the unknown quantity within the element (for example, in a structural analysis one of the most common unknown is the displacement at the nodes). Once the elements and their shape functions have been defined, the properties of the individual elements can be determined.

These properties are then assembled in matrix equations expressing the behaviour of the elements, which are then combined to form the matrix equations expressing the behaviour of the entire system. This assembly process involves combining the element equations based on shared nodal points or degrees of freedom.

Then, the boundary conditions of the problems must be imposed, thus modifying the system equations, which now describe the relationship between the unknown quantities, their derivatives, and the applied loads and boundary conditions.

Finally, the global system of equations is solved numerically using various techniques, such as direct solvers or iterative methods, to obtain the unknown nodal values of the problem.

8.5 Additional Results

In this appendix, additional results of the optical properties and the finite element analysis have been reported.

8.5.1 Optical properties

In the following figures, the transmissivity and reflectivity as a function of the polarization angle is shown for Moxtek RCV8N2EC and UBB01A. Moreover, the reflectivities at 15° and 20° AOI are reported.

Moxtek RCV8N2EC

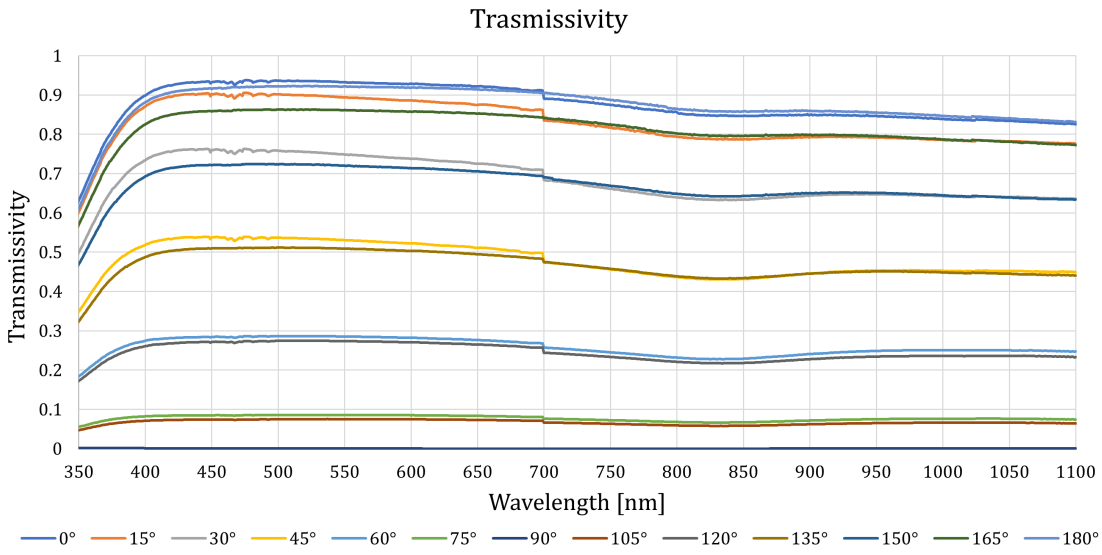


Figure 8.2: Transmissivity of Moxtek RCV8N2EC polarizer in the wavelength range 350-1100 nm, as a function of the polarization angle.

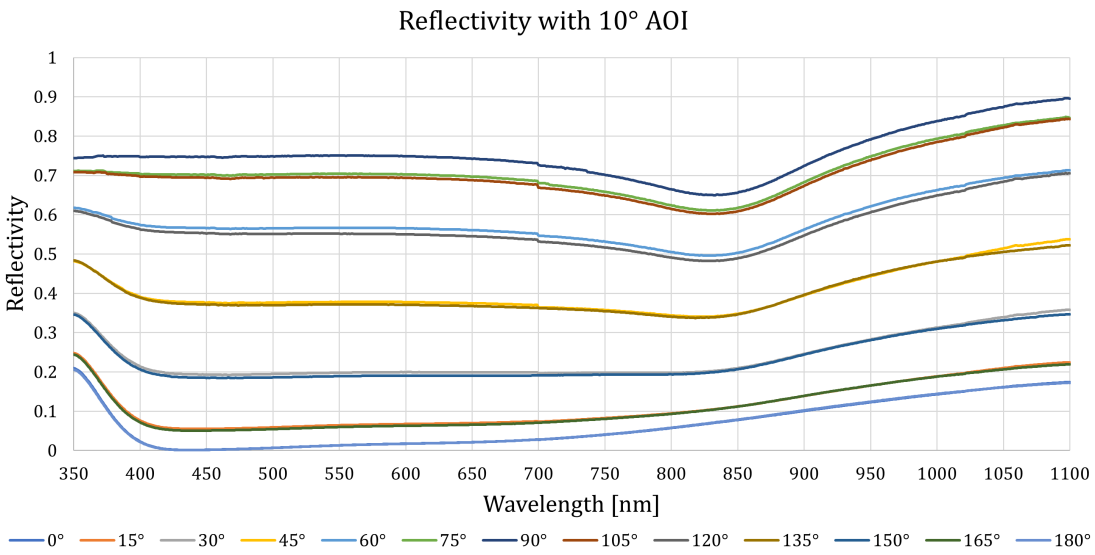


Figure 8.3: Reflectivity of Moxtek RCV8N2EC polarizer in the wavelength range 350-1100 nm, as a function of the polarization angle.

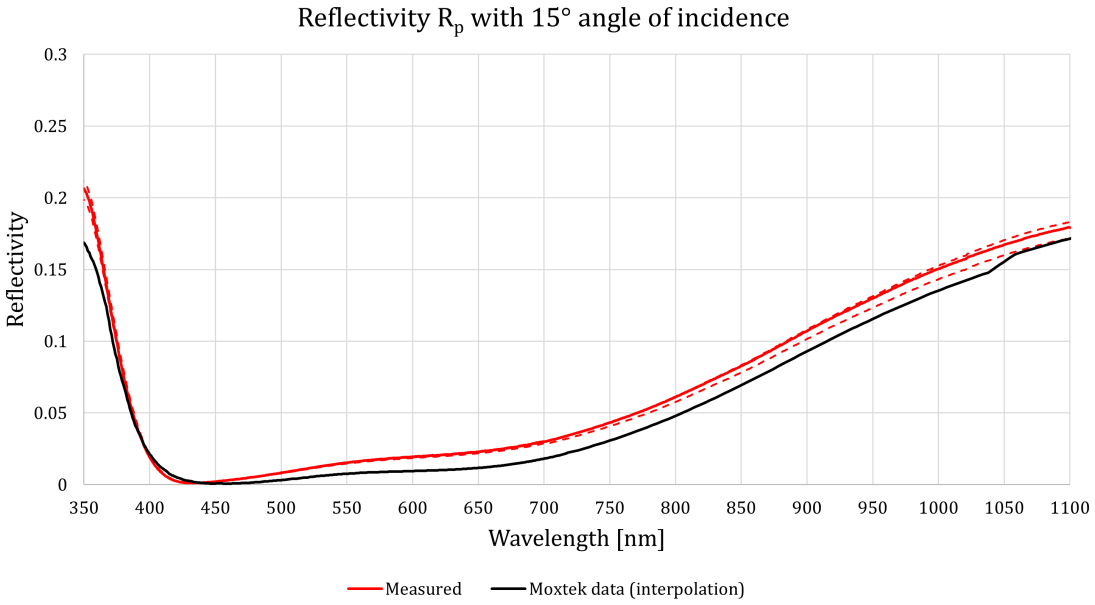


Figure 8.4: Reflectivity R_p of Moxtek RCV8N2EC polarizer with a 15° AOI, in the wavelength range 350-1100 nm. Dashed lines give the confidence range of the measurements.

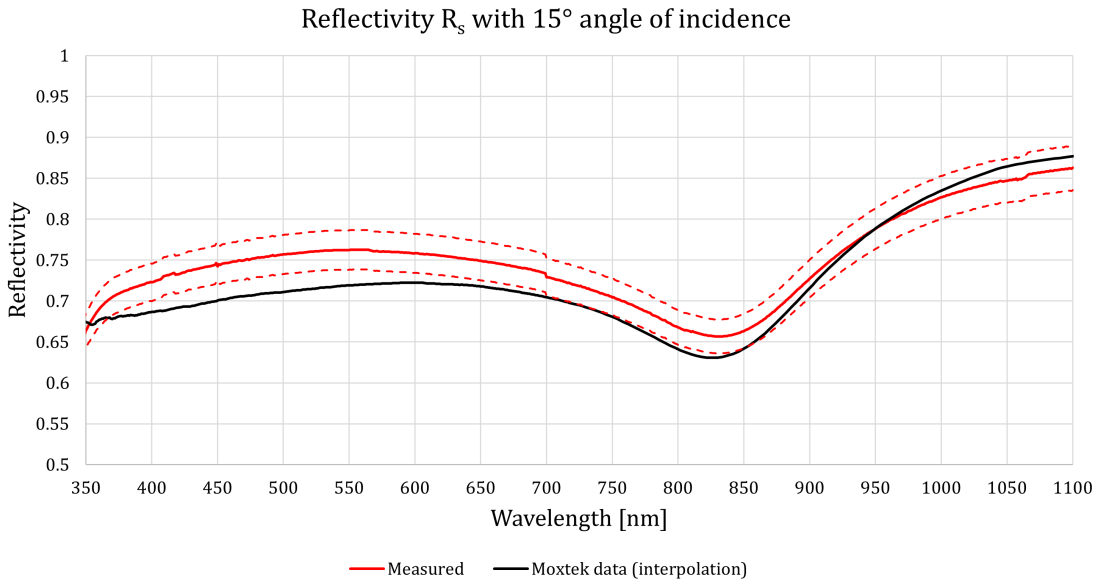


Figure 8.5: Reflectivity R_s of Moxtek RCV8N2EC polarizer with a 15° AOI, in the wavelength range 350-1100 nm. Dashed lines give the confidence range of the measurements.

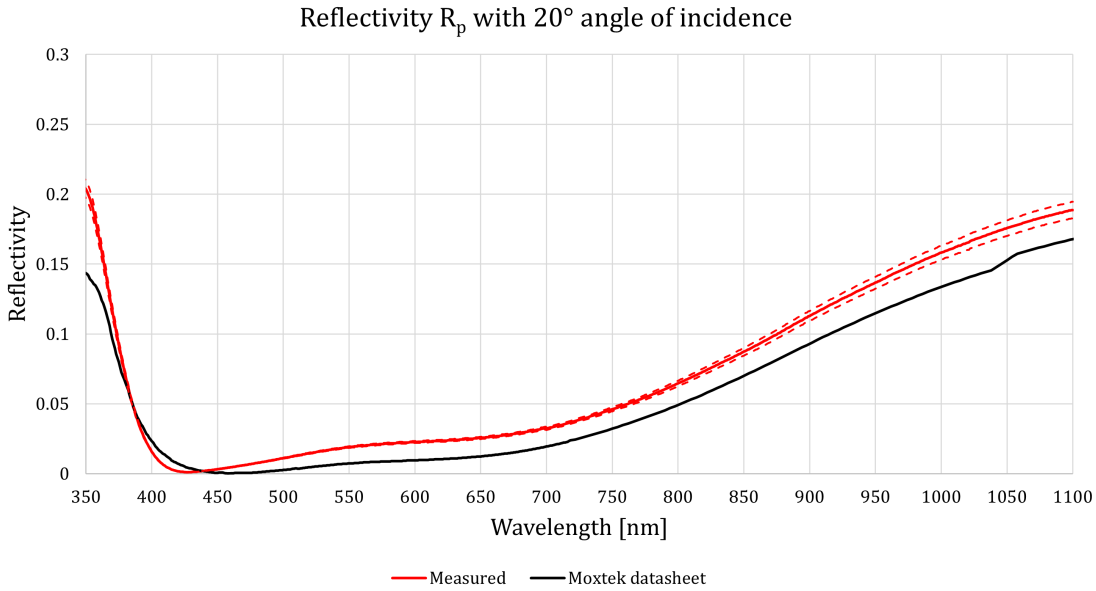


Figure 8.6: Reflectivity R_p of Moxtek RCV8N2EC polarizer with a 20° AOI, in the wavelength range 350-1100 nm. Dashed lines give the confidence range of the measurements.

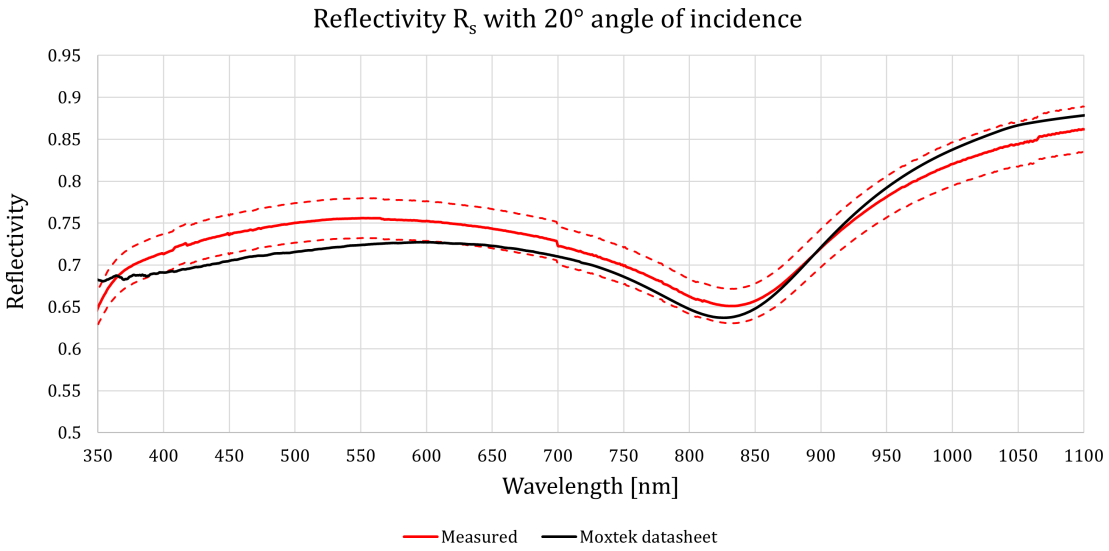


Figure 8.7: Reflectivity R_s of Moxtek RCV8N2EC polarizer with a 20° AOI, in the wavelength range 350-1100 nm. Dashed lines give the confidence range of the measurements.

Moxtek UBB01A

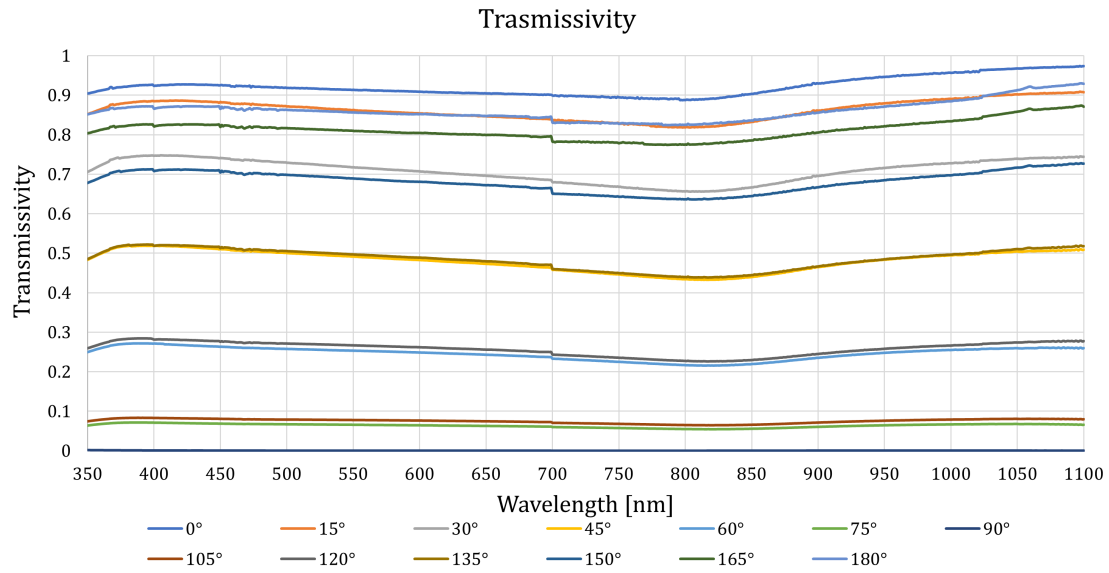


Figure 8.8: Transmissivity of Moxtek UBB01A polarizer in the wavelength range 350-1100 nm, as a function of the polarization angle.

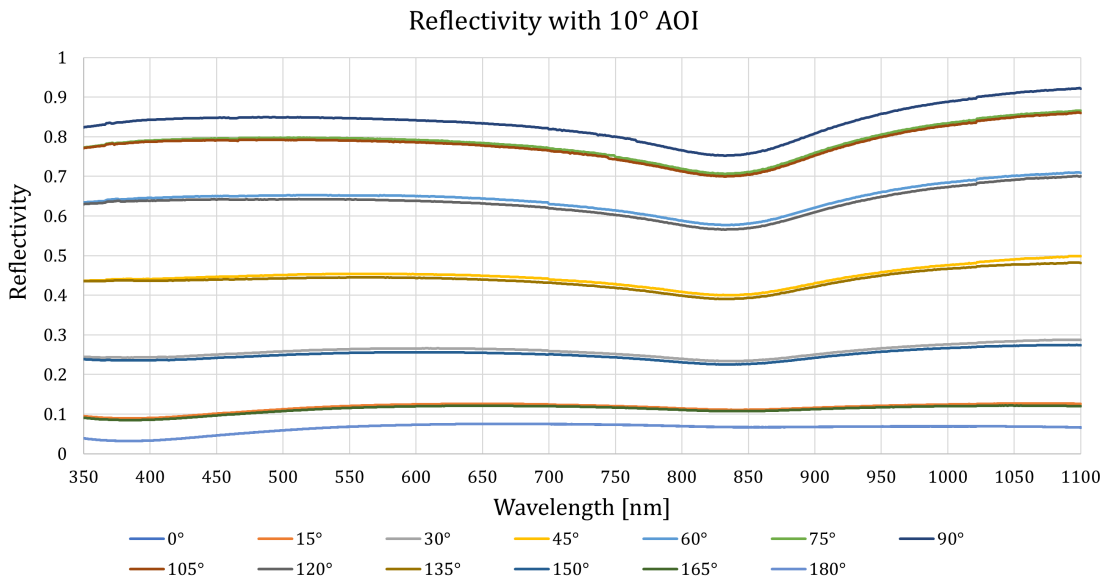


Figure 8.9: Reflectivity of Moxtek UBB01A polarizer in the wavelength range 350-1100 nm, as a function of the polarization angle.

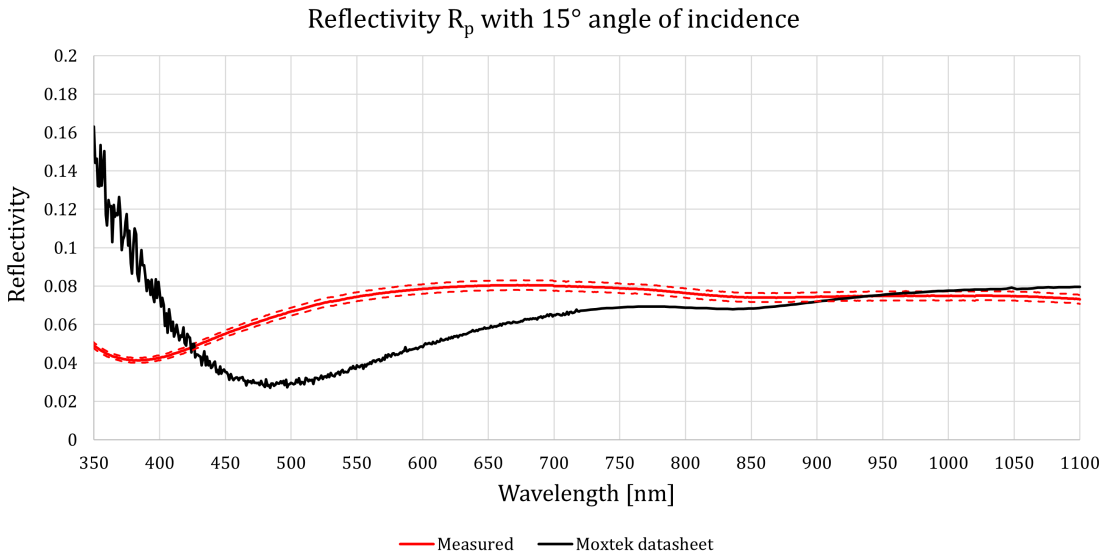


Figure 8.10: Reflectivity R_p of Moxtek UBB01A polarizer with a 15° AOI, in the wavelength range 350-1100 nm. Dashed lines give the confidence range of the measurements.

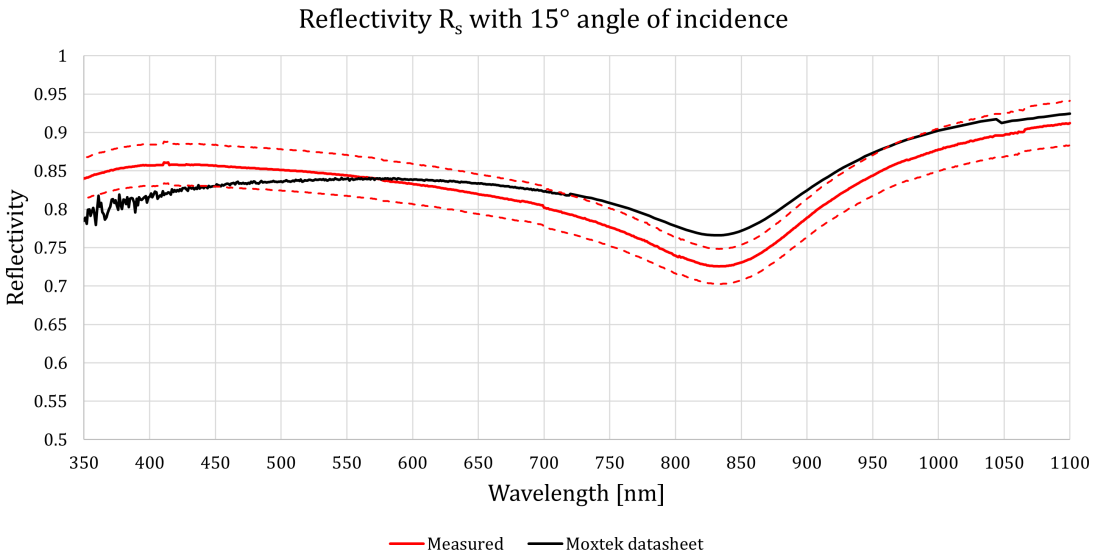


Figure 8.11: Reflectivity R_s of Moxtek UBB01A polarizer with a 15° AOI, in the wavelength range 350-1100 nm. Dashed lines give the confidence range of the measurements.

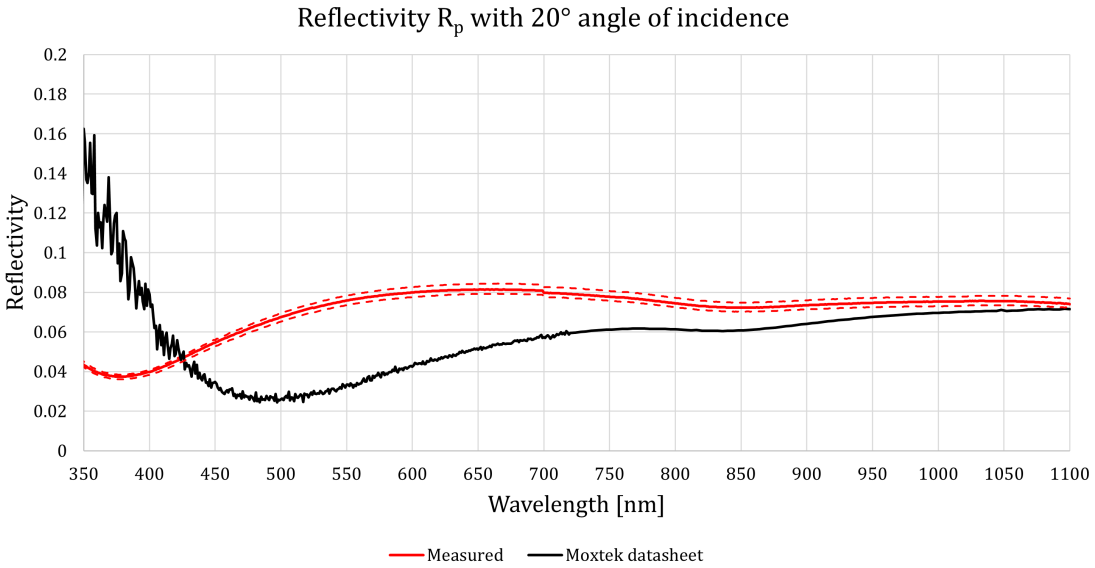


Figure 8.12: Reflectivity R_p of Moxtek UBB01A polarizer with a 20° AOI, in the wavelength range 350-1100 nm. Dashed lines give the confidence range of the measurements.

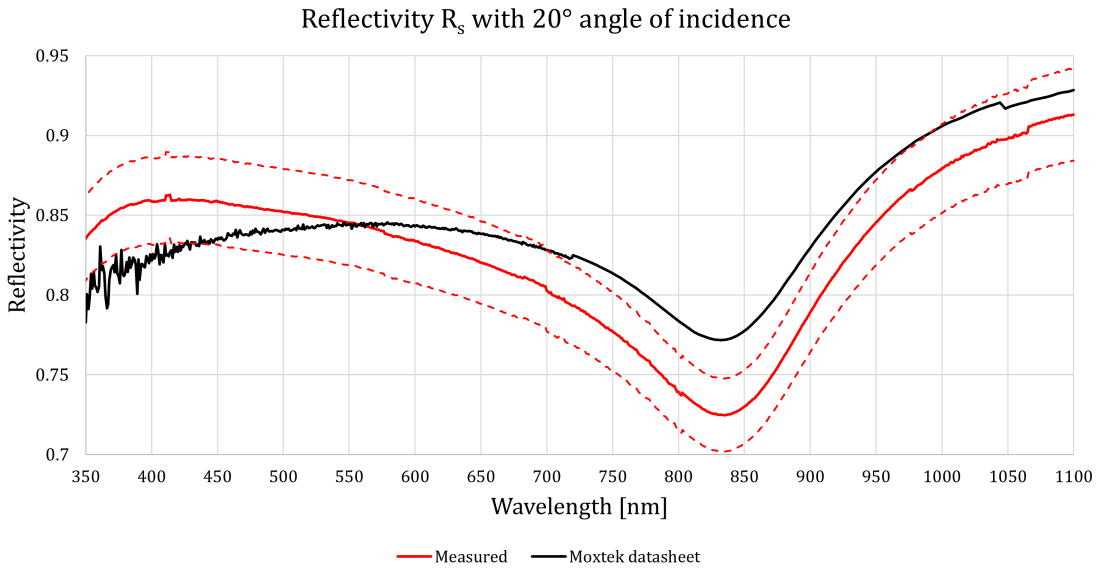


Figure 8.13: Reflectivity R_s of Moxtek UBB01A polarizer with a 20° AOI, in the wavelength range 350-1100 nm. Dashed lines give the confidence range of the measurements.

8.5.2 Finite Element Analysis

In this paragraph additional results regarding the quasi-static acceleration analysis and the effect og the non-planarity of the mechanical interface are shown.

Quasi-static inertial load effect

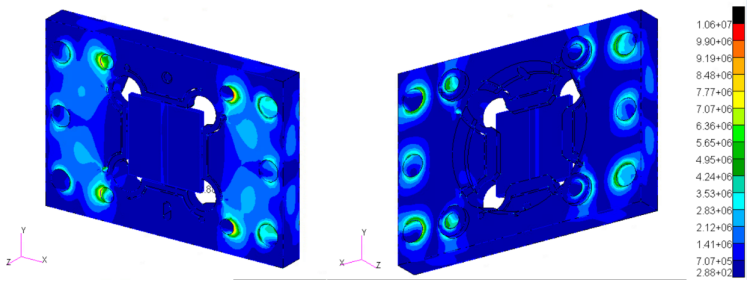


Figure 8.14: Von Mises stress distribution on the analyzed system when subjected to 56g inertial load along the positive y-axis.

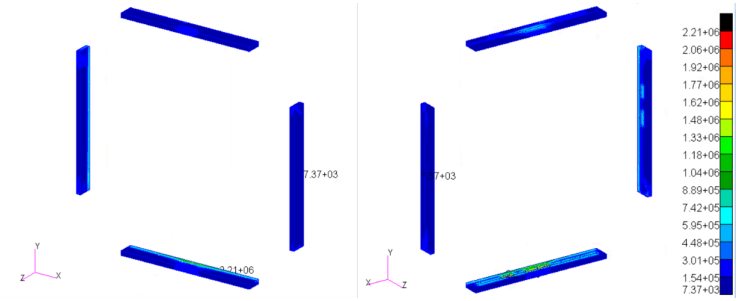


Figure 8.15: Von Mises stress distribution on the glue layers when subjected to 56g inertial load along the positive y-axis.

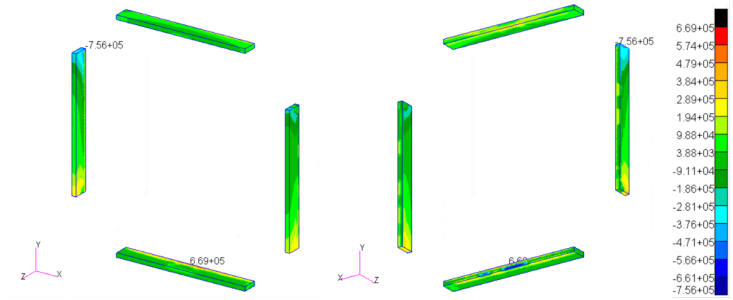


Figure 8.16: X-component of the stress tensor acting on the glue layers when subjected to 56g inertial load along the positive y-axis.

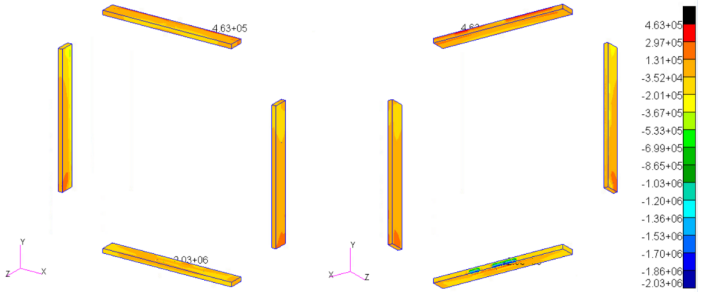


Figure 8.17: Y-component of the stress tensor acting on the glue layers when subjected to 56g inertial load along the positive y-axis.

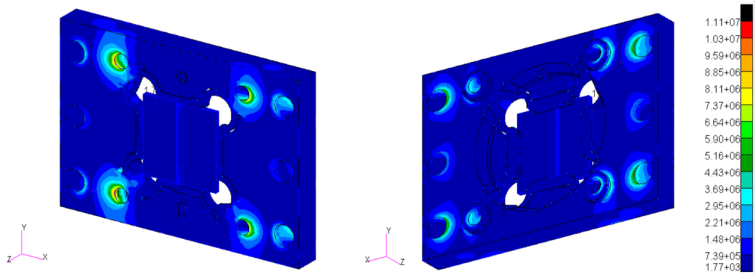


Figure 8.18: Von Mises stress distribution on the analyzed system when subjected to 56g inertial load along the positive z-axis.

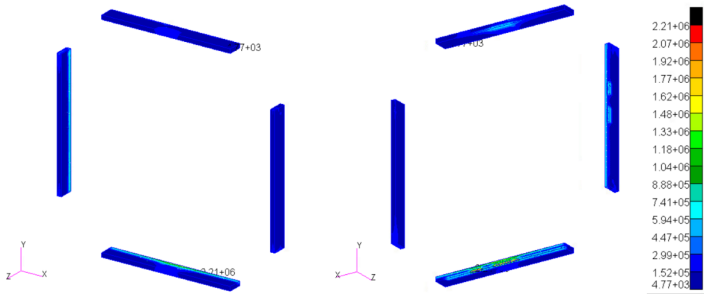


Figure 8.19: Von Mises stress distribution on the glue layers when subjected to 56g inertial load along the positive z-axis.

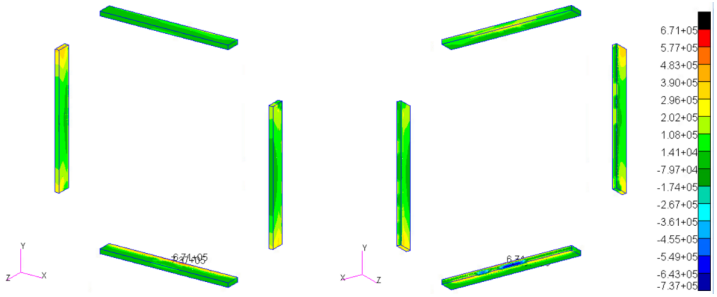


Figure 8.20: X-component of the stress tensor acting on the glue layers when subjected to 56g inertial load along the positive z-axis.

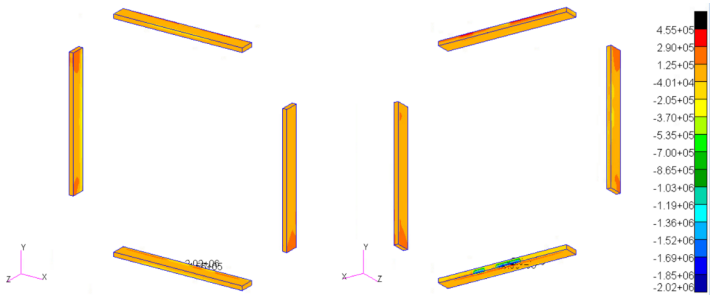


Figure 8.21: X-component of the stress tensor acting on the glue layers when subjected to 56g inertial load along the positive z-axis.

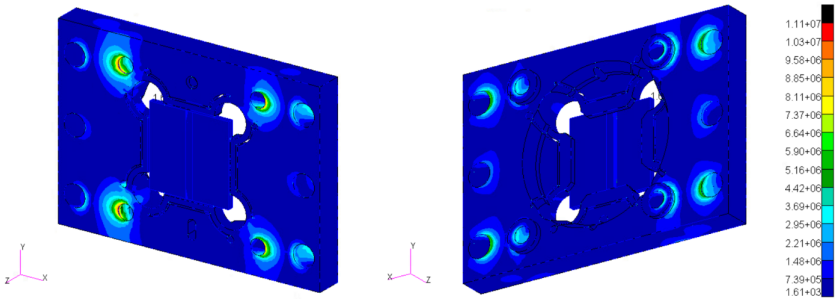


Figure 8.22: Von Mises stress distribution on the analyzed system when subjected to 56g inertial load along the negative z-axis.

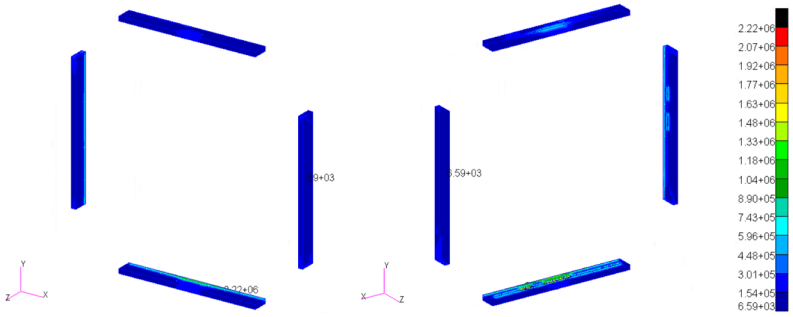


Figure 8.23: Von Mises stress distribution on the glue layers when subjected to 56g inertial load along the negative z-axis.

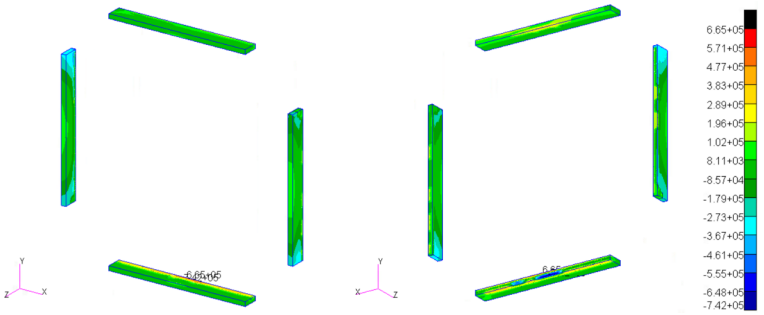


Figure 8.24: X-component of the stress tensor acting on the glue layers when subjected to 56g inertial load along the negative z-axis.

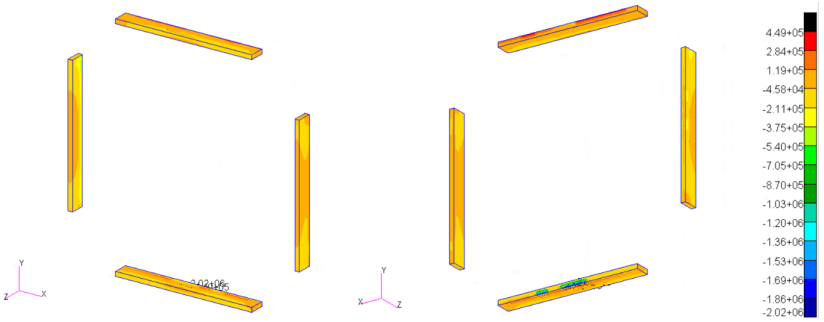


Figure 8.25: Y-component of the stress tensor acting on the glue layers when subjected to 56g inertial load along the negative z-axis.

Non-planarity of the mechanical interface effect

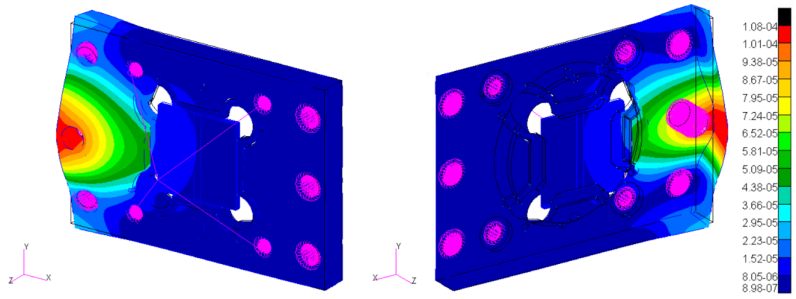


Figure 8.26: Deformation of the analyzed system when subjected to a 100 µm displacement of one of the pinned nodes.

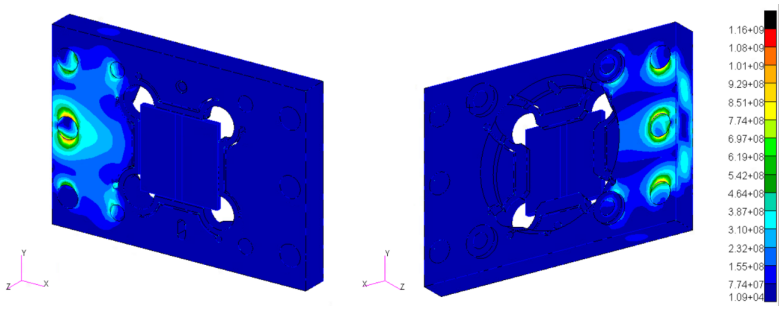


Figure 8.27: Von Mises stress distribution on the analyzed system when subjected to a 100 μm displacement of one of the pinned nodes.

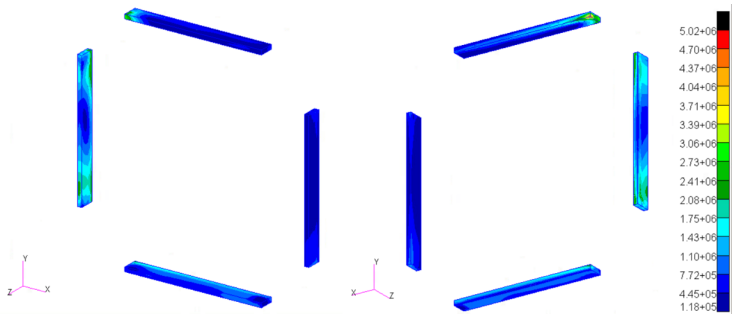


Figure 8.28: Von Mises stress distribution on the glue layers when subjected to a 50 μm displacement of one of the pinned nodes.

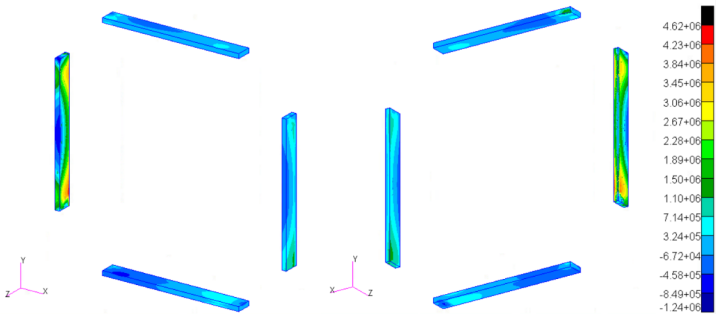


Figure 8.29: X-component of the stress tensor acting on the glue layers when subjected to a 50 μm displacement of one of the pinned nodes.

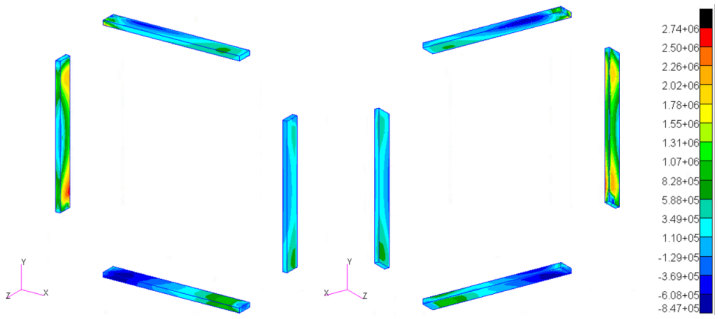


Figure 8.30: Y-component of the stress tensor acting on the glue layers when subjected to a 50 µm displacement of one of the pinned nodes.

8.6 Roughness parameters

In this Appendix the roughness parameters resulting from the topography analysis will be explained ([24], [25]). Note that the used nomenclature corresponds to that of the tables in Figures 5.33b, 5.35b and 5.37b.

- **Rpv:** distance between the maximum peak height and maximum valley depth.

$$\mathrm{Rpv} = |\mathrm{Max}| + |\mathrm{Min}|$$

- **Rq:** root mean square roughness.

$$\mathrm{Rq} = \sqrt{\frac{1}{\mathrm{L}} \int_0^{\mathrm{L}} \mathrm{Z}^2(\mathrm{x})\, \mathrm{dx}}$$

  where L is the sampling length and Z(x) is the function of the sample's height.

- **Ra:** arithmetic mean deviation.

$$\mathrm{Ra} = \frac{1}{\mathrm{L}} \int_0^{\mathrm{L}} |\mathrm{Z}(\mathrm{x})|\, \mathrm{dx}$$

  where L is the sampling length and Z(x) is the function of the sample's height.

- **Rz:** Ten-point mean roughness, it represents the sum of the mean value for the height of the five highest peaks and the mean of the depth of the five deepest valleys of a profile within the sampling length.

$$\mathrm{Rz} = \frac{1}{5} \sum_{\mathrm{i}=1}^{5} (\mathrm{Z}_{\mathrm{max_i}} + \mathrm{Z}_{\mathrm{min_i}})$$

- **Rsk:** skewness, it represents the quotient of the mean cube value of Z(x) and the cube of Rq within a sampling length.

$$\mathrm{Rz} = \frac{1}{\mathrm{Rq}^3} \frac{1}{\mathrm{L}} \int_0^{\mathrm{L}} \mathrm{Z}^3(x)\, \mathrm{dx}$$

if Rsk=0 then the surface height is symmetric against the mean line (normal distribution), if Rsk>0 there will be a deviation beneath the mean line, and if Rsk<0 the deviation will be above the mean line.

- **Rku:** kurtosis, it represents the quotient of the mean quadratic value of Z(x) and the fourth power of Rq within a sampling length.

$$\mathrm{Rz} = \frac{1}{\mathrm{Rq}^4}\frac{1}{\mathrm{L}}\int_0^{\mathrm{L}} \mathrm{Z}^4(x)\,\mathrm{dx}$$

if Rku=3, then there will be a normal distribution, if Rku>3 the height distribution will be sharp, and if Rku<3 the height distribution is even.

References

[1] "Comets," https://solarsystem.nasa.gov/asteroids-comets-and-meteors/comets/overview/?page=0&per_page=40&order=name+asc&search=&condition_1=102%3Aparent_id&condition_2=comet%3Abody_type%3Ailike.

[2] "Comet interceptor, visiting a pristine comet - definition study report," https://www.cosmos.esa.int/documents/3760686/3760706/Comet+Interceptor+Red+Book.pdf/dfa9634f-b15b-e918-17b5-5a8523149ea7?t=1664524062069, published on 26th April, 2022.

[3] S. Nordera, V. D. Deppo, P. Zuppella, P. Chioetto, V. D. Corte, C. Pernechele, U. Barozzi, R. Gabrieli, G. Impicciché, D. Labate, B. Tofani, and L. Tommasi, "Ghost analysis of the EnVisS camera for the Comet Interceptor ESA mission," in *Space Telescopes and Instrumentation 2022: Optical, Infrared, and Millimeter Wave*, S. M. Laura E. Coyle and M. D. Perrin, Eds., vol. 12180, International Society for Optics and Photonics. SPIE, 2022, p. 1218036. [Online]. Available: https://doi.org/10.1117/12.2629473

[4] S. Nordera, V. D. Deppo, P. Zuppella, and P. Chioetto, "Characterization of polarizing filters for the enviss camera: procedure and results," 2022.

[5] D. Goldstein and D. Goldstein, *Polarized Light, Revised and Expanded*, ser. Optical engineering. CRC Press, 2003. [Online]. Available: https://books.google.it/books?id=aWX5jj603PoC

[6] E. Hecht, *Optics*. Pearson Education, Incorporated, 2017. [Online]. Available: https://books.google.it/books?id=ZarLoQEACAAJ

[7] D. Hansen, E. Gardner, R. Perkins, M. Lines, and A. Robbins, "18.3: Invited paper: The display applications and physics of the proflux™ wire grid polarizer," *Sid Symposium Digest of Technical Papers*, vol. 33, 05 2002.

[8] "Visible light polarizers, ppl, pfu & rcv series datasheet," https://moxtek.com/wp-content/uploads/OPT-DATA-1004-PPL-PFU-and-RCV-Series.pdf.

[9] "Ultra broadband polarizers, ubb series datasheet," https://moxtek.com/wp-content/uploads/OPT-DATA-1007-Ultra-Broadband-Polarizers-UBB-Series.pdf.

[10] M. Xu, H. Urbach, D. de Boer, and H. Cornelissen, "Wire-grid diffraction gratings used as polarizing beam splitter for visible light and applied in liquid crystal on silicon," *Opt. Express*, vol. 13, no. 7, pp. 2303–2320, Apr 2005. [Online]. Available: https://opg.optica.org/oe/abstract.cfm?URI=oe-13-7-2303

[11] "Polarcor glass polarizer, product information," https://pdf.directindustry.com/pdf/corning/polarcor-glass-polarizers/12631-666657.html.

[12] https://www.edmundoptics.eu/f/corning-polarcor-glass-polarizers/39626/.

[13] G. Zeni, P. Chioetto, L. Cocola, A. J. Corso, P. Zuppella, and L. Poletto, "Bentham reflectometer characterization," 7 Nov. 2022.

[14] http://dipastro.pd.astro.it/studenti/espfis1/esperI_cap9.pdf.

[15] https://snsf.stanford.edu/facilities/xsa/parkxe.

[16] O. Marti, B. Drake, and P. K. Hansma, "Atomic force microscopy of liquid-covered surfaces: Atomic resolution images," *Appl. Phys. Lett. 51, 484-486*, 1987.

[17] J. Kwon, J. Hong, Y.-S. Kim, D.-Y. Lee, K. Lee, S.-M. Lee, and S.-I. Park, "Atomic force microscope with improved scan accuracy, scan speed, and optical vision," *Review of Scientific Instruments - REV SCI INSTR*, vol. 74, 10 2003.

[18] "Park xe-70 afm user manual," pdf.

[19] V. jagota, A. Sethi, and D.-K. Kumar, "Finite element method: An overview," *Walailak Journal of Science & Technology*, vol. 10, pp. 1–8, 01 2013.

[20] "3m™ scotch-weld™ ec-9323-2 b/a, aerospace technical datasheet," https://multimedia.3m.com/mws/media/820936O/3m-scotch-weld-ec-9323-2-b-a.pdf.

[21] K. Anasiewicz and J. Kuczmaszewski, "Adhesive joint stiffness in the aspect of fem modelling," *Materials*, vol. 12, no. 23, 2019. [Online]. Available: https://www.mdpi.com/1996-1944/12/23/3911

[22] J. Goodenough, A. Fitzgerald, K. Bean, J. Hatcliffe, A. Slark, I. Hamerton, and I. Bond, "Reversible adhesives and debondable joints for fibre-reinforced plastics: Characteristics, capabilities, and opportunities," *Materials Chemistry and Physics*, vol. 299, p. 127464, 2023. [Online]. Available: https://www.sciencedirect.com/science/article/pii/S0254058423001724

[23] G. Blugan, G. Mata-Osoro, S. Fecht, J. Janczak-Rusch, and J. Kuebler, "Torsional shear strength of steel joined with high performance aerospace adhesives at cryogenic and elevated temperatures." 2018 Nov 7.

[24] A. Ravindran, S. Karthigeyan, R. Bhat, M. Naidu, N. Senthilnathan, and S. Sinnurkar, "Analysis of surface roughness and 3d scanning topography of zirconia implants before and after photofunctionalisation by 3d optical profilometry- an invitro study," *JOURNAL OF CLINICAL AND DIAGNOSTIC RESEARCH*, vol. 15, 05 2021.

[25] "Surface roughness measurement—parameters," https://www.olympus-ims.com/en/metrology/surface-roughness-measurement-portal/parameters/.

Acknowledgments

To conclude this thesis work, I want to dedicate a paragraph to all the people that made this professional achievement possible.

First and foremost, I want to thank my parents and brother for always supporting me and my decisions, and providing for me without asking anything in return. Thank you for contributing to my personal formation allowing me to get this far. Thank you also to the rest of my family for always believing in me and sharing all my successes and failures together.

A special thanks goes to my supervisor Prof. Mirco Zaccariotto and my co-supervisors Dr. Vania Da Deppo and Dr. Paola Zuppella for all the help and support given me during the past few months in order to develop this project. Thank you for all the precious advices and insights.

A big thanks goes to Simone, my laboratory partner, with whom I performed all the reflectometry measurements and their data elaboration object of this thesis. In addition to Simone, I also want to thank Riccardo, Daniele and all the members of the "Raman gang" for making this internship in the CNR-IFN laboratories a unique and enjoyable experience. Without you these past few months would not have been the same.

Finally, I want to thank Eleonora, Giorgia, Samantha and all my friends, study buddies and companions of advantures for always being there when needed and always supporting me, no matter what.

I really appreciate all of your support, if I am where I am today is also thanks to all of you.